

Growth and Characterization of High Permittivity Thin Film Nanolaminates  
Fabricated by Atomic Layer Epitaxy

Hui Zhang

B.E. of Material Science and Engineering,  
Central South University of Technology, Changsha, Hunan, China, 1994  
M.S. of Material Science and Engineering,  
Oregon Graduate Institute of Science and Technology, 1997  
M.S. of Electrical Engineering,  
Oregon Graduate Institute of Science and Technology, 1998

A dissertation presented to the faculty of the  
Oregon Graduate Institute of Science and Technology  
in partial fulfillment of the  
requirements for the degree  
Doctor of Philosophy  
in  
Electrical and Engineering


May, 2000

The dissertation "Growth and Characterization of High Permittivity Thin Film Nanolaminates Fabricated by Atomic Layer Epitaxy" by Hui Zhang has been examined and approved by the following Examination Committee:

---

Dr. Rajendra Solanki, Thesis Advisor  
Professor, Oregon Graduate Institute

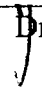
---

 Dr. Jack McCarthy  
Assistant Professor, Oregon Graduate Institute

---

Dr. Anthony Bell  
Associate Professor, Oregon Graduate Institute

---

 Dr. J. Neal Cox, Intel Corporation

*To*  
*my parents*  
*&*  
*my husband*

## **Acknowledgements**

I would like to express my deepest appreciation to my advisor, Dr. Raj Solanki for his guidance, encouragement and financial support during the course of this project.

I am indebted to the thesis committee members: Dr. Jack McCarthy, Dr. Anthony Bell and Dr. J. Neal Cox for reviewing this dissertation and offering helpful suggestions.

Special thanks go to Dr. Indrajit Banerjee, Dr. Christopher Barbero, Dr. Brian Roberds, Dr. Edward Ritz, Justin Shaw, Zeting Pei, Doug Skinner and Lisa Volpol for their constant support and invaluable assistance.

Finally, I would like to thank my husband Michael and our parents for their support and consistent encouragement.

## Table of Contents

ACKNOWLEDGEMENTS.....	iv
TABLE OF CONTENTS.....	v
LISTS OF TABLES.....	vii
LISTS OF FIGURES.....	ix
ABSTRACTS.....	xiv
Chapter 1 Introduction .....	1
Reference .....	5
Chapter 2 MOS System and high permittivity materials.....	8
2.1 MOS System.....	8
2.2 Charges in MOS system.....	20
2.3 Carrier transport in dielectric films.....	23
2.4 MOSFET transistor.....	29
2.5 Scaling issues and limitations .....	34
2.6 High dielectric constant materials.....	37
Reference .....	43
Chapter 3 Atomic layer epitaxy .....	46
3.1 Background of ALE .....	41
3.2 The mechanism of ALE process .....	41
Reference .....	47
Chapter 4 ALE growth of Ta <sub>2</sub> O <sub>5</sub> , HfO <sub>2</sub> , ZrO <sub>2</sub> and their nanolaminates .....	53
4.1 Introduction of the F-120 ALE reactor .....	53

4.2 Growth and initial characterization of Ta <sub>2</sub> O <sub>5</sub> .....	57
4.3 Growth and initial characterization of HfO <sub>2</sub> .....	63
4.4 Growth and initial characterization of ZrO <sub>2</sub> .....	65
4.5 Growth and initial characterization of nanolaminates .....	69
4.5.1 Growth of Ta <sub>2</sub> O <sub>5</sub> -HfO <sub>2</sub> nanolaminates .....	69
4.5.2 Growth of Ta <sub>2</sub> O <sub>5</sub> -ZrO <sub>2</sub> nanolaminates .....	71
4.5.3 Growth of ZrO <sub>2</sub> -HfO <sub>2</sub> nanolaminates.....	71
Reference .....	73
Chapter 5 Characterization of MOS structure with high k insulators .....	75
5.1 Nitrided silicon substrate .....	75
5.2 Material and electrical characterization of binary oxides .....	79
5.2.1 Ta <sub>2</sub> O <sub>5</sub> thin films .....	79
5.2.2 HfO <sub>2</sub> and ZrO <sub>2</sub> thin films .....	93
5.3 Material and electrical characterization of nanolaminates .....	95
5.3.1 Ta <sub>2</sub> O <sub>5</sub> -HfO <sub>2</sub> nanolaminates .....	95
5.3.2 Ta <sub>2</sub> O <sub>5</sub> -ZrO <sub>2</sub> nanolaminates .....	109
5.3.3 ZrO <sub>2</sub> -HfO <sub>2</sub> nanolaminates .....	113
5.4 Electrical properties of SiO <sub>2</sub> and high k films .....	115
Reference .....	120
Chapter 6 Summary and Conclusions .....	122
Vita .....	127

## List of Tables

Table 1-1	The International Technology Roadmap .....	2
Table 2-1	Conduction processes in dielectric films .....	24
Table 2-2	Scaling factors associated with important device parameters for the initial constant-field scaling law, generalized one and the practical constant-voltage scaling law .....	36
Table 2-3	The energy band gap and dielectric constant of various dielectric materials .....	41
Table 5-1	Electrical properties of Ta <sub>2</sub> O <sub>5</sub> thin film grown on p-type Si substrate, where a thin layer of SiO <sub>2</sub> exists at the interface due to the Si oxidation .....	83
Table 5-2	Ta <sub>2</sub> O <sub>5</sub> films grown on Al passivated Si. The thickness of Al layer is 2 nm .....	85
Table 5-3	Electrical properties of Ta <sub>2</sub> O <sub>5</sub> / Si <sub>3</sub> N <sub>4</sub> after RTA in argon and oxygen ambients .....	86
Table 5-4	Electrical properties of HfO <sub>2</sub> / Si <sub>3</sub> N <sub>4</sub> with the thickness of Si <sub>3</sub> N <sub>4</sub> about 2.76nm or 2.12nm .....	93
Table 5-5	Electrical properties of ZrO <sub>2</sub> / Si <sub>3</sub> N <sub>4</sub> with the thickness of Si <sub>3</sub> N <sub>4</sub> about 2.76nm or 2.12nm .....	94
Table 5-6	The Ta <sub>2</sub> O <sub>5</sub> - HfO <sub>2</sub> nanolaminates grown on Al coated Si substrates with and without rapid thermal annealing .....	97
Table 5-7	The Ta <sub>2</sub> O <sub>5</sub> - HfO <sub>2</sub> nanolaminates growth on nitrided Si substrates. The thickness of Si <sub>3</sub> N <sub>4</sub> is 2.76 nm .....	99

Table 5-8	Ta <sub>2</sub> O <sub>5</sub> -ZrO <sub>2</sub> nanolaminates deposited on Si substrates. The thickness ratio of Ta <sub>2</sub> O <sub>5</sub> : ZrO <sub>2</sub> is 12%: 88% .....	109
Table 5-9	Ta <sub>2</sub> O <sub>5</sub> - ZrO <sub>2</sub> nanolaminates grown on nitrided Si substrates. The thickness of Si <sub>3</sub> N <sub>4</sub> is 2.76 nm .....	112
Table 5-10	ZrO <sub>2</sub> -HfO <sub>2</sub> nanolaminates growth on nitrided Si substrates. The thickness of Si <sub>3</sub> N <sub>4</sub> is 2.76 nm .....	114



## List of Figures

Fig. 2.1	MOS Structure .....	9
Fig. 2.2a	Accumulation region of MOS capacitor .....	10
Fig. 2.2b	Depletion region of MOS capacitor .....	10
Fig. 2.2c	Inversion region of MOS capacitor .....	11
Fig. 2.3	Energy band diagram at the surface of a p-type semiconductor. An arrow pointing down (up) denotes positive (negative) potential. Surface potential is measured with respect to the Fermi level $E_F$ at the interface. Surface band bending $\psi_s$ is measured with respect to the intrinsic Fermi level $E_i$ at the interface .....	13
Fig. 2.4	MOS capacitance-voltage characteristics under (a) low frequency (b) high-frequency (c) deep –depletion conditions .....	16
Fig. 2.5	Low frequency equivalent circuit of the MOS capacitor .....	18
Fig. 2.6	High frequency equivalent circuit of the MOS capacitor .....	18
Fig. 2.7	MOS C-V curves measured at room temperature with frequency as a parameter . The substrate is n-type .....	19
Fig. 2.8	MOS C-V characteristics as a function of the oxide thickness. Solid lines correspond to low frequency and dashed lines represent high frequency. The substrate is p-type silicon .....	20
Fig. 2.9	Four categories of oxide charges in the MOS system .....	22
Fig. 2.10	Four basic transport processes in Schottky emission .....	25
Fig. 2.11	Illustration of Frenkel-Poole emission. $\phi_B$ is the barrier height .....	26
Fig. 2.12	Diagram of tunneling processes in insulating films. (a) Direct Tunneling (b) Fowler-Nordheim Tunneling .....	27

Fig. 2.13	Cross section of a MOSFET .....	29
Fig. 2.14	Idealized saturation characteristics ( $I_D$ vs. $V_D$ ) of an n-channel MOSFET .The dashed line indicates the locus of $I_{Dsat}$ vs. $V_{Dsat}$ .....	33
Fig. 2.15	Energy bandgap vs. the dielectric constant of various semiconductor and dielectric materials.....	41
Fig. 3.1	Energy diagram of chemical and physical adsorption .....	48
Fig. 3.2	An ALE processing temperature window .....	49
Fig. 4.1	ALE F-120 reactor system schematic .....	55
Fig. 4.2	Schematic diagram of the F-120 substrate holder (side view) .....	56
Fig. 4.3	The rear view of F-120 substrate holder .....	57
Fig. 4.4	Gas pulse sequence in $Ta_2O_5$ growth by ALE process .....	58
Fig. 4.5	High resolution TEM lattice image of $Ta_2O_5$ film with an ellipsometrically measured thickness of 11.6 nm grown on silicon substrate. A layer of 1.5 nm $SiO_2$ is formed at the interface .....	59
Fig.4.6	Growth rate vs. growth temperature of $Ta_2O_5$ ALE thin films grown on Si substrate using $TaCl_5$ and $H_2O$ .....	61
Fig. 4.7	The effect of RTP on $Ta_2O_5$ film thickness at growth temperatures of 100, 200, 300, 400 and 500°C. The number of water turn is 4 and water is kept at 20°C .....	61
Fig. 4.8	The effect of water on $Ta_2O_5$ film thickness at growth temperature of 300°C .....	61
Fig. 4.9	X-ray diffraction pattern of rapid thermal annealed $Ta_2O_5$ film at 800°C for 30 s in Ar .....	62
Fig. 4.10	X-ray diffraction pattern of $HfO_2$ annealed in RTA chamber at 800°C for 30 s in Ar .....	64
Fig. 4.11	High resolution TEM lattice image of $HfO_2$ film with an ellipsometry thickness of 15 nm grown on Si. $SiO_2$ layer of 2 nm is formed at the interface .....	65
Fig. 4.12	The dependence of film thickness on the $ZrCl_4$ pulse duration	

	for $\text{ZrO}_2$ film deposited at $300^\circ\text{C}$ for 1000 reaction cycles. The $\text{ZrCl}_4$ purge time used was 2.0 s except for 2.0 s pulse time where 4.0 s purge duration was employed .....67
Fig. 4.13	The film thickness as a function of the water purge durations. The data were measured at the center of the film grown by 1000 cycles at $300^\circ\text{C}$ using 2.0 s $\text{ZrCl}_4$ pulses .....68
Fig. 4.14	X-ray diffraction pattern of $\text{ZrO}_2$ annealed at $700^\circ\text{C}$ for 30 s in Ar .....68
Fig. 4.15	Schematic cross-section view of a $\text{Ta}_2\text{O}_5 - \text{HfO}_2$ nanolaminates structure of $2 \times (\text{Ta}_2\text{O}_5 + \text{HfO}_2)$ . The thickness of each constituent layer can be varied by number of reaction cycles. The silicon nitride layer is 2.76 nm thick .....70
Fig. 5.1	FTIR spectrum of the nitrided Si substrate. The thickness of the nitride layer is 2.76nm .....77
Fig. 5.2	AFM image of the silicon nitride layer of 2.76 nm, grown by rapid thermal annealing at $1000^\circ\text{C}$ in ammonium for 30 s .....78
Fig. 5.3a	AFM image of sample #322b1-2 on Si at $300^\circ\text{C}$ for 1000 cycles .....80
Fig. 5.3b	AFM image of sample #351b1-1 on Si at $300^\circ\text{C}$ for 80 cycles .....81
Fig. 5.4	Refractive index of as-deposited $\text{Ta}_2\text{O}_5$ film of 75 nm in the visible region .....81
Fig. 5.5	High frequency C-V curves for 16 nm thick of $\text{Ta}_2\text{O}_5$ annealed at $700^\circ\text{C}$ for 60 s in Ar and $\text{O}_2$ . (a) C-V curve (b) Normalized C-V curve .....87
Fig. 5.6	High frequency C-V curves for 17 nm thick of $\text{Ta}_2\text{O}_5$ annealed at $800^\circ\text{C}$ for 60 s in Ar and $\text{O}_2$ .....88
Fig. 5.7	The leakage current density of MOS capacitors with 16 nm and 17 nm thick $\text{Ta}_2\text{O}_5$ gate dielectric layers and under different annealing conditions .....90
Fig. 5.8	$J/T^2$ plots of gate leakage current under positive gate bias +2.0

	volts for as-deposited and Ar annealed Ta <sub>2</sub> O <sub>5</sub> film of 17 nm .....91
Fig. 5.9	C-V characteristics of the HfO <sub>2</sub> thin films with thicknesses 27.6 nm and 11.6 nm respectively. The thicknesses include 2.76 nm of nitride. The area of the capacitor is 0.0028 cm <sup>2</sup> .....94
Fig. 5.10	An AFM image of the Ta <sub>2</sub> O <sub>5</sub> - HfO <sub>2</sub> nanolaminates. The stack is 5 Ta <sub>2</sub> O <sub>5</sub> + 2 × (10 Ta <sub>2</sub> O <sub>5</sub> + 10 HfO <sub>2</sub> ) .....100
Fig. 5.11	FTIR spectra of Ta <sub>2</sub> O <sub>5</sub> /HfO <sub>2</sub> nanolaminates/Si <sub>3</sub> N <sub>4</sub> /Si and Si <sub>3</sub> N <sub>4</sub> /Si. The top curve is the spectrum of the nanolaminates, the middle one is nitrided silicon substrate, the bottom one is the subtraction of two curves showing that there is no SiO <sub>2</sub> forming at the interface .....101
Fig. 5.11	FTIR spectra of Ta <sub>2</sub> O <sub>5</sub> /HfO <sub>2</sub> nanolaminates/Si <sub>3</sub> N <sub>4</sub> /Si and Si <sub>3</sub> N <sub>4</sub> /Si. The top curve is the spectrum of the nanolaminates, the middle one is nitrided silicon substrate, the bottom one is the subtraction of two curves showing that there is no SiO <sub>2</sub> forming at the interface .....102
Fig. 5.13	Calculation of the flatband voltage from a C-V measurement. The gate voltage corresponds to the peak of $\frac{d^2}{dV_G^2} \left[ \frac{1}{(C_{HF} / C_{ox})^2} \right]$ was the flatband voltage .....103
Fig. 5.14	Hysteresis characteristic of Ta <sub>2</sub> O <sub>5</sub> -HfO <sub>2</sub> /Si <sub>3</sub> N <sub>4</sub> nanolaminates, the Ta <sub>2</sub> O <sub>5</sub> -HfO <sub>2</sub> is 5 Ta <sub>2</sub> O <sub>5</sub> + 10(8×Ta <sub>2</sub> O <sub>5</sub> +8×HfO <sub>2</sub> ) and Si <sub>3</sub> N <sub>4</sub> is 2.12 nm .....104
Fig. 5.15	Frequency dependency of C-V curve of Ta <sub>2</sub> O <sub>5</sub> -HfO <sub>2</sub> /Si <sub>3</sub> N <sub>4</sub> nanolaminates, the Ta <sub>2</sub> O <sub>5</sub> -HfO <sub>2</sub> is 5 Ta <sub>2</sub> O <sub>5</sub> + 10(8×Ta <sub>2</sub> O <sub>5</sub> +8×HfO <sub>2</sub> ) and Si <sub>3</sub> N <sub>4</sub> is 2.12 nm .....105
Fig. 5.16	The leakage current density vs. applied voltage for the Al-Ta <sub>2</sub> O <sub>5</sub> /HfO <sub>2</sub> -Si <sub>3</sub> N <sub>4</sub> -Si capacitor. The thickness of the

	nanolaminates was 7.4 nm. The area of the capacitor is 0.0028 cm <sup>2</sup> .....107
Fig. 5.17	The $\ln(J)$ vs $E^{1/2}$ is plotted for the Al-Ta <sub>2</sub> O <sub>5</sub> /HfO <sub>2</sub> -Si <sub>3</sub> N <sub>4</sub> -Si (MIS) capacitor. The straight line characteristic at low electric field ( $< 0.4$ MV/cm) indicates Schottky emission .....108
Fig. 5.18	The $\ln(J/E)$ vs. $E^{1/2}$ is plotted for the Al-Ta <sub>2</sub> O <sub>5</sub> /HfO <sub>2</sub> -Si <sub>3</sub> N <sub>4</sub> -Si(MIS) capacitor. The straight-line characteristic at relative high electric field ( $> 0.4$ MV/cm) indicates Poole-Frenkel conduction .....108
Fig. 5.19	Gate current density of as-deposited and RTA treated Ta <sub>2</sub> O <sub>5</sub> - ZrO <sub>2</sub> nanolaminates grown on nitrated Si substrates. The thickness of the nanolaminates is about 3.7 nm and the nitride thickness is 2.76 nm .....111
Fig. 5.20	Gate current density of as-deposited and O <sub>2</sub> RTA treated ZrO <sub>2</sub> - HfO <sub>2</sub> nanolaminates grown on nitrated Si substrates. The thickness of the nanolaminates is about 3.4 nm and the nitride thickness is 2.76 nm .....115
Fig. 5.21	Gate leakage current of SiON, Ta <sub>2</sub> O <sub>5</sub> - HfO <sub>2</sub> nanolaminates/Si <sub>3</sub> N <sub>4</sub> , Ta <sub>2</sub> O <sub>5</sub> - ZrO <sub>2</sub> nanolaminates/Si <sub>3</sub> N <sub>4</sub> , and ZrO <sub>2</sub> - HfO <sub>2</sub> nanolaminates/Si <sub>3</sub> N <sub>4</sub> . The thickness of Si <sub>3</sub> N <sub>4</sub> is 2.76 nm for all three nanolaminates .....116
Fig. 5.22	Ramped I-V characteristic of MIS capacitors with binary high k films driven to breakdown in the accumulation mode. All films are of 8 nm thick .....117
Fig. 5.23	I-V characteristics of MIS capacitors of Ta <sub>2</sub> O <sub>5</sub> - HfO <sub>2</sub> , Ta <sub>2</sub> O <sub>5</sub> - ZrO <sub>2</sub> and ZrO <sub>2</sub> - HfO <sub>2</sub> nanolaminates in the accumulation region .....118

## ABSTRACT

### Growth and Characterization of High Permittivity Thin Film Nanolaminates Fabricated by Atomic Layer Epitaxy

Hui Zhang, B. S., M. S.

Ph. D., Oregon Graduate Institute of Science and Technology  
May, 2000

Thesis Professor: Dr. Rajendra Solanki

This thesis considers three issues regarding high permittivity thin films and their nanolaminates. Atomic layer epitaxy, the process technique used to deposit thin films of  $\text{Ta}_2\text{O}_5$ ,  $\text{HfO}_2$ ,  $\text{ZrO}_2$  and their nanolaminates will be discussed first. Material properties of these films are presented next. Finally, the electrical properties and dielectric characteristics are investigated.

Atomic layer epitaxy was used to grow binary oxides ( $\text{Ta}_2\text{O}_5$ ,  $\text{HfO}_2$ , and  $\text{ZrO}_2$ ) and their nanolaminates ( $\text{Ta}_2\text{O}_5$  -  $\text{HfO}_2$ ,  $\text{Ta}_2\text{O}_5$ -  $\text{ZrO}_2$ ,  $\text{HfO}_2$ - $\text{ZrO}_2$ ) on silicon substrates. Metallic chlorides and water vapor were used as source materials. The as-deposited  $\text{Ta}_2\text{O}_5$ ,  $\text{HfO}_2$  and  $\text{ZrO}_2$  thin films grown at  $300^\circ\text{C}$  were amorphous. The crystallization temperatures of these films were  $800^\circ\text{C}$ ,  $800^\circ\text{C}$  and  $700^\circ\text{C}$ , respectively.

Transmission electron microscope (TEM) showed that silicon surface oxidation occurred during the high permittivity film growth due to the use of water vapor. A thin layer of silicon nitride was grown by rapid thermal nitridation as a barrier layer prior to the deposition of high permittivity films.

Capacitors made with these binary oxides and their nanolaminates were characterized by capacitance – voltage (C-V) and current – voltage (I-V) measurements. Dielectric constants, flatband voltage and interface fixed charges were calculated based on C-V data. Leakage current of nanolaminates was dramatically reduced compared to

that of binary oxides. It was found that Schottky emission and Poole-Frenkel conduction were the major leakage mechanisms. Crystallization of amorphous films had two effects on the dielectric properties. First, it increased the dielectric constant, which was desirable. Secondly, it created grain boundaries that facilitate the current leakage in the dielectric films. As the thicknesses of high permittivity films decreased, the dielectric constants dropped. This reduction in dielectric constant has been shown to depend on the number of atomic monolayers and the atomic polarizability of the film. The investigation of these high permittivity nanolaminates suggested that they could be useful for future gate dielectric material.

# **Chapter 1**

## **Introduction**

The metal-oxide-semiconductor or MOS structure is, without a doubt, the core structure in modern-day microelectronics. Although a quasi-MOS device was first proposed in the 1920s, the metal-oxide-semiconductor fields effect transistor (MOSFET) achieved practical status in 1960, mainly attributed to D. Kahng and M. M. Atalla who filed patents on the Si-SiO<sub>2</sub> based FET [1]. Over the last four decades, the integrated circuit (IC) market has increased dramatically. In 1960s the IC market was broadly based on the bipolar transistors. Since 1970s, however, digital MOS ICs has prevailed. MOSFET and related integrated circuits now constitute about 90% of the semiconductor device market.

Throughout the MOS development history, the quality of the gate SiO<sub>2</sub> and its interface to Si has always been playing an essential role, in both MOS and Dynamic Random Access Memory (DRAMs) [2]. There were strong efforts to obtain a dielectric film superior to the thermally grown SiO<sub>2</sub>. They include SiO<sub>2</sub> formed using plasma [3], laser [4], and CVD (Chemical Vapor Deposition) technique [5], Si<sub>3</sub>N<sub>4</sub> [6], and ferroelectrics [7]. Such films having other interfaces than thermal SiO<sub>2</sub> to Si, however, suffered from inferior dielectric quality, especially with respect to the defect charge density, and so have not been implemented as gate dielectrics.

Continued Ultra-Large Scale Integration (ULSI: more than 10<sup>7</sup> transistors on a chip) has been achieved mainly by decreasing the size of an individual transistor as well



as by increasing the chip size and circuit complexity, as typically seen for DRAM whose memory size grows at a rate of approximately four times every three years. The feature size ( $L$ ) of an individual device continues to decrease to two thirds or a little bit less than that of a prior generation. For example,  $L$  was on the order of several micrometers in the 1970s, the decade of Large-Scale Integration (LSI:  $10^3 \sim 10^4$  transistors on a chip), while that for the ULSL is now scaled down to  $0.25\mu\text{m}$  or less. Accordingly, the thickness of the gate oxides has been reduced from  $\sim 100\text{nm}$  in the LSI technology to  $\sim 10\text{nm}$  or less for ULSI. As described in the National Technology Roadmap for Semiconductors (Table 1-1), the device dimension will shrink from  $0.25\mu\text{m}$  in 1997 to  $0.10\mu\text{m}$  in 2005.

**Table 1-1 The International Technology Roadmap [8]**

Year	1999	2000	2001	2002	2003	2004	2005
Technology Node	180nm			130nm			100nm
DRAM $\frac{1}{2}$ Pitch (nm)	180	165	150	130	120	110	100
MPU Gate Length (nm)	140	120	100	85-90	80	70	65
MPU/ASIC $\frac{1}{2}$ Pitch (nm)	230	210	180	160	145	130	115
ASIC Gate Length (nm)	180	165	150	130	120	110	100

The scaling trends discussed above lead to several limitations and issues of the MOS technology, mainly to (a) small-geometry effects, (b) limited performance under high electrical field, (c) hot-carrier-induced device degradation, (d) gate-induced drain leakage, and (e) gate-dielectric reliability [9]. The limitations (b, c, e) are closely related to the quality of the gate dielectric and its interface to silicon, while the limitations (a, b, d) are more dependent on the gate dielectric thickness. In either case, almost all the limitations become more critical as the gate dielectric thickness is scaled down to

nanometer scale. Generally, increasing internal electric fields will enhance the circuit performance while it degrades reliability. Therefore, trade-off between performance and reliability has become one of the most important device design issues in ULSI technology.

With the continuous shrinkage of the silicon dioxide thickness, direct tunneling current through the dielectric will be a very serious concern. A major limiting factor in transistor scaling beyond the current 0.18- $\mu\text{m}$  design rules has been the difficulty to grow high quality, ultra-thin oxides as the tunneling limit of 2.5nm for  $\text{SiO}_2$  is approached and gate currents exceed 1 A/cm<sup>2</sup>. Furthermore,  $\text{SiO}_2$  is not a good diffusion barrier for gate electrode dopants, such as boron. Even with nitrogen incorporation [10, 11], it is difficult to utilize ultra-thin nitrided oxides for sub-0.25 $\mu\text{m}$  technologies due to high tunneling current and rough Si-SiO<sub>2</sub> interface. Therefore, a high dielectric constant (k) material of equivalent electrical dielectric thickness is a possible alternative to thermally grown  $\text{SiO}_2$ . High k materials [12-14] have been studied for storage capacitors but successful demonstrations for MOSFET are rare [15]. The biggest challenge in DRAM technology is to shrink the size of the memory cell, while maintaining enough capacitance to store a bit. With the traditional  $\text{SiO}_2$  as the dielectric, special topologies have to be used to achieve high capacitance and high density. This results in planarization problem and process complexity. Therefore, it is very desirable to replace the current  $\text{SiO}_2$  with high permittivity materials.

As a relatively high permittivity material, silicon nitride film has been studied extensively as a gate or capacitor dielectric. It is not used alone but in combination with  $\text{SiO}_2$  to form silicon oxynitride [16] or nitride/oxide stack [17]. However, the dielectric constant (7.5~7.8) of silicon nitride is not high enough for future 0.10 $\mu\text{m}$  ULSI devices. According to the National Technology Road Map for semiconductors (1997), gate dielectric scaling down to 2nm is desired from 2006 onward. When the  $\text{SiO}_2$  thickness is reduced below 2 nm, alternative high permittivity dielectrics such as  $\text{Ta}_2\text{O}_5$ ,  $\text{TiO}_2$ ,  $\text{HfO}_2$  and  $\text{ZrO}_2$  must be considered.  $\text{Ta}_2\text{O}_5$  has been studied for applications as the capacitor

dielectric in gigabit DRAMs [18-20].  $\text{Ta}_2\text{O}_5$  has also been proposed as MOSFET gate dielectric for high-speed circuit in simulation study [21]. Recently MOSFET devices have also been fabricated using high  $k$  thin films such as  $\text{Ta}_2\text{O}_5$ ,  $\text{HfO}_2$  and  $\text{ZrO}_2$ . Some of these results were reported in references [22-25]. One major obstacle in using high  $k$  materials is that a solid material with higher permittivity tends to have narrower bandgap. This is deduced from a reduced cohesive force according to the quantum-mechanical consideration [26], thereby suffering from a larger leakage current.

The purpose of this research was to study the deposition of  $\text{Ta}_2\text{O}_5$ ,  $\text{HfO}_2$  and  $\text{ZrO}_2$  films and their nanolaminates ( $\text{Ta}_2\text{O}_5$ - $\text{HfO}_2$ ,  $\text{Ta}_2\text{O}_5$ - $\text{ZrO}_2$  and  $\text{HfO}_2$ - $\text{ZrO}_2$ ) using atomic layer epitaxy (ALE) technique and to characterize the material and electrical properties of MOS capacitors made with these films.

This thesis contains 6 chapters including this introduction. In chapter 2, dielectric properties of materials are discussed and the relationship between dielectric constant and bandgap is presented. This chapter also includes basic theory of MOS system and the ULSI device scaling. The ALE technique and its application are described in chapter 3. In chapter 4, the experimental results of the  $\text{Ta}_2\text{O}_5$ ,  $\text{HfO}_2$ ,  $\text{ZrO}_2$  and their nanolaminates by ALE technique are presented. The fabrication sequence and material characteristics are also included in this chapter. Chapter 5 presents material and electrical properties of MOS capacitors built with these high  $k$  thin films. C-V characteristics at high frequency were investigated and dielectric constants were extracted from C-V measurement. I-V characteristics were studied to determine the leakage mechanisms and reliability. Argon and oxygen annealing effects on leakage current are described. Summary and conclusions were presented in chapter 6.

## References

- [1] M. M. Atalla, E. Tannenbaum, and E. J. Scheibner, "Stabilization of silicon surfaces by thermally grown oxides," *Bell Syst. Tech. J.* **38**, 1959, pp. 749-754.
- [2] P. Singer, "Directions in dielectrics in CMOS and DRAMs," *Semiconductor International* **17**, 1994, pp. 56-59.
- [3] V. K. Bhat, K. N. Bhat, and A. Subrahmanyam, "Electrical characterization of Ultrathin oxides of silicon grown by  $N_2O$  plasma assisted oxidation," *J. Electronic Materials* **20**, 2000, pp. 399-404.
- [4] I. W. Boyd, "Incorporation of carbon dioxide laser-grown oxide layers into conventional metal-oxide-silicon devices," *J. Appl. Phys.* **54**, 1983, pp. 3561-3565.
- [5] L. G. Meiners, "Indirect plasma deposition of silicon dioxide," *J. Vac. Sci. Technol.* **21**, 1982, pp. 655-658.
- [6] Y. Kuo, "PECVD silicon nitride as gate dielectric for amorphous silicon thin film transistor," *J. Electrochem. Soc.* **142**, 1995, pp. 186-190.
- [7] J. R. Pfister, *Performance limit of CMOS very large scale integration*, Ph.D. Thesis, Elect. Eng. Dept., Stanford University, Technology Report, No. G541-1 (1984).
- [8] The International Technology Road Map for Semiconductors, Semiconductor Industry Association, San Jose, CA, 1999.
- [9] T. Hori, *Gate Dielectrics and MOS ULSIs*, Springer-Verlag Berlin Heidelberg, 1997, p. 110.
- [10] Y. Yamamoto, T. Ogura, Y. Saito, K. Uwasawa, T. Tatsumi, and T. Mogami, "An advanced 2.5nm oxidized nitride gate dielectric for highly reliable 0.25 $\mu$ m MOSFET," *Symp. on VLSI Technology Digest of Technical Papers*, 1997, pp. 45-46.
- [11] X. Guo and T. P. Ma, "Tunneling Leakage current in oxynitride: dependence on oxygen/nitrogen content," *IEEE Electron Device Letters* **19**, June 1998, pp. 207-209.
- [12] M. Hao, K. Lai, W. M Chen, and J. C. Lee, "Surface cleaning effect on dielectric integrity for Ultrathin oxynitride grown in  $N_2O$ ," *Appl. Phys. Lett.* **65**, 1994, pp. 1133-1135.

- [13] Y. Matsui, K. Torri, M. Hirayama, Y. Fujisaki, S. Iijima, and Y. Ohji, "Reduction of current leakage in chemical vapor deposited Ta<sub>2</sub>O<sub>5</sub> thin films by oxygen radical annealing," IEEE Electron Device Letters **17**, 1996, pp. 431-433.
- [14] S.C. Sun and T. F. Chen, "Leakage current reduction in chemical-vapor deposited Ta<sub>2</sub>O<sub>5</sub> films by rapid thermal annealing in N<sub>2</sub>O," IEEE Electron Device Letters **17**, 1996, pp. 355-357.
- [15] M. Matsui, H. Hagayoshi, G. Muto, S. Tanimoo, K. Kuroiwa, and Y. Tarui, "Amorphous silicon thin film transistors employing photoprocessed tantalum oxide films as gate insulators," Jpn. J. Appl. Phys. **29**, 1990, pp. 62 -66.
- [16] B. Maiti, P. J. Tobin, V. Misra, R. I. Hedge, K. G. Reid, and C. Gelatos, " High performance 20 Å NO oxynitride for gate dielectric in deep sub quarter micron CMOS technology," IEEE IEDM, Washington, DC, Dec. 7-10, 1997, pp. 651-654.
- [17] B. Y. Kim, H. F. Luan, and D. L. Kwong, "Ultra thin (<3nm) high quality nitride /oxide stack gate dielectrics fabricated by in-situ rapid thermal processing," IEEE IEDM, Washington, DC, Dec. 7-10, 1997, pp. 463-466.
- [18] K. A. Mckinley and N. P. Sandler, "Tantalum pentoxide for advanced DRAM applications," Thin Solid Films **290-291**, 1996, pp. 440-446.
- [19] M. B. Lee, H.D. Lee, B.L. Park, U.I.Chung, Y.B. Koh, and M.Y. Lee, "Electrical characterization of CVD TiN upper electrode for Ta<sub>2</sub>O<sub>5</sub> capacitor," IEEE IEDM, San Francisco, CA, Dec. 8-11, 1996, pp. 683-686.
- [20] S. C. Sun and T. F. Chen, "A new post-deposition annealing method using furnace N<sub>2</sub>O for the reduction of leakage current of CVD Ta<sub>2</sub>O<sub>5</sub> storage capacitors," IEEE IEDM, San Francisco, CA, Dec. 8-11, 1996, pp. 687-690.
- [21] H. Shimada and T. Ohmi, "Current drive enhancement by using high-permittivity gate insulator in SOI MOSFET's and its limitation," IEEE Trans. Electron Devices **43**, 1996, pp. 431-435.
- [22] J. L. Autran, R.Devine, C. Chanelieve, and B. Balland, "Fabrication and characterization of Si-MOSFET's with PECVD amorphous Ta<sub>2</sub>O<sub>5</sub> gate insulator," IEEE Electron Device Letters **18**, 1997, pp. 447-449.
- [23] D. Park, Y. King, Q. Lu, T. King, C. Hu, A. Kalnisky, S. Tay, and C. C. Cheng, "Transistor characteristics with Ta<sub>2</sub>O<sub>5</sub> gate dielectric," IEEE Electron Device Letters **19**, Nov. 1998, pp. 441-443.

- [24] B. H. Lee, L. Kang, W-J Qi, R. Nieh, Y. Joen, K. Onishi, and J. C. Lee, "Ultrathin hafnium oxide with low leakage and excellent reliability for alternative gate dielectric application," IEEE IEDM, Washington, DC, Dec.5-8, 1999, pp. 133-136.
- [25] W. J. Qi, R. Nieh, B. H. Lee, L. Kang, Y. Jeon, K. Onishi, T. Ngai, S. Banerjee, and J. C. Lee, "MOSCAP and MOSFET characteristics using  $\text{ZrO}_2$  gate dielectric deposited directly on Si," IEEE IEDM, Washington, DC, Dec.5-8, 1999, pp. 145-148.
- [26] K. W. Boer, Survey of Semiconductor Physics, Van Nostrand Reinhold, 1990, p. 26.

## **Chapter 2**

### **MOS System and High Permittivity Materials**

In this chapter, the history and fundamentals of the metal-oxide-semiconductor structure are reviewed. Basic device physics and device characterization techniques are discussed. Device scaling and demand for high permittivity materials as gate dielectrics are presented as well. This chapter also includes the discussion of dielectric properties of high permittivity materials and their application in ULSI devices.

#### **2.1 MOS system**

An MOS structure shown in Fig. 2.1 consists of a top electrode called a gate generally made by vacuum deposition of a metal or by chemical deposition of polysilicon, an oxide layer usually thermally grown, and an ohmic contact to the silicon substrate. An MOS capacitor has only two terminals, and is the simplest and most useful device in the study of semiconductor surfaces and gate dielectrics [1]. A second metallic layer present on the bottom side of the semiconductor provides an electrical contact to the silicon substrate.

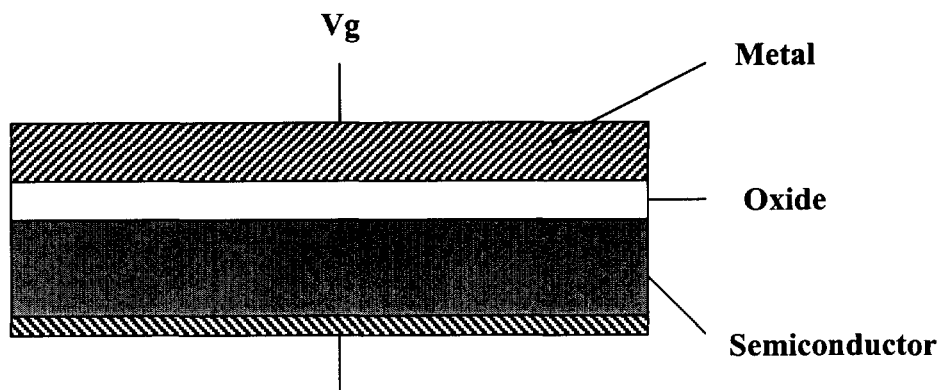


**Fig. 2.1 MOS Structure**

An ideal MOS structure has the following explicit properties: (1) the metallic gate is sufficiently thick so that it can be considered an equipotential region under ac as well as dc biasing conditions; (2) the oxide is a perfect insulator with zero current flowing through the oxide layer under all static biasing conditions; (3) there are no charge centers located in the oxide or at the oxide-semiconductor interface; (4) the semiconductor is uniformly doped; (5) the semiconductor is sufficiently thick so that, regardless of the applied gate potential, a field-free region (so called Si “bulk”) is encountered before reaching the back contact [2]. With the scaling down of device size, the idealization (2) and (3) have been challenged.

The energy band diagram is an indispensable aid in visualizing the internal status of the MOS structure under static biasing conditions. As schematically illustrated in Fig. 2.2, when an ideal MOS capacitor with a p-type substrate is biased with  $V_g$  not equal to zero, basically three situations may arise at the semiconductor surface.



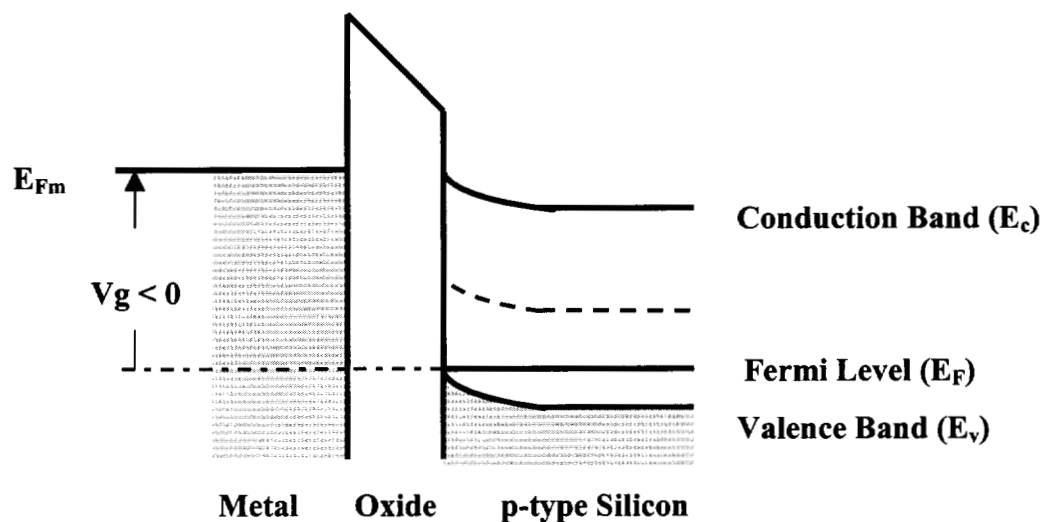


Fig. 2.2a Accumulation region of MOS capacitor

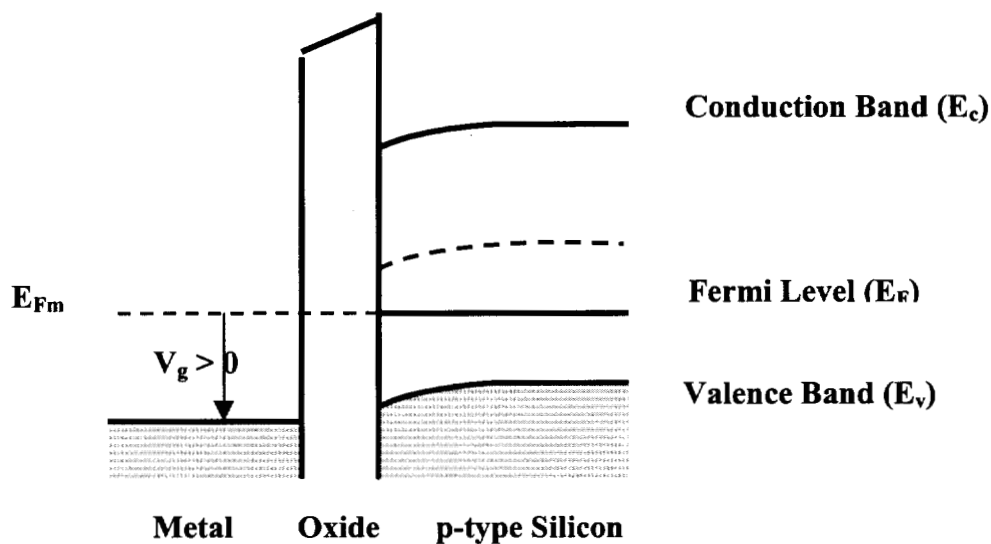
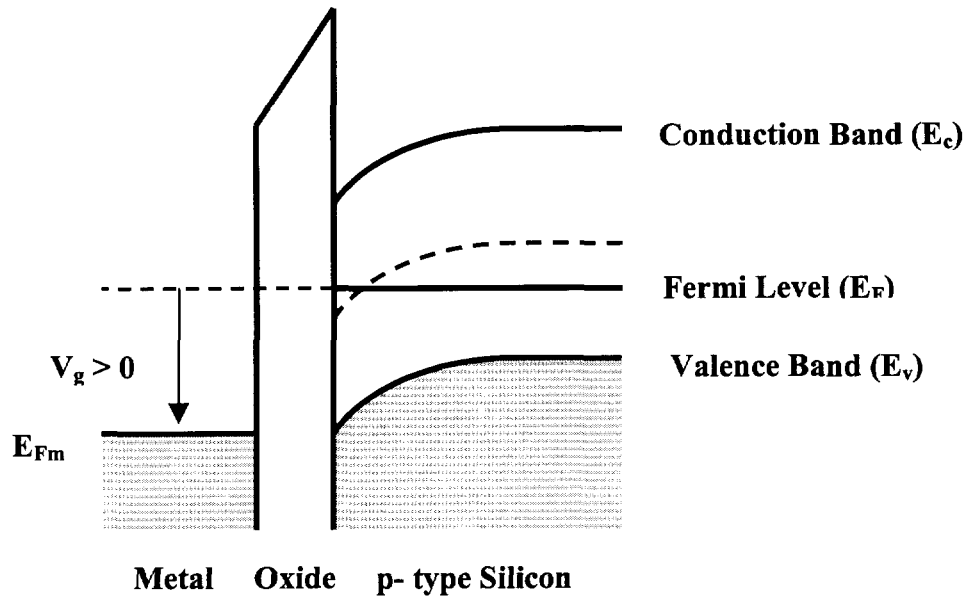


Fig. 2.2b Depletion region of MOS capacitor



**Fig. 2.2c Inversion region of MOS capacitor**

Regardless of the gate potential  $V_g$ , the Fermi level  $E_F$  remains constant throughout the semiconductor since no current flows in the semiconductor. When  $V_g < 0$ , the negative gate potential attracts positive charges under the interface in the semiconductor (holes in the p-type Si in the case of Fig. 2.2a). This results in an enhanced concentration of majority carriers (holes for p-type substrate), called accumulation, at the interface of oxide and semiconductor. When a positive gate voltage is applied, negative charges are introduced near the semiconductor and oxide interface. This, at first, is due to the holes being pushed away from the semiconductor surface, leaving behind a depletion region consisting of uncompensated acceptor ions as illustrated in Fig. 2.2b. As the positive gate potential increases, the surface depletion region is widened. Accordingly, the total electrostatic potential variation, as represented by the energy band bending, increases so that the midgap energy  $E_i$  crosses over the quasi-Fermi level  $E_F$  of the semiconductor. Beyond this point, the concentration of

minority carriers (electrons in this case) is larger than that of the majority carriers (holes) near the semiconductor and oxide interface. Therefore, the surface is rich in minority carriers, so called under inversion condition, as shown in Fig. 2.2c. Similar results can be obtained for n-type semiconductors when the gate bias is reversed.

To derive the capacitance – voltage (C-V) characteristics of the MOS structure, we need to develop a relation for the charge in the semiconductor to the surface band bending potential  $\psi_s$ . A p-type semiconductor is used to illustrate the C-V characteristics as show in Fig. 2.3. An arrow pointing down represents a positive potential. Band bending potential ( $\psi$ ) is measured with respect to midgap energy ( $E_i$ ) as a function of the distance  $x$  from the interface of oxide and semiconductor. It is defined to be zero in the bulk of the semiconductor, which indicated that gate voltage drop was only applied across the oxide and the semiconductor surface. The surface potential  $\phi$  is defined as the potential difference between  $E_i$  and  $E_F$ , and therefore  $\psi(x)$  can be expressed as  $\phi(x) + \phi_F$ . The  $n$  and  $p$  are given as functions of either  $\psi(x)$  or  $\phi(x)$  by the following equations:

$$n(x) = N_D \exp (\psi(x) / \phi_t) = n_i \exp ( \phi(x)/ \phi_t) \quad (2.1a)$$

$$p(x) = N_A \exp (-\psi(x) / \phi_t) = n_i \exp (-\phi(x)/ \phi_t) \quad (2.1b)$$

where  $n_i$  is the intrinsic carrier concentration,  $\phi_t = kT/q$  is the thermal voltage ( $\sim 26$  mV at room temperature),  $N_D$  ( $N_A$ ) is the donor (acceptor) concentration.

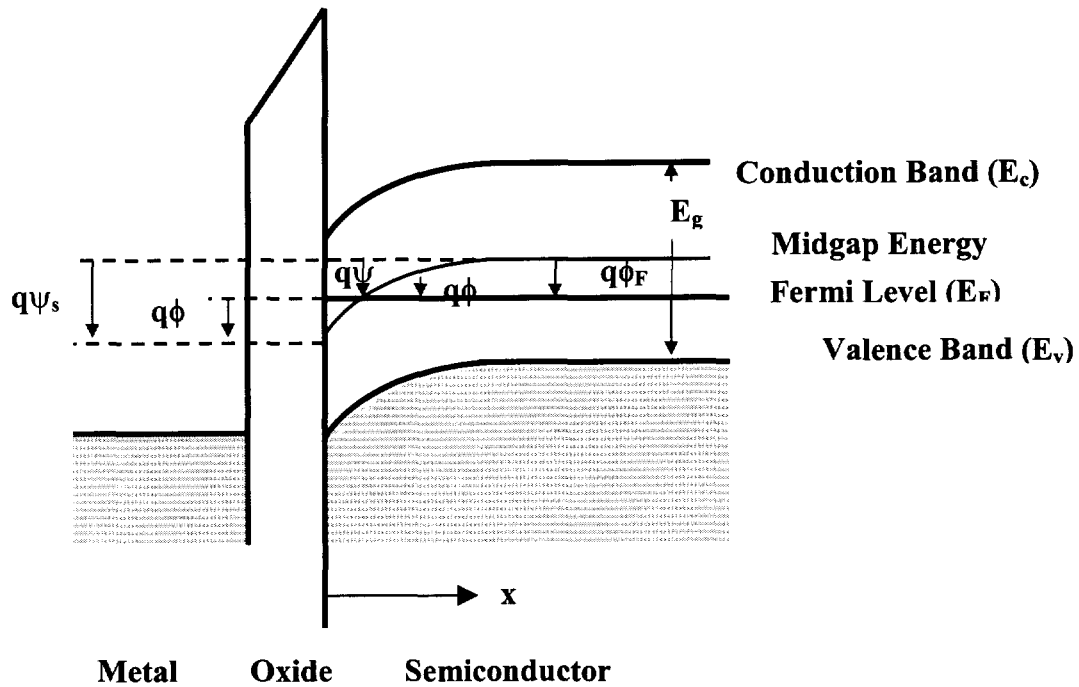


**Fig. 2.3 Energy band diagram at the surface of a p-type semiconductor. An arrow pointing down (up) denotes positive (negative) potential. Surface potential  $\phi_s$  is measured with respect to the Fermi level  $E_F$  at the interface. Surface band bending  $\psi_s$  is measured with respect to the intrinsic Fermi level  $E_i$  at the interface.**

From the above discussion together with Eqn. 2.1, The following regions of surface band bending potential can be distinguished [3]:

$\psi_s < 0$	Accumulation of holes (bands bending upward)
$\psi_s = 0$	Flat-band condition ( $n < p$ )
$\phi_F > \psi_s > 0$	Depletion of holes (bands bend downward)
$\psi_s = \phi_F$	Intrinsic condition at surface ( $n = p = n_i$ )
$2\phi_F > \psi_s > \phi_F$	Weak inversion ( $N_A > n > p$ )
$\psi_s > 2\phi_F$	Strong inversion ( $n > N_A$ )

The potential distribution in the semiconductor is described by one-dimensional Poisson equation:

$$\frac{d^2\psi(x)}{dx^2} = -\frac{\rho(x)}{\epsilon_s} = -\frac{q}{\epsilon_s} [p(x) - n(x) + N_D - N_A] \quad (2.2)$$

where  $p(x)$  and  $n(x)$  is the hole and electron concentration in silicon respectively,  $N_D$  and  $N_A$  are the density of ionized donors and acceptors respectively,  $\epsilon_s$  is the permittivity of the semiconductor,  $\rho(x)$  is the total space-charge density. Integrating Eqn. 2.1 in conduction with Eqn. 2.2 from the bulk toward the surface [4]

$$\int_0^{\psi_s/\phi_t} \frac{\partial \psi}{\partial x} d \left[ \frac{\partial \psi}{\partial x} \right] = -\frac{q}{\epsilon_s} \int_0^{\psi_s} [N_A (e^{-\psi/\phi_t} - 1) - N_D (e^{\psi/\phi_t} - 1)] d\psi \quad (2.3)$$

gives the relation between potential  $\psi$  and the electric field  $E$ :

$$E = -\frac{\partial \psi}{\partial x} = \pm \sqrt{2} \frac{\phi_t}{L_D} F(\psi, N_A) \quad (2.4)$$

with the positive sign for  $\psi > 0$  and the negative sign for  $\psi < 0$ . The extrinsic Debye length  $L_D$  which is a characteristic length of semiconductors, and  $F(\psi, N_A)$  are defined as

$$L_D = \sqrt{\frac{\epsilon_s \phi_t}{q N_A}} \quad (2.5a)$$

$$F(\psi, N_A) = \sqrt{e^{-\psi/\phi_t} + \psi/\phi_t - 1 + (n_i/N_A)^2 (e^{\psi/\phi_t} - \psi/\phi_t - 1)} \quad (2.5b)$$

At thermal equilibrium the depletion layer width of abrupt junction is about  $8L_D$  for Si. The surface electric field  $E_s$  is given by substituting  $\psi_s$  for  $\psi$  into Eqn. 2.4. By

Gauss's law, the total charge  $Q_s$  per unit area in the semiconductor required to produce the field  $E_s$  is:

$$Q_s \equiv -\epsilon_s E_s = \mp \sqrt{2} \frac{\epsilon_s \phi_t}{L_D} F(\psi_s, N_A) \quad (2.6)$$

The differential capacitance of the semiconductor is given by:

$$C_s \equiv \frac{\partial Q_s}{\partial \psi_s} = \frac{\epsilon_s}{\sqrt{2} L_D} \frac{|1 - e^{-\psi_s/\phi_t} + (n_i/N_A)^2 (e^{\psi_s/\phi_t} - 1)|}{F(\psi_s, N_A)} \quad (2.7)$$

The total capacitance  $C$  of a MOS system is a series combination of insulator capacitance  $C_i$  and the semiconductor capacitance  $C_s$ :

$$C = \frac{1}{1/C_i + 1/C_s} \quad (2.8)$$

$C_i$  is the oxide capacitance per unit area:

$$C_i = \frac{\epsilon_i}{t_i} \quad (2.9)$$

where  $\epsilon_i$  is the permittivity of the insulator (oxide in most cases) and  $t_i$  is the thickness of the insulator. When a gate voltage is applied to the MOS structure, the ideal MOS capacitance – voltage (C-V) characteristics for a p-type semiconductor can be described by the C-V curves at high- and low-frequency conditions as shown in Fig. 2.4.

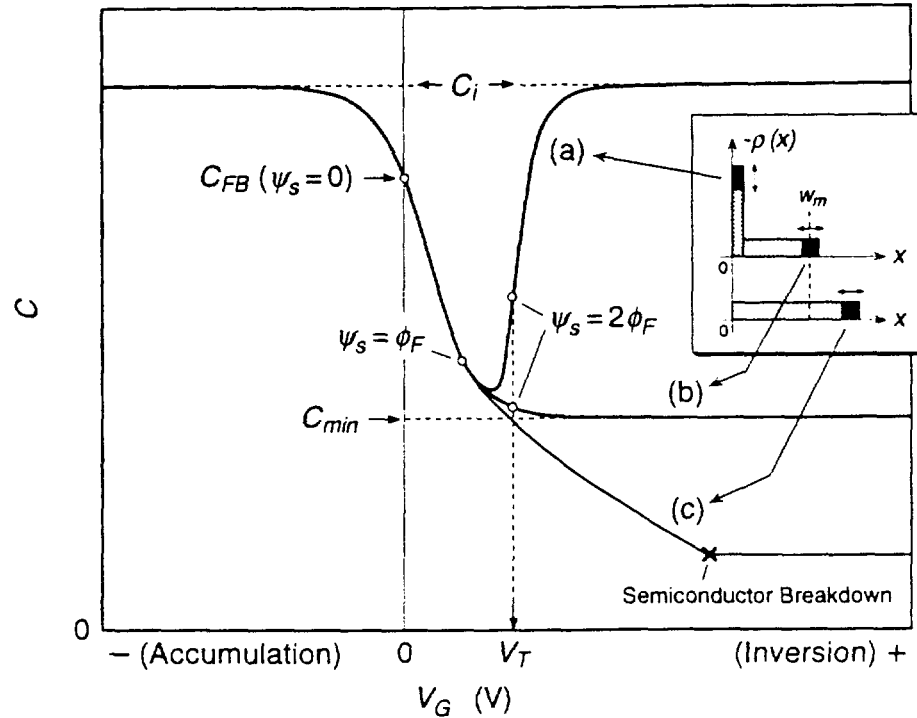


**Fig. 2.4 MOS capacitance-voltage characteristics under (a) low frequency, (b) high-frequency, and (c) deep-depletion conditions**  
[5]

For the low frequency C-V curve (a) in Fig. 2.4, accumulation of holes occurs with a negative gate bias ( $V_g < 0$ ) and  $Q_s$  (hole charge in this case) dominates. Therefore the differential capacitance of the semiconductor  $C_s$  is much larger than the capacitance of the insulator  $C_i$ . As a result, the total  $C$  of the MOS is close to its maximum  $C_i$ . As  $V_g$  is increased to be slightly positive, a depletion layer, which may act as a dielectric layer of thickness  $w$  in series with the insulator, forms and widens near the semiconductor surface. Therefore the total capacitance  $C$  decreases substantially according to

$$C = \frac{1}{t_i / \epsilon_i + w / \epsilon_s} \quad (2.10)$$

As  $V_g$  is further increased to exceed the so called threshold voltage  $V_t$  at which strong inversion occurs ( $\psi_s \approx 2\phi_F$ ), total capacitance  $C$  increases again after showing a minimum and then approaching the maximum  $C_i$ , since the charges  $Q_s$  in the inversion layer of semiconductor increases dramatically by a slight increase of the surface band bending potential  $\psi_s$ . Once strong inversion occurs,  $w$  reaches its maximum  $w_m$ . Simplifying  $F$  in Eqn. 2.5b by expressing it only through the second term and equating  $Q_s$  at  $\psi_s \approx 2\phi_F$  with Eqn. 2.6 to  $Q_D = qN_A w_m$ ,  $w_m$  is given by:

$$w_m \approx \sqrt{\frac{2\epsilon_s 2\phi_F}{qN_A}} = 2\sqrt{\frac{\phi_F}{\phi_i}} L_D \quad (2.11)$$

To measure the differential capacitance, the AC signal of small amplitude  $\delta V$  with the angular frequency  $\omega$  ( $\omega = 2\pi f$ ,  $f$  being frequency) is superimposed onto the DC voltage  $V_g$ . Comparing the curves a and b in Fig. 2.4, it should be noticed that the increase of capacitance in inversion region occurs at low frequencies where the recombination-generation rates of minority carriers can keep up with the small signal variation and lead to charge exchange with the inversion layer. These minority carriers will contribute an additional capacitance  $C_{it}$  to the measured low frequency C-V curve. At low frequencies, the C-V characteristics are represented by the equivalent circuit in Fig. 2.5. The total capacitance can be calculated using Eqn. (2.12).

$$\frac{1}{C_{LF}} = \frac{1}{C_i} + \frac{1}{C_s + C_{it}} \quad (2.12)$$

At higher frequencies, interface traps lag behind the small-signal AC change with the minority-carrier response time. The capacitance at high frequency can be given by:



$$C_{HF} = \frac{C_i C_s}{C_i + C_s} \quad (2.13)$$

This capacitance corresponds to the equivalent circuit shown in Fig. 2.6.

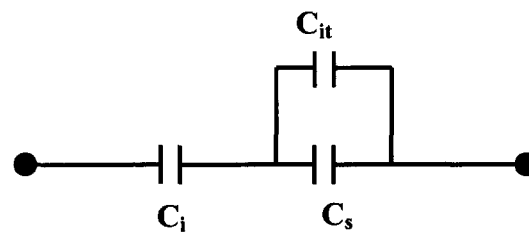


**Fig. 2.5 Low frequency equivalent circuit of the MOS**

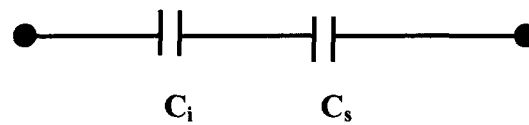


**Fig. 2.6 High frequency equivalent circuit of the MOS capacitor**

An experimental set of low frequency C-V data is shown in Fig. 2.7. It is obvious that for this Si-SiO<sub>2</sub> system the onset of low frequency curves occurs at  $f \leq 100$  Hz.

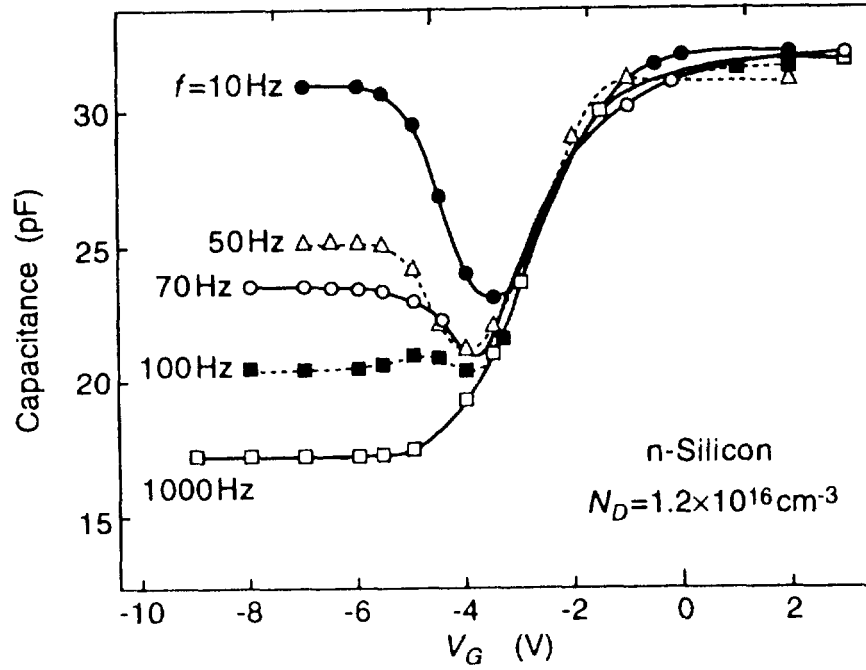


**Fig. 2.7 MOS C-V curves measured at room temperature with frequency as a parameter . The substrate is n-type.**  
[6]

The capacitance-voltage characteristics of an ideal MOS structure vary not only with the frequency but also the thickness of the oxide layer and the doping concentration of the substrate. As the thickness  $d$  is made thinner or the substrate doping is made lighter, a large variation of capacitance is observed, as illustrated in Fig. 2.8. In these figures, the dielectric constant  $k$  ( $= \epsilon_i / \epsilon_0$ ) of  $\text{SiO}_2$  is approximately three times smaller than that of silicon ( $\sim 11.8$ ),  $\epsilon_0$  being the permittivity of vacuum. In order to replace another insulator for  $\text{SiO}_2$ , simply replace its physical thickness  $t$  with an electrically equivalent thickness of  $\text{SiO}_2$ ,  $t_{eq,ox}$  defined as

$$t_{eq,ox} = \frac{\epsilon_{ox}}{\epsilon_i} t = \frac{3.9}{\epsilon_i / \epsilon_0} t \quad (2.14)$$

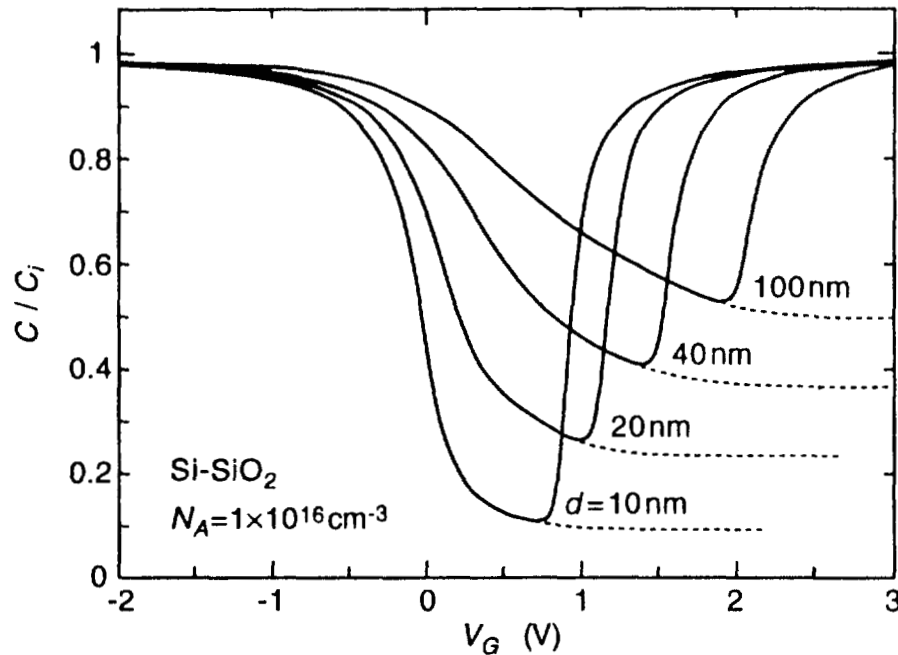


**Fig. 2.8 MOS C-V characteristics as a function of the oxide thickness. Solid lines correspond to low frequency and dashed lines represent high frequency. The substrate is p-type silicon.**

[7]

## 2.2 Charges in a MOS system

An ideal MOS capacitor does not contain any defect charges. However, for a real MOS capacitor there exist different defect charges especially near the Si-SiO<sub>2</sub> interface where the chemical composition is considered not to be stoichiometric (SiO<sub>x</sub>:  $x < 2$ ) unlike in the bulk. As shown in Fig. 2.9, there are four distinct types of charges in the Si-SiO<sub>2</sub> system:  $Q_f$  the fixed charges, located very near the interface but can not exchange charges with the semiconductor;  $Q_{it}$  the interface -state charges, located very close to the

interface and have energy states close to the Fermi level ( $E_F$ ) within the forbidden bandgap as to be able to exchange charges with the semiconductor;  $Q_{ot}$  oxide trapped charges, the trap sites are distributed throughout the bulk of the oxide;  $Q_m$  mobile ionic charges, results from alkali-metal ions (mainly sodium) that are easy to be absorbed in the oxide under bias-temperature aging conditions. Among the four kinds of charges,  $Q_f$  causes the parallel shift  $\Delta V$  along the V axis in a C-V curve, i.e.

$$\Delta V = -\frac{Q_f}{C_i} = -\frac{Q_f t_i}{\epsilon_i} \quad (2.15)$$

where  $t_i$  is the thickness of insulator (oxide) and  $\epsilon_i$  is the permittivity of the insulator.

The effects of  $Q_{it}$  on C-V curve are more complicated.  $Q_{it}$  will not simply shift the C-V curve in parallel but stretch them out, because the interface states occupancy varies with the gate bias. Since the interface state levels are distributed across the energy band gap, the interface state density is described as  $D_{it} \equiv \partial N_{it} / \partial E$  in units of  $\text{cm}^{-2}/\text{eV}$ . There are two types of interface states, acceptor type and donor type. Acceptor -like interface states are negative when filled with electrons and neutral when empty, whereas donor-like ones are neutral when filled and positive when empty. It is generally considered that interface states above the midgap energy are acceptor type while those below midgap are donor type. An interface state can interact with the silicon conduction band by capturing or emitting an electron and with the silicon valence band by capturing or emitting a hole.

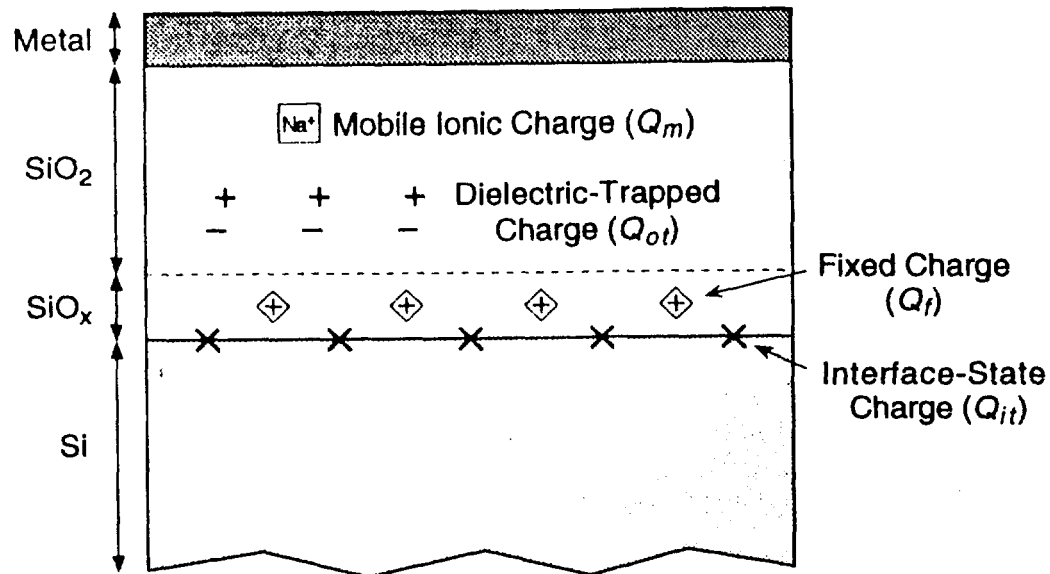


**Fig. 2.9 Four categories of oxide charges in the MOS system.**  
[8]

Interface states can be extracted from capacitance, conductance and sub-threshold measurements. Terman used the theoretical and measured high frequency C-V data to extract the interface state density [9]. The interface state density can also be obtained from the low frequency C-V measurement, a technique developed by Berglund [10]. The difference of the theoretical and measured low frequency C-V curve is due to the interaction of interface states with the silicon substrate. Castagne and Vapaille proposed a method to calculate interface state density using both high frequency and low frequency C-V data [11]. The conductance method, proposed by Nicollian and Goetzberger in 1967, is considered the most sensitive approach to determine  $D_{it}$  [12]. It is based on the measurement of the equivalent parallel conductance  $G_p$  of a MOS capacitor as a function of bias and frequency. The charge pumping method, originally proposed by Brugler in 1969 [13], is suitable for interface states measurement on small geometry MOSFET's

states distribution from the charge pumping effects [14]. The advantage of charge pumping method is the direct measurement of the current that is proportional to  $D_{it}$  and the fact it can be used to measure regular MOSFET devices without preparing extra test structures.

### 2.3 Carrier transport in dielectric films

The conductance of an insulating thin film is assumed to be zero in an ideal MOS structure. Real insulators, however, show carrier conductance when the electric field or temperature is sufficiently high. An estimation of the relationship between electric field and the permittivity can be obtained from

$$E_i \epsilon_i = E_s \epsilon_s \quad (2.16)$$

where  $E_i$  and  $E_s$  are electric fields in insulator and semiconductor, respectively, and  $\epsilon_i$  and  $\epsilon_s$  are the corresponding permittivities. For the Si-SiO<sub>2</sub> system, the field for silicon at avalanche breakdown is about  $3 \times 10^5$  V/cm, the corresponding field in oxide is about three time larger ( $\epsilon_{Si}/\epsilon_{SiO_2} = 11.9/3.9$ ), that is, about  $10^6$  V/cm. Under such an electric field, the conduction of electron and hole in the oxide film is negligible even at elevated temperatures. However, when sufficiently high electric fields  $E$  (V/cm), are applied to dielectric films, the response is passage of a current density  $j$  (A/cm<sup>2</sup>). If  $E$  is small, the response is linear or ohmic, and the conductivity ( $\sigma$ ), given by  $j/E$ , is independent of  $E$ . For larger applied fields the  $j$ - $E$  relationships defining charge transport through dielectric films are more complex. Depending on the mechanism, the conduction process is described in Table 2-1 [15]. In most cases the magnitude of  $j$  is strongly temperature-dependent according to Maxwell-Boltzmann relationship.

**Table 2-1 Conduction processes in dielectric films**

Process	j-E relationships	Voltage(V), Temperature(T) dependence
1.Schottky emission	$j = A^* T^2 \exp \left[ \frac{-q(\Phi_B - (qE/(4\pi\epsilon_i))^{1/2})}{kT} \right]$	$\approx T^2 \exp \left[ \frac{+aV^{1/2} - b}{T} \right]$
2. Frenkel-Poole emission	$j = B \exp \left[ \frac{-q(\Phi_B - (qE/(\pi\epsilon_i))^{1/2})}{kT} \right]$	$\approx V \exp \left[ \frac{+a'V^{1/2} - b}{T} \right]$
3. Tunneling	$j = \frac{CE^2}{\Phi_B} \exp \left[ -\frac{8\pi(2m)^{1/2}(q\Phi_B)^{3/2}}{3hqE} \right]$	$\approx V^2 \exp(-\frac{c}{V})$
4.Space-charge- limited	$j = \frac{4\epsilon_0(2q/m)^{1/2}}{9} \frac{E^{3/2}}{t^{1/2}}$	$\approx V^{3/2}$
5.Ohmic (intrinsic)	$j = ET^{3/2} \exp \left[ -\frac{E_g}{2kT} \right]$	$\approx VT^{3/2} \exp \left[ -\frac{eE_g}{T} \right]$
6.Ionic conduction (low field)	$j \approx \frac{E \exp[-E_a/kT]}{T}$	$\approx \frac{V \exp(-E_a/T)}{T}$
7.Ionic conduction (high field)	$j \approx \sinh[qaE/kT] \exp[-E_a/kT]$	$\approx \sinh(gV/T) \exp(-hE_a/T)$

$A^*$  = Richardson constant,  $\Phi_B$  = barrier height,  $E$  = electric field,  $\epsilon_i$  = insulator dielectric constant,  $\epsilon_0$  = permittivity of free space,  $m$  = effective electron mass,  $t$  = insulator thickness,  $h$  = Planck's constant,  $E_g$  = insulator energy gap,  $E_a$  = activation energy for ion creation and motion. Constants  $B$ ,  $C$ ,  $a$ ,  $a'$ ,  $b$ ,  $c$ ,  $e$ , and  $f$  are independent of  $V$ .

The Schottky emission process is similar to the current transport in the metal-semiconductor contacts that is mainly due to (1) majority carriers transport from the metal over the potential barrier into the semiconductor at moderate temperatures (e.g., 300K). The other contributions to carrier transport from thermionic emission across the metal-insulator interface or the insulator-semiconductor interface are (2) quantum-mechanical tunneling of electrons through the barrier, (3) recombination in the space-charge region and (4) electron injection from the metal to the semiconductor under negative gate bias. Fig. 2.10 shows the transport processes in the Schottky emission under forward bias. A plot of  $\ln(J)$  versus  $\sqrt{E}$  yields a straight line where  $E$  is the electric field and  $J$  is the current density. Meanwhile, a plot of  $\ln(J/T^2)$  versus  $1/T$  would also show a straight line where  $T$  denotes the temperature.

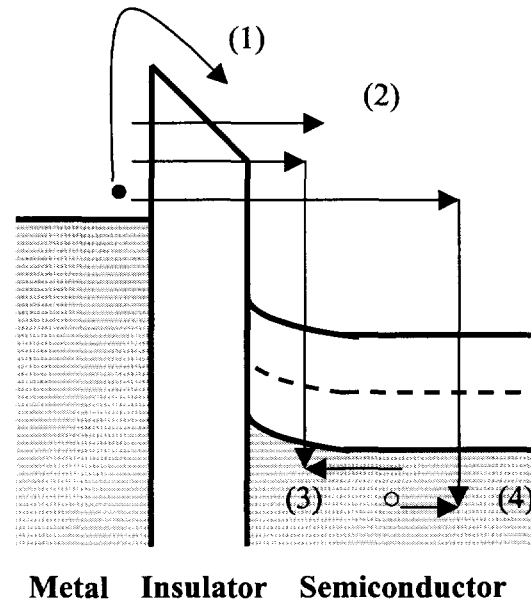


**Fig. 2.10 Four basic transport processes in Schottky emission.**  
[16]



The Frenkel-Poole emission, shown in Fig. 2.11, is due to the field-enhanced thermal excitation of trapped electrons into the conduction band. For trap states with coulomb potentials, the expression is virtually identical to that of the Schottky emission. The barrier height is the depth of the trap potential well. The tunneling is caused by the field-assisted electron emission into the conduction band or by electrons tunneling from metal Fermi level into the insulator conduction band. The tunneling process is substantially

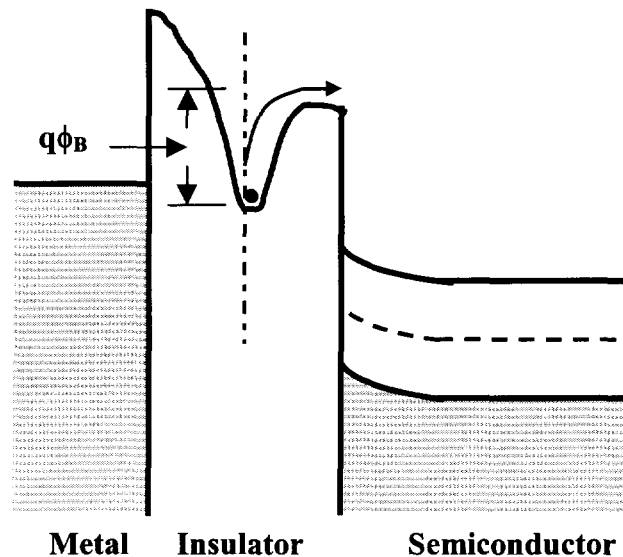


**Fig. 2.11 Illustration of Frenkel-Poole emission.  $\phi_B$  is the barrier height.**  
[17]

dependent on the applied voltage and independent of the temperature. Fowler-Nordheim tunneling occurs at a large electric field above 6-7 MV/cm. If electric field  $E_i$  is further increased beyond 10~12 MV/cm, depending on the dielectric film thickness, dielectric breakdown occurs. When the thickness of dielectric films is reduced to 4~5nm, direct

tunneling becomes dominant. The tunneling processes are shown in Fig. 2.12. A simple criterion that direct tunneling occurs is that:

$$V_i \equiv E_i t < \Phi_B \quad (2.17)$$

which means that electrons go into the conduction band of silicon rather than of  $\text{SiO}_2$ .  $V_i$  is the potential across the oxide layer of thickness  $t$ .  $\Phi_B$  is the barrier potential from metal to oxide. Substituting  $\Phi_B = 3.2$  V and  $E_i = 7$  MV/cm for the onset of F-N tunneling into Eqn. 2.17, for example, we approximately find for the Si- $\text{SiO}_2$  system that direct tunneling is dominant when the dielectric thickness is less than 4.5 nm. This agrees with the experimental observations. Due to the mechanism of direct tunneling, it has much smaller dependence on the gate voltage  $V_g$  compared to the F-N tunneling. Therefore, the current in such a low- $V_g$  range at which MOSFET's are operated in practice is undesirably increased, setting a fundamental constraint on MOS technology.

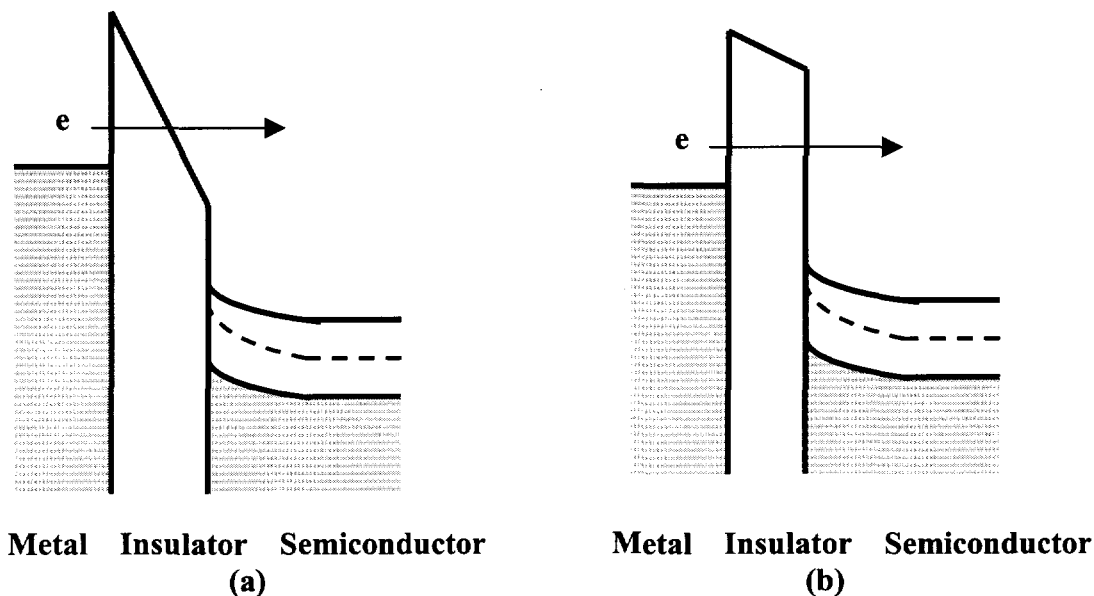


**Fig. 2.12 Diagram of tunneling processes in insulating films. (a) Direct Tunneling (b) Fowler-Nordheim Tunneling**

The space-charge-limited current is due to the carriers injected into the insulator, where no compensating charge is present. At low voltage and high temperature, conduction current is formed by thermally excited electrons hopping from one isolated state to the next, this leads to an ohmic characteristic exponential dependence on temperature. The ionic conduction is similar to diffusion processes. The dc ionic conduction is not obvious during the time the voltage is initially applied since ions can not be readily injected or extracted from the insulator. After the initial current flow, positive and negative space charges will build up at the metal-insulator and insulator-semiconductor interfaces, causing a distortion of the potential distribution. As the voltage is removed, large internal fields remain which cause some ions to flow back to their equilibrium position.

Intrinsic tunneling and leaky paths due to neutral trapping centers created by plasma exposure are the major leakage mechanisms in MOS devices with untrathin oxide [18]. Thin gate oxides are subjected to plasma process induced charging damage since so many plasma steps are used and plasma damage is cumulative. Plasma charging may cause electrical stress of the gate oxide that can result in reduced device yield. When charging stress is milder, interface traps are generated and the characteristics of MOS devices may exhibit a higher range of variability. Reliability of devices is also degraded. The nature of the oxide degradation under plasma charging relies on the Fowler-Nordheim (F-N) current being forced through the thin oxide layer under electrical stress. Degradation of the gate oxide leakage depends on bias polarity, temperature, and gate material such as boron or phosphor doped poly silicon gates. The Stress-Induced-Leakage-Current (SILC) in gate oxide has been studied extensively since it may impose constraints on dielectric thickness scaling. It was reported that for stress voltage below 5 V and for gate oxide thickness less than 3.5 nm, SILC is caused by tunneling via interfacial traps, rather than through bulk oxide traps [19].

## 2.4 MOSFET Transistor

MOSFET transistor is a four-terminal structure including gate, substrate, source and drain, as shown in Fig. 2.13. There are two types of transistors based on the carriers in the channel: n-type (n-channel) and p-type (p-channel). In this section, operation theory and equations of n-channel on p-type substrate are discussed. Similar results can also be applied to p-channel device with corresponding polarity modifications.

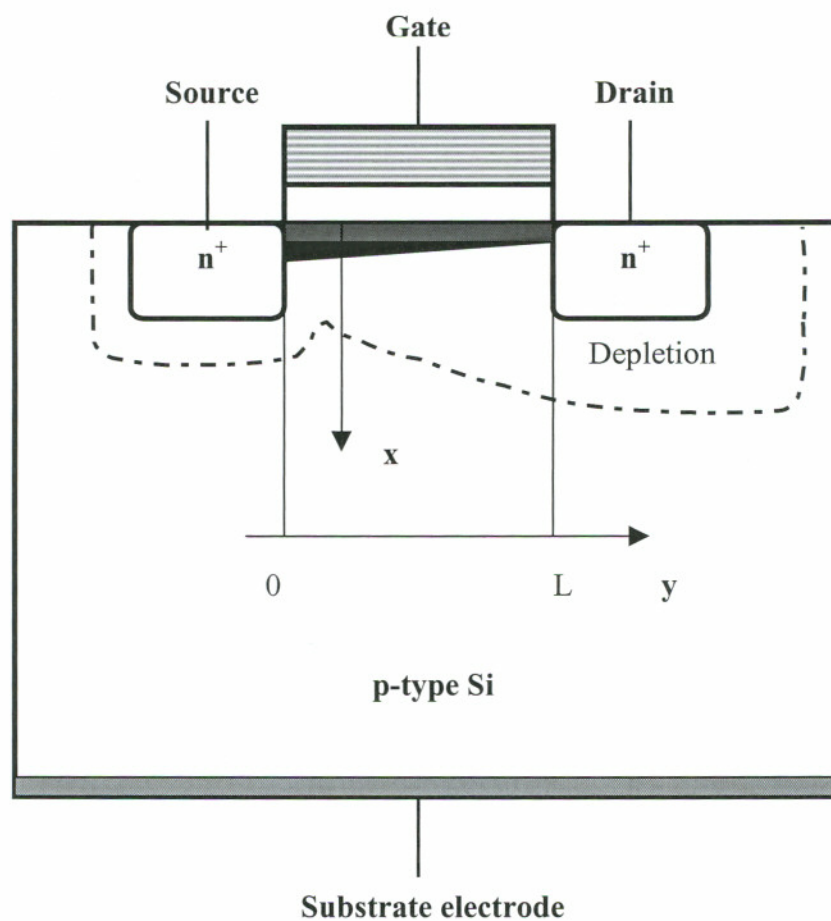


Fig. 2.13 Cross section of a MOSFET

When the gate voltage  $V_g$  is larger than the threshold voltage  $V_{th}$ , electrons in the substrate will be attracted to the semiconductor surface, forming so called n-channel underneath the gate oxide. The potential difference between source and drain will cause electrons in the n-channel to drift from source to drain therefore current flows through the channel. The threshold voltage is an important parameter for the MOSFET device. It is the minimum gate voltage needed to turn on the transistor. The threshold voltage for large-geometry devices on uniformly doped substrates with no short- or narrow-channel effects is given by

$$V_{th} = V_{FB} + 2\phi_F + \frac{\sqrt{2q\epsilon_{Si}N_A(2\phi_F)}}{C_i} \quad (2.18)$$

$$\phi_F = \frac{kT}{q} \ln\left(\frac{N_A}{n_i}\right) \quad (2.19)$$

where  $V_{FB}$  is the flat band voltage, substrate and source are both grounded. The threshold voltage for non-uniformly doped, ion-implanted devices depends on the implant dose as well.  $C_i$  is the gate dielectric capacitance, which increases with the reduction of gate dielectric thickness. Additional corrections are needed for short- or narrow-channel devices. The charges that exist at interface of semiconductor and oxide will also cause a shift of the threshold voltage. In this case, the threshold voltage can be expressed as

$$V_{th} = V_{FB} + 2\phi_F + \frac{\sqrt{2q\epsilon_{Si}N_A(2\phi_F)}}{C_i} + \frac{Q_{it} + Q_{ot}}{C_i} \quad (2.20)$$

where  $Q_{it}$  are the interface charges and  $Q_{ot}$  are the oxide trapped charges. The scaling of oxide thickness results in an increase of oxide capacitance. Therefore, the threshold voltage could be reduced.

As a large enough gate voltage is applied to the MOSFET device, an n-type inversion layer will be formed and electrons in this n-channel will flow from source to drain with  $V_D > 0$ . There are two cases of small and large  $V_D$  to be considered. For a small  $V_D$ , inversion layer charges are uniformly distributed under the gate oxide and current flows through the conducting channel. The channel acts as a resistor in this case so that the drain current increases proportionally to  $V_D$ . This is called linear region. As  $V_D$  is further increased, electrons in the inversion layer close to the drain end will be attracted to the drain and this region will be depleted of mobile electrons. Therefore the channel resistance will be increased until eventually the inversion layer charge becomes zero (called pinchoff) at the drain end.  $V_D$  at which saturation occurs is denoted by the saturation drain voltage  $V_{Dsat}$ . Once  $V_D$  exceeds the saturation voltage, the pinchoff point will move towards the source end leaving a depletion region behind at the surface. The drain current will eventually remain constant  $I_D$  because it depends on the voltage drop (fixed at  $V_{Dsat}$ ) inside the channel. This region is called saturation.

To derive the  $I_D$ - $V_D$  characteristics, only drift current is considered for simplicity. The mobility is assumed to be constant throughout the channel. Integrating the equation for current density  $J$  ( $v_d$ : drift velocity of the electrons) [3]

$$J = -qn(x)v_d \quad (2.21)$$

from the surface towards the point  $x = x_1$  at which the intrinsic Fermi level  $E_i$  intersects  $E_{Fn}$  gives

$$I_D = WQ_I\mu_n E_{\parallel} = -WQ_I\mu_n \partial V / \partial y \quad (2.22)$$

where  $E_{\parallel} \equiv -\partial V / \partial y$ ,  $W$  is the width of the channel, and  $Q_I$  is the inversion charge per unit area defined by

$$Q_I = - \int_0^{x_I} qn(x)dx \quad (2.23)$$

There are several methods to calculate the  $Q_I$  in Eqn. 2.23. Some approaches are very complicated and time-consuming. Usually a gradual-channel approximation is used ( $V_D \ll 2\phi_F$ , in this case) and a simple drain current calculation yields

$$I_D = \frac{W}{L} \mu_n C_i (V_g - V_{th} - V_D / 2) V_D \quad (2.24)$$

where the threshold voltage  $V_{th}$  is given by

$$V_{th} = 2\phi_F + \frac{1}{C_i} \sqrt{2\varepsilon_s q N_A \cdot 2\phi_F} = 2\phi_F + K \sqrt{\phi_i \cdot 2\phi_F} \quad (2.25)$$

$K$  is a characteristic ratio of semiconductor capacitance to the gate dielectric capacitance  $C_i$  defined by

$$K = \frac{\sqrt{2\varepsilon_s}}{C_i} \frac{1}{L_D} = \frac{\sqrt{2\varepsilon_s q N_A / \phi_i}}{C_i} \quad (2.26)$$

which includes the Debye length  $L_D$  as described in Chapter 2.1. Eqn. 2.24 reflects the drain current in the so-called linear region. In this region, for a given gate voltage  $V_g$ ,  $I_D$  first increases linearly with  $V_D$ , then gradually levels off, and reaches its maximum  $I_{Dsat}$  at  $V_{Dsat}$ . Solving  $\partial I_D / \partial V_D = 0$  with Eqn. 2.24 produces

$$V_{Dsat} = V_g - V_{th} \quad (2.27)$$

$I_{Dsat}$  is then obtained by substituting Eqn. 2.27 into Eqn. 2.24,

$$I_{Dsat} = \frac{W}{L} \mu_n C_i \frac{(V_g - V_{th})^2}{2} \quad (2.28)$$

which is used to describe  $I_D$  with  $V_D > V_{Dsat}$ . A typical  $I_D - V_D$  curve is shown in Fig. 2.14.

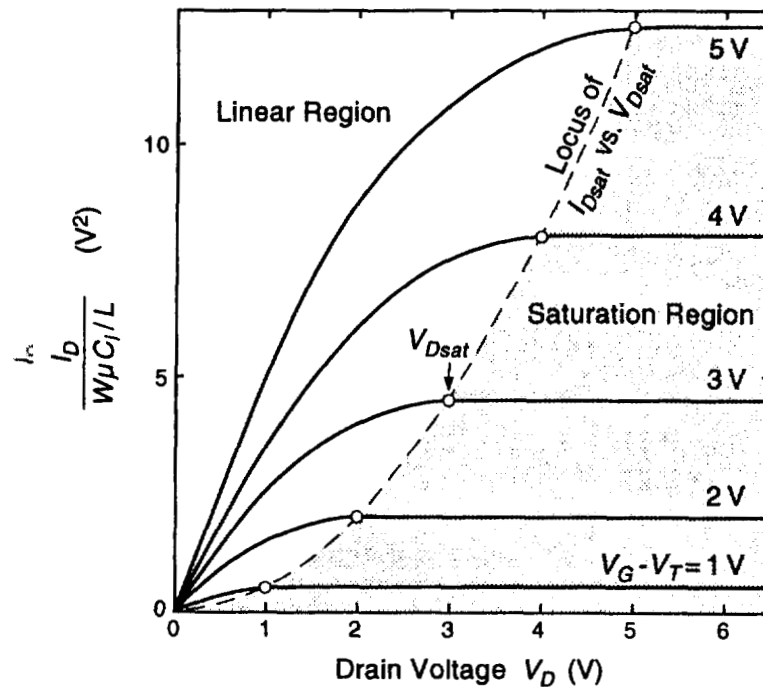


**Fig. 2.14 Idealized saturation characteristics ( $I_D$  vs.  $V_D$ ) of an n-channel MOSFET. The dashed line indicates the locus of  $I_{Dsat}$  vs.  $V_{Dsat}$ .**

[3]

According to the drain current expression in the linear region,  $I_D$  should be zero for  $V_g < V_{th}$ . This is because when the drain current was explored, only drift current was considered. In reality, there will be a current flow in the channel even gate voltage is



smaller than the threshold voltage. Unlike the drift current in the strong inversion, the subthreshold current  $I_D$  in weak inversion is dominated by diffusion due to the difference between the electron density at the source and drain. This current is especially important for low-voltage, low-power applications such as CMOS logic and DRAM memory devices.

## 2.5 Scaling issues and limitations

Scaling down or shrinking of the device size has been extensively used to improve device and circuit performance. This enhanced performance includes a faster switching speed, low power dissipation, smaller device and circuit areas and high capacity of integration. The initial scaling concept, the constant – field scaling law, was proposed by IBM researchers [20] in mid 1970s to keep the internal electric fields constant by reducing all geometry factors and voltage by the single scaling factor  $\lambda$  as shown in Table 2-2. The geometric factors include the channel length  $L$ , channel width  $W$ , source/drain junction depth  $x_j$ , and the gate dielectric thickness  $d$ . The doping density  $N_B$  is increased by  $\lambda$  so that the depletion layer depth is reduced by  $\lambda$ , under the biases reduced by  $\lambda$ . Therefore, undesirable two-dimensional effects such as short channel effects remain under control. The scaling reduces the drain current drive  $I_D$  by  $\lambda$ , the switching delay by  $\lambda$ , and the power dissipation by  $\lambda^2$ . This theory was confirmed by the successful fabrication of 1- $\mu\text{m}$  channel MOSFET showing the proper characteristics as expected with respect to traditional 5- $\mu\text{m}$  technology.

Since then, the constant –field scaling law has acted as a concise guide for device shrinking. However, as devices continue to be scaled down to deep-submicrometer, the constant-field scaling law can not hold any more. In particular, the voltage for the above 1- $\mu\text{m}$  MOSFET device was already reduced to 1 V. Therefore, in the mid 1980s, the IBM researchers modified their theory [21] to the generalized scaling law that reduces the

voltage by a factor  $\kappa$  generally smaller than the factor  $\lambda$ . By resetting the starting voltage to 2.5V for the 1- $\mu\text{m}$  channel FET, it was demonstrated that a 1/4- $\mu\text{m}$  channel FET with  $d = 5 \text{ nm}$  ( $\lambda = 4$ ) operates well under a reduced bias ( $\kappa = 2.5$ ) of 1 V. The generalized design does not require major modifications of the state-of-art MOS technology since  $\kappa < \lambda$ , but it requires an evolution toward much thinner gate dielectrics and the proportionally reduced fabrication tolerance since thickness of gate dielectric  $d$  is reduced by the same factor  $\lambda$ .

In practice, several limitation factors restrict the voltage to be scaled as much as the device dimensions. The temperature deviation of  $V_{\text{th}}$  leads to large threshold fluctuation if extended operation temperatures would be used, i.e. from  $-55^\circ\text{C}$  to  $+135^\circ\text{C}$  [22]. The subthreshold characteristics are nonscalable. The above two issues prevent  $V_{\text{th}}$  from being scaled proportionally with the device dimensions down to less than roughly 0.4~0.5V[23]. Otherwise the subthreshold current and power dissipation will be undesirably increased. There are other concerns such as the non-scalability of junction built-in potential and the transition region, where the inversion charge  $Q_{\text{I}}$  is nonlinearly increased with  $V_{\text{g}}$ . In addition to the above fundamental limits associated with the physical parameters of  $\phi_{\text{t}}$ ,  $\phi_{\text{F}}$ , and  $E_{\text{g}}$ , there are other practical limiting factors for scaling. The circuit requirement on functional capability with appropriate noise immunity prevents the power supply voltage from being less than about  $4V_{\text{th}}$  [23, 24]. In fact the power supply voltage is kept constant as long as possible, which is called constant-voltage scaling. The nonscalability of the interconnection line length as well as the parasitic capacitance lead to slower response time with progress of scaling. The major delay for a circuit comes from the interconnection delay, which can not be solved by scaling the transistor size. Historically designers tried to expand circuits to reduce the interconnection length.

**Table 2-2 Scaling factors associated with important device parameters for the constant-field scaling law, generalized one and the practical constant-voltage scaling law.**

Parameter		Expression	Scaling Law		
			Constant E	Generalized	Constant V
Dimension		$W, L, d, x_j$	$1 / \lambda$		
Voltage		$V_{DD}, V_T$	$1 / \lambda$	$1 / \kappa$	1
Electric Field		$E_i, E_{  }$	1	$\lambda / \kappa$	$\lambda$
Doping Density		$N_B$	$\lambda$	$\lambda^2 / \kappa$	$\lambda^2$
Circuit	Capacitance	$C_G = A \epsilon_i / d$	$1 / \lambda$		
	Current	$I_D$	$1 / \lambda$	$\lambda / \kappa^2$	$\lambda$
	Gate Delay Time	$t_{pd} = C_G V_{DD} / I_D$	$1 / \lambda$	$\kappa / \lambda^2$	$1 / \lambda^2$
	Power Dissipation	$I_D V_{DD}$	$1 / \lambda^2$	$1 / \lambda \kappa$	$1 / \lambda$
Interconnection	Line Resistance	$R_L = \rho l / A_L$	$\lambda$		
	Time Constant	$R_L C_L$	1		
	Current Density	$I_D / A_L$	$\lambda$	$\lambda^3 / \kappa^2$	$\lambda^3$

All the fundamental and practical limiting factors call for supply voltage and threshold voltage to be reduced less than the traditional constant-field scaling would require. For modern sub-micron devices, the constant-voltage scaling law has become a practical guide for device shrinking. Therefore, the lateral and normal electric fields in a sub-micron MOSFET have been considerably increased. As the power supply voltage was maintained at 5V for over five generations from 3- $\mu\text{m}$  to 0.6- $\mu\text{m}$  design rules, the gate dielectric field has already been close to its highest allowable value of  $\sim 3 \text{ MV/cm}$ . Due to the increased electric fields, various concerns on device and circuit performance and reliability have caught attention in semiconductor field.

As recent development of ULSIs have required further scaling of MOSFETs down to deep sub-micron, the gate oxides are thinned to nanometers or even angstroms, and requirements on the quality and reliability become more severe. There are two alternative ways to resolve this problem, one is to keep the gate oxide unchanged and scale other device parameters such as operating voltage, and the other method is to replace the current gate oxide  $\text{SiO}_2$  with a high dielectric constant insulator to achieve very thin equivalent  $\text{SiO}_2$ . With the continuous scaling of device, operation voltage can not remain at the current value for 0.13  $\mu\text{m}$  and smaller MOSFETs. Searching for high dielectric constant ( $k$ ) material provides a resolution for future IC fabrication.

## 2.6 High Dielectric Constant Materials

Dielectric materials, also called insulators are very important in IC fabrication. They are used for insulation between conducting layers, for diffusion and ion implantation masks, for diffusion from doped oxides, for capping doped films to prevent the loss of dopants, for gettering impurities, and for passivation to protect devices from impurities, moisture, and scratches [25]. The general characteristics of dielectric usually comprise strong ionic or directed covalent bonds, brittle mechanical behavior at ordinary

temperatures, very high resistivity and transparent to visible and infrared light. A dielectric is polarized in the presence of an electric field. Dipole moments are produced as an external electric field is applied to the dielectric. There are several parameters used to describe this phenomenon such as electric field  $E$ , electric displacement  $D$ , the polarization  $P$  together with the electric susceptibility  $\kappa$ , and the dielectric constant  $\epsilon$  or  $k$ . The relationships of above factors are

$$D = \epsilon^* E = \epsilon_0 E + P \quad (2.29)$$

$$P = \kappa \epsilon_0 E \quad (2.30)$$

$$\epsilon = 1 + \kappa \quad (2.31)$$

where  $\epsilon_0$  is the permittivity of vacuum,  $\epsilon^*$  is the permittivity of the material and the relative dielectric constant is

$$\epsilon = \frac{\epsilon^*}{\epsilon_0} \quad (2.32)$$

For a dielectric material containing different kinds of atoms with concentration  $N_i$  and polarizability  $\alpha_i$ , and assuming that different kinds of atoms act independently of one another, the relationship between the macroscopic quantity  $\epsilon$  and the atomic quantity  $\alpha_i$  is given by [26]

$$\sum_i N_i \alpha_i = 3 \frac{\epsilon - 1}{\epsilon + 2} \quad (2.33)$$

This is known as the Clausius-Mossotti formula. To relate the dielectric properties to the optical properties and consider time-dependent fields, we have

$$\epsilon = N^2 \quad (2.34)$$

where  $N$  is the refractive index. Substituting Eqn. 2.34 into Eqn. 2.33,

$$\sum_i N_i \alpha_i = 3 \frac{N^2 - 1}{N^2 + 2} \quad (2.35)$$

which is known as the Lorentz-Lorentz formula.

If the dielectric material possesses only electronic polarizability, it is non-polar and the dielectric constant will not change with frequency because electrons in atoms readily respond to optical frequencies. At X-ray frequencies, however, the dielectric constant is eventually unity and there is no agreement between the static and the X-ray dielectric constants. Materials that possess permanent molecular dipole moments have very different low- and high- frequency behavior, so that Eqn. 2.33 and Eqn. 2.35 can not be expected to give the same polarizabilities.

The frequency dependence of dielectric constant is related to the different mechanisms of polarization. There are four types of polarizations: electronic polarization, ionic polarization, dipolar polarization, and interfacial polarization. Electronic polarization is due to the separation of the centers of gravity of the electronic and nuclear charges in the applied electric field. This occurs up to very high frequency ( $10^{16}$  Hz). The application of an electric field to a polar substance causes a relative displacement of the ions leading to a lattice polarization described by an ionic polarization. Ions are heavy particles and more sluggish in their motion than electrons. As the frequency of applied electric field increases, there comes a time when the field changes so rapidly that the ions

can no longer follow its variation. Then there is no contribution to the total polarization from the ionic polarization. Therefore, ionic polarization only occurs in a relatively low frequency range  $10^{10} - 10^{13}$  Hz. Dipole polarization is caused by the perturbation of the thermal motion of ionic or molecular dipoles, introducing a dipolar orientation in the direction of applied field. Interfacial polarization involves mobile charges in the dielectrics.

For simple elemental materials or binary compounds, Duffy has established an empirical relationship between energy band gap  $E_g$  and the dielectric constant  $\epsilon$ : [27]

$$E_g = 20 \left[ \frac{3}{\epsilon + 2} \right]^2 \quad (2.36)$$

This equation indicates that a material having large dielectric constant tends to have smaller band gap. An oxide of a single metal, such as  $Ta_2O_5$  or  $ZrO_2$ , usually has a relatively high dielectric constant. In general, with increasing the atomic number of the metal, the atomic (or ionic) radius increases and so the cohesive force decreases, leading to a higher dielectric constant but a narrower band gap [28]. Table 2-3 summarized the dielectric constants of various semiconductors and insulators. The comparison of the data in Table 2-3 and the calculated data from Eqn. 2.36 was shown in Fig. 2.15.

**Table 2-3 The energy band gaps and dielectric constants of various dielectric materials.**

	$\epsilon$ ( low frequency)	$E_g$ (eV)
Diamond (C)	5.7	5.4
Si	11.9	1.17
Ge	16	0.7
$\alpha$ -Sn	23.8	$\sim 0$
SiO <sub>2</sub>	3.9	1.12
Si <sub>3</sub> N <sub>4</sub>	7.5	5
Ta <sub>2</sub> O <sub>5</sub>	15 -25	4.2
HfO <sub>2</sub>	16	5.68
Al <sub>2</sub> O <sub>3</sub>	8 - 12	-
TiO <sub>2</sub>	20 – 170	3.0-3.2
ZrO <sub>2</sub>	20	5.16-7.8

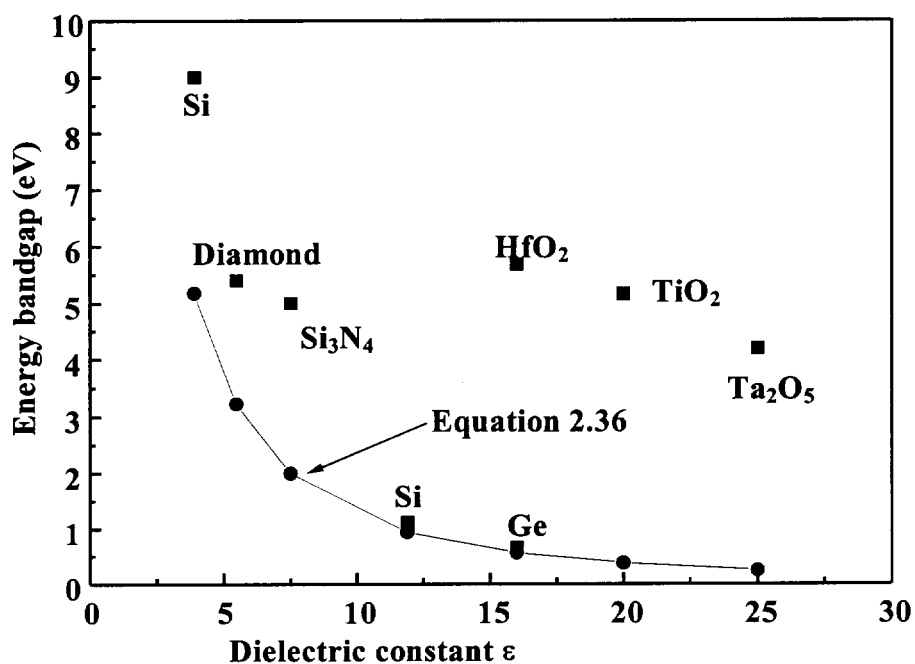


**Fig.2.15 Energy bandgap vs. the dielectric constant of various semiconductor and dielectric materials.**



Duffy's equation can not describe dielectric thin films accurately as seen from Fig. 2.15. However, it does show the trend that energy bandgap decreases with the increase of dielectric constant.

As the device size keeps shrinking, there is a great need to replace the gate oxide with some high dielectric constant material. However, the leakage current through high dielectric materials is a serious concern when these materials are to be integrated into low power IC fabrication.

Among these high dielectric metal oxides,  $\text{Ta}_2\text{O}_5$ ,  $\text{HfO}_2$ ,  $\text{Al}_2\text{O}_3$ , and  $\text{ZrO}_2$  have relatively large band gaps. Especially  $\text{Ta}_2\text{O}_5$  has been extensively studied for high-density DRAM applications. Recently  $\text{Ta}_2\text{O}_5$  has also been investigated as one of the promising candidates to replace  $\text{SiO}_2$  as the gate dielectrics in MOSFETs. To relieve the high leakage current in  $\text{Ta}_2\text{O}_5$  especially polycrystalline  $\text{Ta}_2\text{O}_5$ , stacked structure of  $\text{Ta}_2\text{O}_5$  with other insulators, such as  $\text{SiO}_2$  [29,30],  $\text{Al}_2\text{O}_3$  [31], are fabricated. The unique thin film deposition technique called atomic layer epitaxy allows growing of layered structures with nanometer range constituent layer. Using this method,  $\text{Ta}_2\text{O}_5$ - $\text{HfO}_2$  nanolaminates have been studied to improve the leakage characteristics of  $\text{Ta}_2\text{O}_5$  [32,33]. There are other nanolaminates such as  $\text{Ta}_2\text{O}_5$ - $\text{ZrO}_2$  and  $\text{HfO}_2$ - $\text{ZrO}_2$  that show improved leakage current characteristics while retaining high dielectric constant. In this thesis, the details of different nanolaminates for gate dielectrics have been investigated and will be presented in chapters 4 and 5.

## References

- [1] E. H. Nicollian and J. R. Brews, MOS Physics and Technology, John Wiley & Sons, 1982, p. 208.
- [2] R. F. Pierret, Field Effect Devices, Addison-Wesley, 1990, p. 30.
- [3] S. M. Sze, Physics of Semiconductor Devices, John Wiley & Sons, 1981, p. 367.
- [4] C. G. B. Garrett and W. H. Brattain, "Physical theory of semiconductor surfaces," Phys. Rev. **99**, 1955, pp. 376-382.
- [5] A. S. Grove, B. E. Deal, E. H. Snow, and C. T. Sah, "Investigation of thermally oxidized silicon surface using metal-oxide-semiconductor structures," Solid State Electronics **8**, 1965, pp. 145-153.
- [6] A. Goetzberger and E. H. Nicollian, "Temperature dependence of inversion layer frequency response in silicon," Bell Syst. Tech. J. **46**, 1967, pp. 513-518.
- [7] A. Goetzberger, "Ideal MOS curves for silicon," Bell Syst. Tech. J. **45**, 1966, pp. 1097-1103.
- [8] B. E. Deal, "Standardized terminology for oxide charges associated with thermally oxidized silicon," IEEE Trans. Electron Devices **27**, 1980, pp. 606-612.
- [9] L. M. Terman, "An investigation of surface states at silicon/silicon dioxide interface employing metal-oxide-silicon diodes," Solid State Electronics **5**, 1962, pp. 285-290.
- [10] C. N. Berglund, "Surface states at steam-grown silicon-silicon dioxide interface," IEEE Trans. Electron Devices **13**, 1966, pp. 701-705.
- [11] R. Castagne, P. Hesto, and A. Vapaille, "Very low frequency response of inversion layer in MIS structure," Surface Science **268**, 1969, pp. 1578-1581.
- [12] E. H. Nicollian and A. Goetzberger, "The Si-SiO<sub>2</sub> interface electrical properties as determined by the MIS conductance technique," Bell Syst. Tech. J. **46**, 1967, pp. 1055-1061.
- [13] J. S. Brugler and P. G. A. Jespers, "Charge Pumping in MOS Devices," IEEE Trans. Electron Devices **16**, 1969, pp. 297-302.

- [14] F. Hofmann and W. H. Krautschneider, "A simple technique for determining the interface-trap distribution of submicron metal-oxide-semiconductor transistors by the charge pump method," *J. Appl. Phys.* **65**, 1989, pp. 1358-1360.
- [15] M. Ohring, *Reliability and Failure of Electronic Materials and Devices*, Academic Press, 1998, p. 305.
- [16] S. M. Sze, *Physics of Semiconductor Physics*, John Wiley & Sons, 1981, p. 254.
- [17] S. M. Sze, *Physics of Semiconductor Physics*, John Wiley & Sons, 1981, p. 403.
- [18] A. Balasinski, C. Petti, H. Bamnolker, K. Kamkumar, and A. Chung, "Characterization of plasma induced damage using transient current measurements," 3rd International Symposium on Plasma Process-Induced Damage, June 4-5, 1998, Honolulu, HI, pp. 26-29.
- [19] P. E. Nicollian, M. Rodder, D. T. Grider, P. Chen, R. M. Wallace, and S. V. Hattangady, "Low leakage stress-induced-leakage-current in ultrathin gate oxides," 37th Annual International Reliability Physics Symposium, San Diego, CA, 1999, pp. 400-404.
- [20] R. H. Dennard, F. H. Gaensslen, H. -N. Yu, V. L. Rideout, E. Bassous, and A. R. LeBlanc, "Design of ion-implanted MOSFET's with very small physical dimensions," *IEEE J. Solid State Circuits* **9**, 1974, pp. 256-268.
- [21] G. Baccarani, M. R. Wordeman, and R. H. Dennard, "Generalized scaling theory and its application to  $\frac{1}{4}$  micrometer MOSFET design," *IEEE Trans. Electron Devices* **31**, 1984, pp. 452-462.
- [22] J. T. Tzou, C. C. Yao, R. Cheung, and H. Han, "The temperature dependence of threshold voltages in submicrometer CMOS," *IEEE Electron Device Letters* **6**, 1985, pp. 250-252.
- [23] J. R. Pfister, J. D. Shott, and J. D. Meindl, "Performance limits of CMOS ULSI," *IEEE Trans. Electron Devices* **32**, 1985, pp. 333-343.
- [24] B. Hoefflinger and G. Zimmer, "New CMOS technologies," *Solid State Devices* **57**, 1980, pp. 85-139.
- [25] S. M. Sze, *VLSI Technology*, John Wiley & Sons, 1988, p. 234.
- [26] H. P. Myers, *Introductory Solid State Physics*, Taylor & Francis, 1997, p. 391.

- [27] J. A. Duffy, *Bonding Energy Levels and Bands in Inorganic Solids*, John Wiley & Sons, 1990, p. 108.
- [28] K. W. Boer, *Survey of Semiconductor Physics*, Van Nostrand Reinhold, 1990, p. 26.
- [29] Y. Momiuama, H. Minakata, and T. Sugii, "Ultrathin Ta<sub>2</sub>O<sub>5</sub>/SiO<sub>2</sub> gate insulator with TiN gate technology for 0.1 $\mu$ m MOSFETs," 1997 Symp. on VLSI Technology Digest of Technical Papers, pp. 135-136.
- [30] I. C. Kizilyalli, R. Y. S. Huang, and P. K. Roy, "MOS transistor with stacked SiO<sub>2</sub>-Ta<sub>2</sub>O<sub>5</sub>-SiO<sub>2</sub> gate dielectrics for giga-scale integration of CMOS technologies," *IEEE Electron Device Letters* **19**, 1998, pp. 423-425.
- [31] R. J. Cava, W. F. Peck, Jr. J. J. Krajewski, G. L. Roberts, B. P. Barber, H. M. O'Bryan, and P. L. Gammel, "Improvement of the dielectric properties of Ta<sub>2</sub>O<sub>5</sub> through substitution with Al<sub>2</sub>O<sub>3</sub>," *Appl. Phys. Lett.* **70**, 1997, pp. 1396-1398.
- [32] K. Kukli, J. Ihakko, M. Ritala, and M. Leskela, "Tailoring the dielectric properties of HfO<sub>2</sub>-Ta<sub>2</sub>O<sub>5</sub> nanolaminates," *Appl. Phys. Lett.* **68**, 1996, pp. 3737-3739.
- [33] K. Kukli, J. Ihakko, M. Ritala, and M. Leskela, "Properties of Ta<sub>2</sub>O<sub>5</sub>-based dielectric nanolaminates deposited by atomic layer epitaxy," *J. Electrochem. Soc.* **144**, 1997, pp. 300-306.

## **Chapter 3**

### **Atomic Layer Epitaxy**

This chapter is a review of the fundamentals of Atomic Layer Epitaxy (ALE), its development history, the operation mechanism and the application of this technique. The actual application ALE on high dielectric constant thin film deposition will be addressed in details in next chapter.

#### **3.1 Background of ALE**

Atomic layer epitaxy (ALE) is a method for producing thin films and layers of crystalline or amorphous films one atomic layer at a time utilizing a self-controlled surface reaction. It was originally developed to meet the needs of ZnS thin films and dielectric thin films for electroluminescent (EL) thin film display devices [1-3]. The ALE technique was first established by Suntola and Anston based on a modified vacuum evaporator in 1974. Although the name “atomic layer epitaxy” was originally given by Suntola, it is now a generic term for this method of film deposition and the deposited film can be either crystalline or amorphous. The first US patent on ALE was submitted by the Lohja Corporation from Finland in 1975 and granted in 1977 [1]. Since then ALE has been used mostly to grow thin films in display industry. Current commercial grade ALE reactors manufactured by ASM Microchemistry can handle 8-inch wafers. The ALE technique has also been extended for semiconductor and IC fabrication. The high

permittivity insulators, such as metal oxides processed by ALE have recently attracted more interest from the semiconductor industry [4-5].

### 3.2 The mechanism of ALE process

The basic idea of ALE is the sequential surface reactions resulting in a saturating monolayer growth during each step. In a typical ALE process, the substrate is exposed to alternate vapor sources. The substrate surface is initially saturated with the first reactant in vapor phase. This step is followed by a purging cycle by an inert gas such as  $N_2$  to remove the excess reactants. Due to the energy difference between chemical adsorption and physical adsorption, only one atomic layer will be left adhering to reaction surface. Then the substrate is subject to the second component vapor for a binary compound. After the reaction of the first and the second reactants, an atomic layer of desired binary compound is deposited on the substrate surface after one cycle. The gas phase by-products and excess vapors of reactants are carried out of the reactor by the purge gas pulse. By repeating the reaction cycles, thin films can be deposited monolayer-by-monolayer.

The successful growth via ALE is based on the energy difference between chemical adsorption and physical absorption of reactants on the surface of a substrate. Chemical adsorption describes the chemical bonding between two atoms, while physical adsorption is due to the van der Waal's forces between charges. When a flux of reactant reaches the substrate surface, the first layer interacts with the substrate and is chemically adsorbed onto the substrate, forming chemical bond at an appropriate temperature. This is called chemical adsorption. The subsequent layers are bonded much more weakly and the bonds are very easy to break, hence called physical adsorption. The energy diagram of these two kinds of adsorption mechanism is illustrated in Fig. 3.1, where  $E_c$  and  $E_p$  are the activation energies of chemical adsorption and physical adsorption, respectively [6].

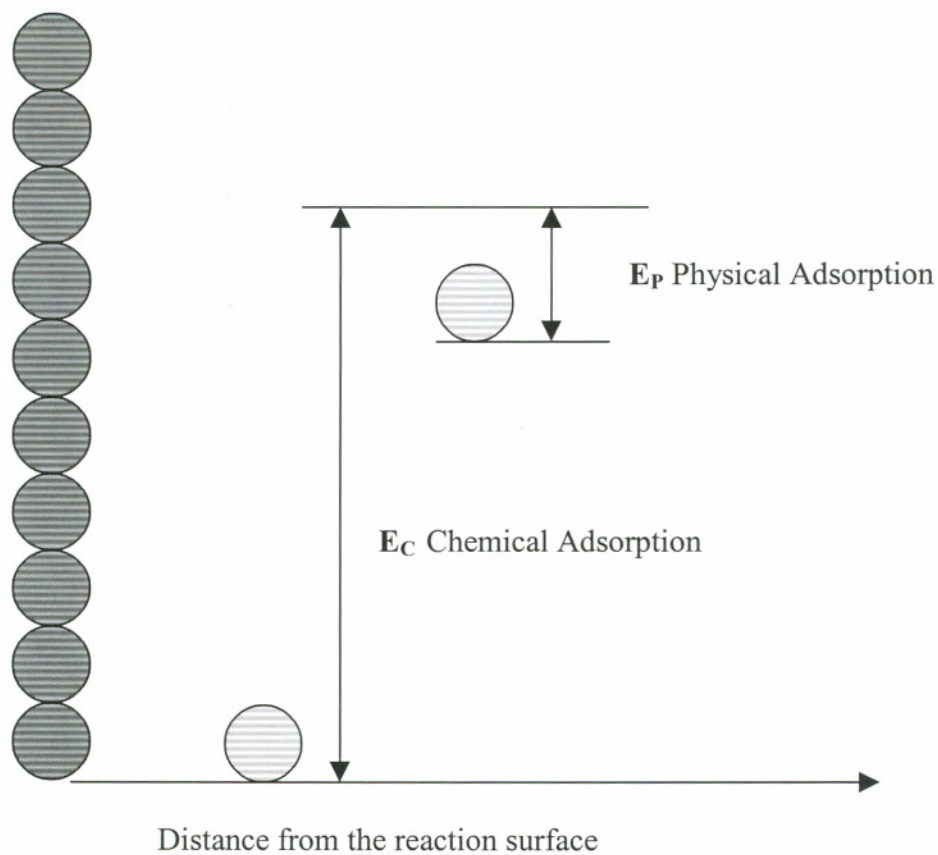


**Fig. 3.1 Energy diagram of chemical and physical adsorption**

When selecting the source materials for an ALE process, a discrimination factor  $\eta$  is defined as:

$$\eta = \exp\left(\frac{E_C}{E_P}\right) \quad (3.1)$$

It is desirable to find the source materials with large discrimination factors when they are introduced to the substrate. This allows us to have larger ALE process

temperature windows. Generally the substrate temperature should satisfy  $E_p < kT \ll E_c$ , where  $k$  is the Boltzmann constant and  $kT$  is the thermal energy of the substrate. The appropriate temperature range for a successful ALE growth, the so-called ALE temperature window has been studied by Suntola [7]. In this temperature range the film growth will produce one monolayer per cycle and the growth rate remains constant regardless of the temperature changes within the allowed range, as illustrated in Fig. 3.2.

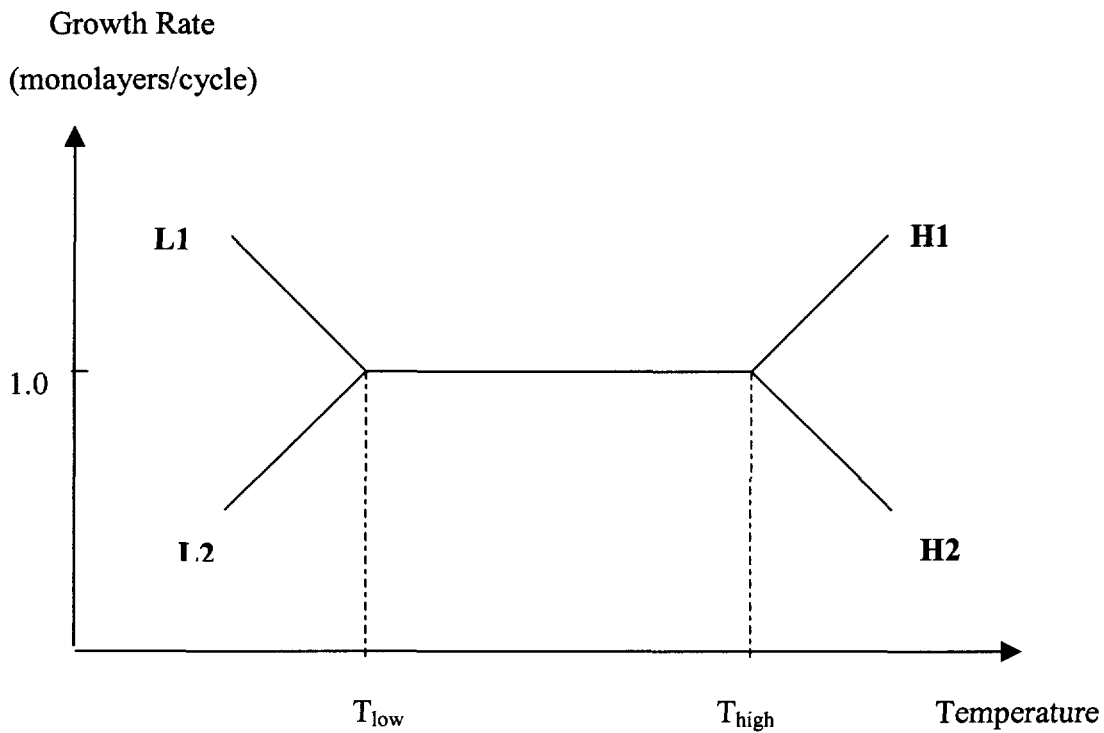


**Fig. 3.2 An ALE processing temperature window.**

The temperature dependence of the growth rate in monolayer units per cycle gives a first indication of the limiting mechanisms of ALE process. When the operation temperature is between  $T_{low}$  and  $T_{high}$ , monolayer ALE growth occurs.



At the operating temperature below the lower limit of the window temperature, the following problems will take place:

(L1) Condensation of reactants and their by-products generally with elemental sources. This may cause higher growth rate but this rate will vary with temperature. Therefore, this is an uncontrollable process.

(L2) Incomplete surface reactions mostly with molecular sources. In this case, there is activation energy to be exceeded. Extra energy will be needed to form the chemical adsorption.

At operating temperature above the higher limit of the window temperature, other problems can occur:

(H1) The undesirable decomposition of molecular reactants will result in fast film growth. This is typical when large molecular metal organic compounds are used as precursors.

(H2) Re-evaporation of a formed monolayers.

The temperature limits depend on the time and flux density of the reactants used for each sequence. In a typical ALE process, there are several process parameters that need to be optimized to achieve an ideal monolayer growth. First of all, the substrate temperature is obviously critical as seen from the ALE temperature window. Meanwhile, the substrate has to be saturated with the source material in vapor phase, which means the flux of source vapor must be able to cover the entire substrate. Therefore, reactor pressure and the source material temperature must be carefully adjusted. Furthermore, the vapor source should have high mobility across the substrate to achieve uniform growth. This is a matter of choosing source material and defines the flow rate of inert purge gas, as well as setting pulse time for each sequence. Reactor cleaning is also critical to prevent cross contamination from run to run.

There is some literature reporting surface chemistry of ALE growth of metal oxides on porous silica. The surface coverage of metal species achievable at a certain temperature on an oxide is determined by the number of specific reactive sites for the

precursors [8]. Silica surfaces are terminated by isolated H-bonded OH groups and siloxanes (oxygen bridges), which serve as bonding sites. The heat treatment of silica controls the number of OH groups on the surface, which in turn determines the surface density of a precursor bonding to the OH groups. Although these studies only concentrated on silica, they can be applied on other oxides since all oxide surfaces are more or less terminated with OH groups and oxygen bridges. However, each precursor/oxide pair would need a separate study.

Atomic layer epitaxy is primarily used in epitaxial growth of III-V and II-VI compounds, especially layered structures, such as superlattices and superalloys. It has great advantage in thin film deposition from multiple source materials at relatively low temperatures. Since ALE is a fairly new technique, the growth technique is still not well understood. However, this does not influence the application of ALE on high quality thin film deposition. Most thin film deposition techniques involve material transfer from a solid source via vapor phase in high vacuum systems or at high temperature, such as evaporation, sputtering, or chemical vapor deposition (CVD). Compared to these technologies, ALE produces epitaxial layers at relatively lower temperatures and does not require ultra-high vacuum reactors. It is a self-controlled process, which results in an accuracy of a single atomic layer because of saturated surface reactions. ALE has been proved to be suitable for growing uniform layers over large areas, even on non-planar surfaces. Using this method, it is possible to investigate the chemical reactions associated with thin film growth in more details compared to other technologies. In current ultra thin film (in nanometer scale) processing, ALE excels over other traditional approaches due to its precise control of the thickness and composition of thin films across a large area. Therefore, ALE is finding more applications in modern high-tech industries.

## References

- [1] T. Suntola and M. J. Anston, "Method for producing compound thin films," U. S. Patent No. 4,058,430 (1977).
- [2] T. Suntola, A. Pakkala, and S. Lindfors, "Method for performing growth of compound thin films," U. S. Patent No. 4,413,022 (1983).
- [3] T. Suntola, "Performance of atomic layer epitaxy devices," Digest of Technical Papers on SID International Symposium (Society for Information Display), New York, NY, 1981, pp. 20-21.
- [4] L. Niinisto, M. Ritala, and M. Leskela, "Synthesis of oxide thin films and overlayers by atomic layer epitaxy for advanced applications," *Materials Science and Engineering B* **41**, 1996, pp. 23-29.
- [5] H. Kattelus, M. Yliammi, J. Saarilahti, J. Antson, and S. Lindfors, "Layered tantalum-aluminum oxide films deposited by atomic layer epitaxy," *Thin Solid Films* **225**, 1993, pp. 296-298.
- [6] T. Suntola, "Atomic layer epitaxy," *Acta Polytechnica Scandinavica, Electrical Engineering Series* **64**, 1989, pp. 242-270.
- [7] T. Suntola, "Atomic layer epitaxy," *Materials Science Report* **4**, 1989, pp. 261-312.
- [8] S. Haukka, E-L Lakomaa, and T. Suntola, "Surface coverage of ALE precursors on oxides," *Applied Surface Science* **82/83**, 1994, pp. 548-552.

## **Chapter 4**

### **ALE growth of Ta<sub>2</sub>O<sub>5</sub>, HfO<sub>2</sub>, ZrO<sub>2</sub> and their nanolaminates**

In this chapter, the growth of high dielectric constant thin films Ta<sub>2</sub>O<sub>5</sub>, HfO<sub>2</sub> and ZrO<sub>2</sub> by atomic layer deposition will be described. The process conditions for growing these films on bare silicon substrate and silicon nitride passivated silicon substrates are presented. X-ray diffraction and transmission electron microscope (TEM) were employed to characterize material properties.

#### **4.1 Introduction of the F-120 ALE reactor**

ALE F-120 reactor was manufactured by the Finnish company Microchemistry Ltd. It was designed for research purposes, for high flexibility and for easy operation. The design of the gas flow dynamics in F-120 has been made in parallel with that in production size reactors. Therefore processes developed with F-120 reactor are scalable to industrial scale in a straightforward way.

The schematic diagram of the F-120 is shown in Fig. 4.1[1]. There are six precursor sources available, four of which (#1, #2, #4, #5) are for solid source materials (mostly powders or pre-melted powders), the other two (#3 and #6) are for gases (such as H<sub>2</sub>S and H<sub>2</sub>) and liquid (such as H<sub>2</sub>O) sources. Each port is sealed with an O-ring and has a thermocouple probe. Solid source materials are usually held in glass boats that are attached to the thermocouples for temperature control. The solid source temperatures

need to be high enough for the precursor to be vaporized and low enough to prevent the precursor from being depleted before a deposition run finishes. The tubing and valving system of the F-120 reactor are fairly complicated as shown in Fig. 4.1. There is one inner tube and one outer tube for each source port. When the vapor is not needed in the reaction chamber, valve A is closed and only  $N_2$  can flow in the outer tube. The vapor is split at the substrate end, going to the substrate and along the BDE to carry the undesired vapor (excess source precursor and by-products) to the exhaust tube. On the other hand, when the vapor is needed, valve A opens, and  $N_2$  will be divided to flow in both inner and outer tubes but mostly through the inner tube. Source vapor flows in direction DBC to the substrate holder.

Heating coils control the temperatures of eight temperature zones, and temperature increases in the direction toward the substrate holder. The advantage of this temperature distribution is that gases flowing toward the substrate travel through regions of increasing temperatures, reducing or eliminating the possibility of condensation on the tube wall. The temperature setting of each temperature zone will be affected by its neighboring heaters because the thermal insulation of adjacent temperature zones is not perfect. It is necessary to set small temperature increments for adjacent heaters when we set up a run. However, this weakness limits our choices of precursors.

The schematic side view of the substrate holder (also called "satellite") in the F-120 is shown in Fig. 4.2. Fig. 4.3 shows the rear view. Two 50 mm x 50 mm substrates are held back-to-back and sit vertically in the substrate holder. A glass spacer could be used between the two substrates depending on the actual width of the trench on the glass substrate boat used to hold the substrates in the "satellite".

The ALE process is controlled by a Compaq 386-PC computer that allows the user to program the source temperatures, growth temperature, gas flow rate and pulsing sequence. Programming can conveniently control multiple layer growth and doping levels.

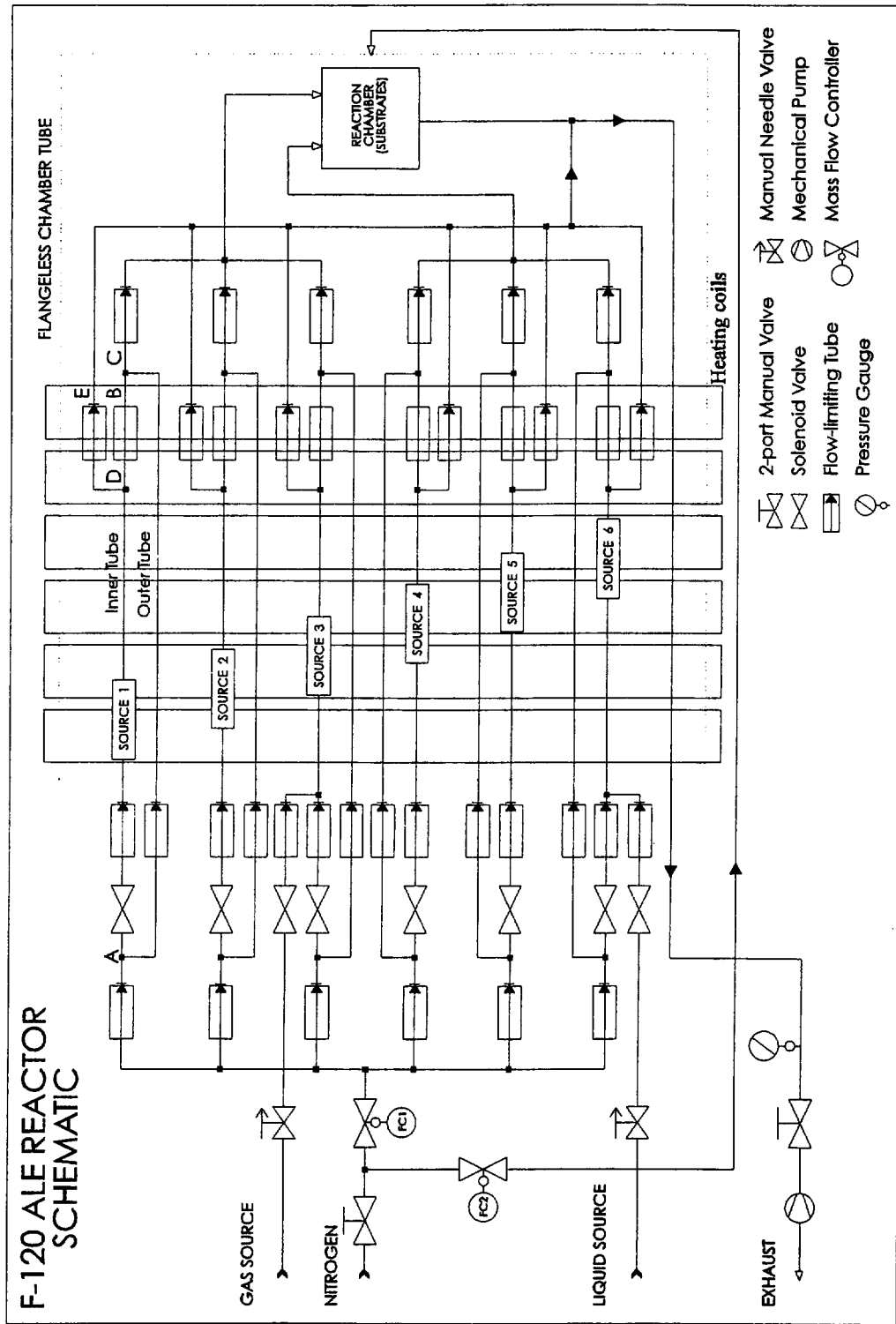


Fig. 4.1 ALE F-120 reactor system schematic.  
[1]

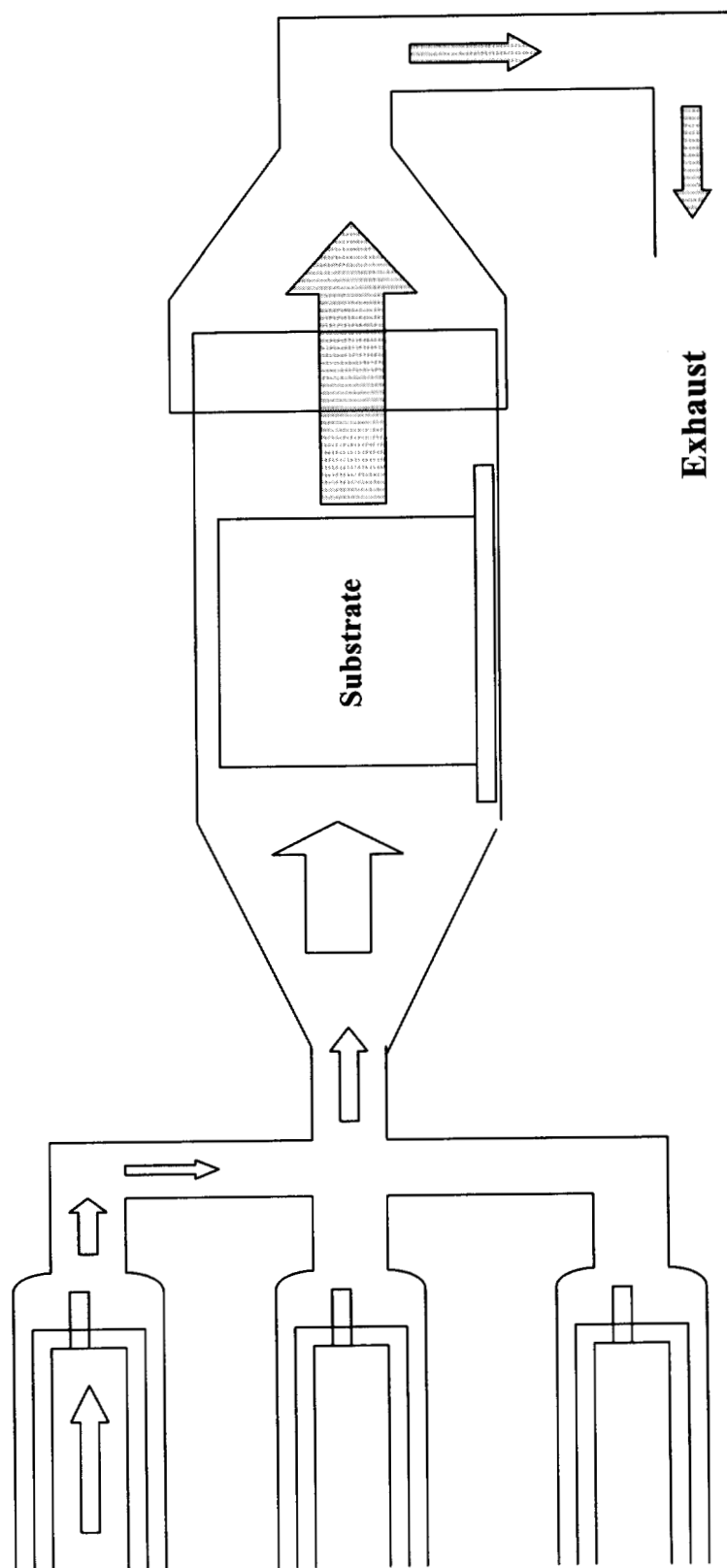
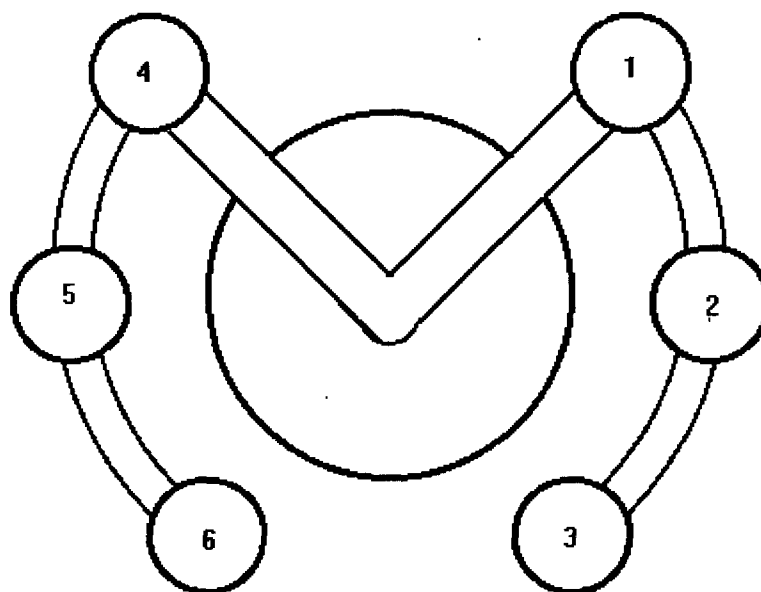


Fig. 4.2 Schematic diagram of the F-120 substrate holder (side view)



**Fig. 4.3 The rear view of F-120 substrate holder. There are six precursor ports.**

## **4.2 Growth and Initial Characterization of $\text{Ta}_2\text{O}_5$**

Tantalum oxide ( $\text{Ta}_2\text{O}_5$ ) thin film has attracted much interest due to its promising application as a storage capacitor material for gigabit dynamic random access memories (DRAM) [2-5].  $\text{Ta}_2\text{O}_5$  has many outstanding characteristics, including high dielectric constant and high capacitor density [6]. Having a dielectric constant of around 25,  $\text{Ta}_2\text{O}_5$  has also been proposed as MOSFET gate insulator for high-speed circuits [7].  $\text{Ta}_2\text{O}_5$  thin films grown by ALE at  $300^\circ\text{C}$  are usually amorphous and turn to polycrystalline after rapid thermal annealing at temperatures above  $800^\circ\text{C}$ . When growing via ALE, tantalum chloride ( $\text{TaCl}_5$ ) and water ( $\text{H}_2\text{O}$ ) vapor have been used as source materials.  $\text{TaCl}_5$  is the metallic precursor while  $\text{H}_2\text{O}$  is used as the oxidant source. The  $\text{TaCl}_5$  used is in form of



very fine powder and has fairly high vapor pressure when heated up to around 100°C. H<sub>2</sub>O source was kept at room temperature. In the growth cycle of Ta<sub>2</sub>O<sub>5</sub>, TaCl<sub>5</sub> and H<sub>2</sub>O vapor were pulsed alternatively as shown in Fig. 4.4. Nitrogen (N<sub>2</sub>) is used as the carrier gas for both precursors. A 2 s N<sub>2</sub> purging gas is inserted between TaCl<sub>5</sub> and H<sub>2</sub>O pulses. The effect of N<sub>2</sub> purge is to transport source material to substrates and clean the reaction surface so that excess gas molecules and by-products are carried away. The overall chemistry on the substrate surface will lead to formation of Ta<sub>2</sub>O<sub>5</sub> and HCl. The HCl is volatile and will be pumped out while Ta<sub>2</sub>O<sub>5</sub> will stay on the substrate. When Ta<sub>2</sub>O<sub>5</sub> is grown on Si substrates, the substrates are pre-cleaned and dipped into HF prior to loading into the ALE reactor. The oxide thickness and their refractive indices were initially determined with a Gaertner ellipsometer (at wavelength of 632.8 nm) and then more detailed analysis was done using a spectroscopic ellipsometer (SOPRA ES4G). The crystalline properties were determined using a grazing incidence X-ray diffractometer (XRD) and cross-sectional transmission electron microscopy (TEM).

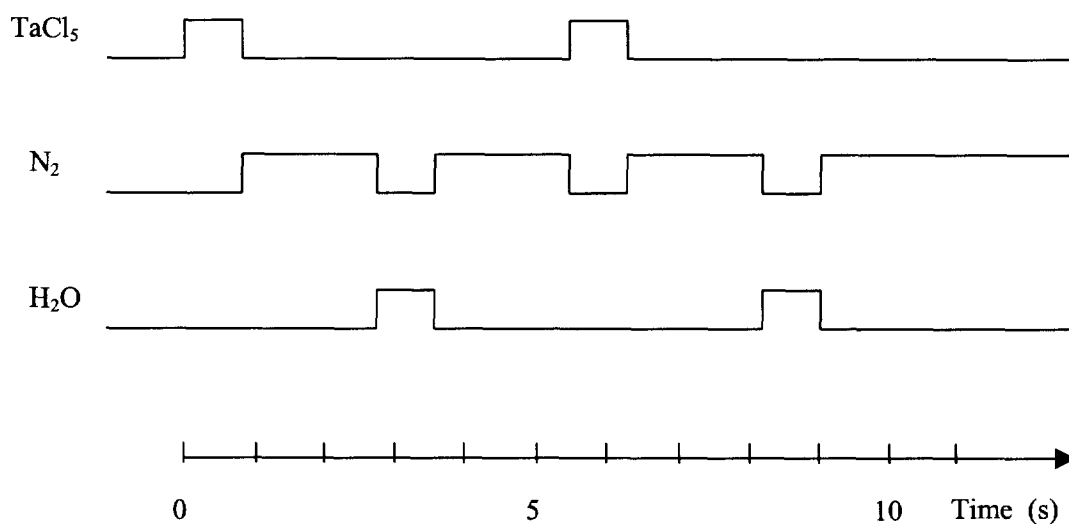


**Fig. 4.4 Gas pulse sequence in Ta<sub>2</sub>O<sub>5</sub> growth by ALE process**

During growth of  $\text{Ta}_2\text{O}_5$ , a very thin layer of  $\text{SiO}_2$  is formed on top of Si as shown in Fig.4.5. This is due to the oxidation of silicon by the  $\text{H}_2\text{O}$  pulse at the growth temperature. This thin layer of  $\text{SiO}_2$  dramatically reduced the total capacitance of the  $\text{SiO}_2$ - $\text{Ta}_2\text{O}_5$  stack due to the low dielectric constant of  $\text{SiO}_2$ . Some  $\text{Ta}_2\text{O}_5$  depositions were performed on Indium-Titanium-Oxide (ITO) substrate, and the capacitance of this ITO-  $\text{Ta}_2\text{O}_5$  stack was much higher than that of  $\text{Ta}_2\text{O}_5$ - $\text{SiO}_2$  stack. To prevent Si surface from oxidizing, a layer of  $\text{Si}_3\text{N}_4$  of thickness 2.76 nm was formed on Si substrate by rapid thermal process in  $\text{NH}_3$  ambient at  $1000^\circ\text{C}$  for 15~30 seconds. Subsequent  $\text{Ta}_2\text{O}_5$  deposition was on  $\text{Si}_3\text{N}_4$  coated Si substrates.

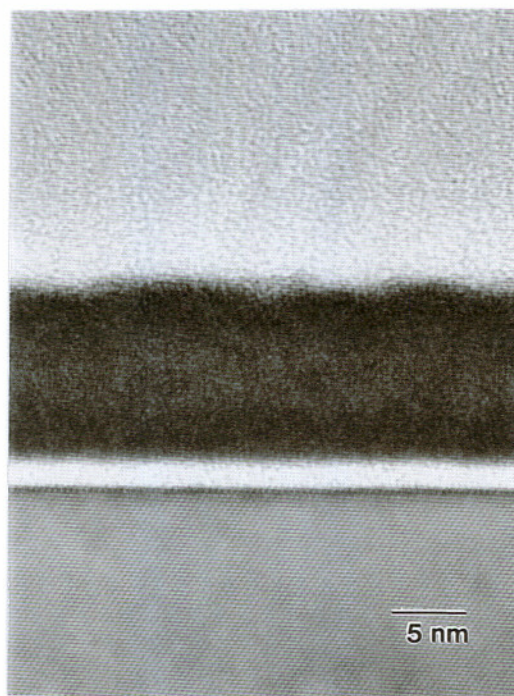


**Fig. 4.5** High resolution TEM lattice image of  $\text{Ta}_2\text{O}_5$  film with an ellipsometrically measured thickness of 11.6 nm grown on silicon substrate. A layer of 1.5 nm  $\text{SiO}_2$  is formed at the interface.

A wide range of growth temperatures was studied. Ta<sub>2</sub>O<sub>5</sub> thin films were deposited at reactor temperatures of 100, 200, 300, 400 and 500°C. As shown in Fig. 4.6, the growth rate decreases with an increase of film growth temperature. At temperatures of 100 and 200°C, condensation of reactants occurs on the substrates so that the growth rates were fairly high. Extreme low growth rates were observed at 400 and 500°C, which was due to re-evaporation of a formed monolayer. Therefore, the proper growth temperature window is around 300°C. Rapid thermal anneal (RTA) at 1000°C in argon ambient did not change the film thickness except for the film grown at 100°C, where Ta<sub>2</sub>O<sub>5</sub> film thickness decreased after RTA as shown in Fig. 4.7. This could be due to the densification of the film grown at 100°C. It is also necessary to optimize the amount of water in the process. With the growth temperature set at 300°C, Ta<sub>2</sub>O<sub>5</sub> was grown with water needle valve opened at 2, 4, 6 and 7.5 turns. Film thickness increased with the increase of water. The best uniformity was obtained with water opened at four turns. No obvious variation of film thickness was observed before and after RTP as shown in Fig. 4.8. Ellipsometry study revealed that the refractive index of annealed film was 2.183 at 632.8 nm, the same as the as-deposited films. XRD analysis indicated that as-deposited Ta<sub>2</sub>O<sub>5</sub> thin film to be amorphous. However, these films crystallized after annealing in a RTP chamber at 800°C in either argon or oxygen ambient as shown in Fig. 4.9 and had the hexagonal crystal structure. Argon was used to avoid oxidation of the Si substrates during anneal. There could be oxygen vacancies in the deposited films, which can cause the increase of leakage current as has been reported. O<sub>2</sub> anneal helps to reduce the oxygen vacancies if there are any. Secondary ion mass spectroscopy (SIMS) characterization showed the films to be stoichiometric, with the concentration of chlorine below the detection limit.

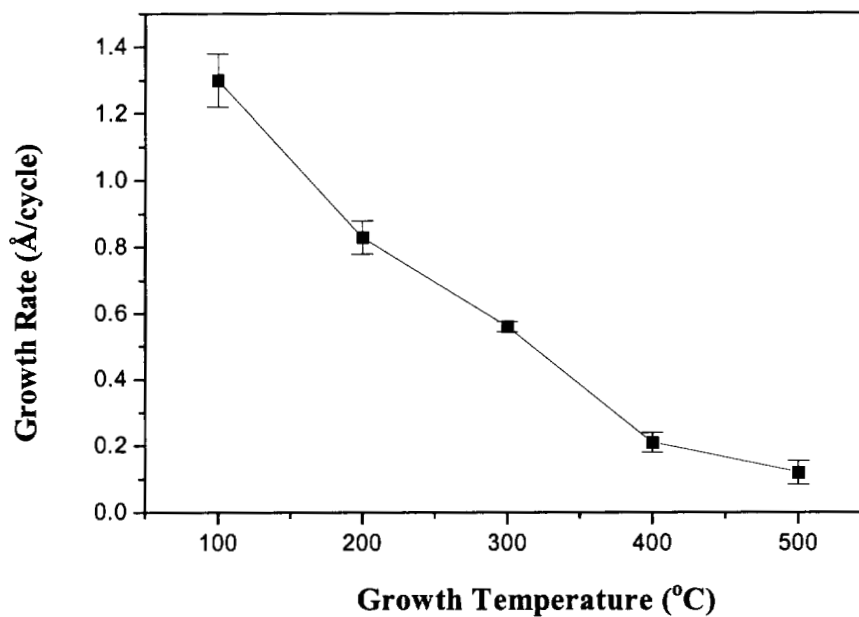


Fig.4.6 Growth rate vs. growth temperature of  $\text{Ta}_2\text{O}_5$  ALE thin films grown on Si substrate using  $\text{TaCl}_5$  and  $\text{H}_2\text{O}$ .

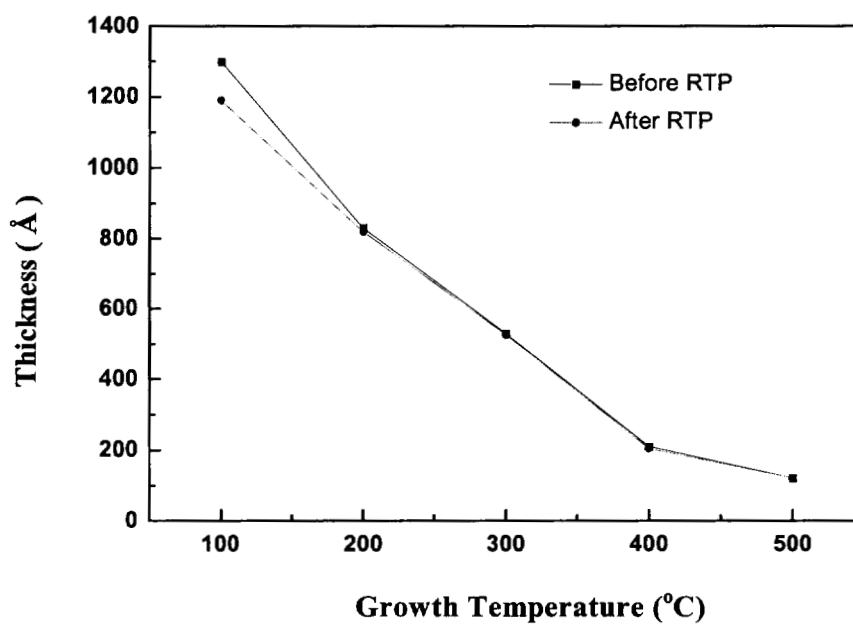


Fig. 4.7 The effect of RTP on  $\text{Ta}_2\text{O}_5$  film thickness at growth temperatures of 100, 200, 300, 400 and 500°C. The number of water turn is 4 and water is kept at 20°C.

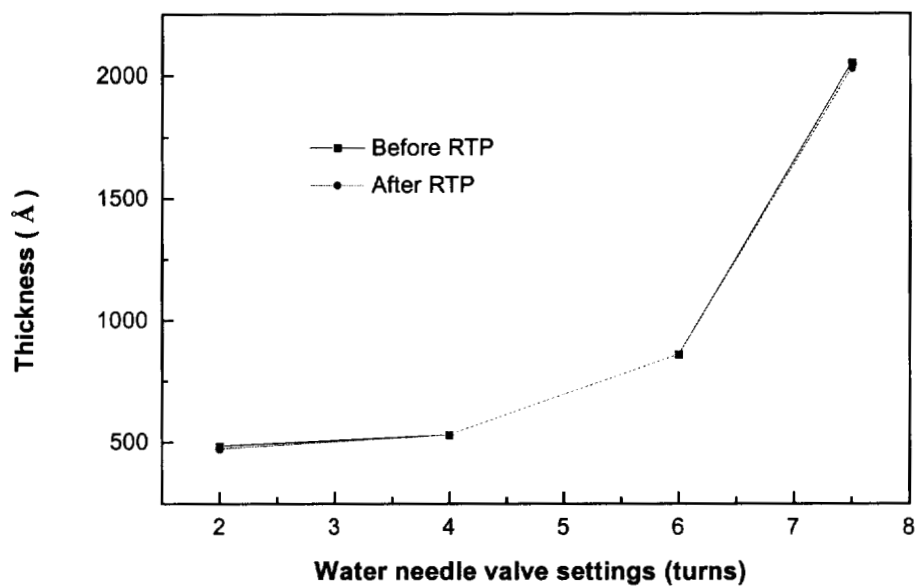


Fig. 4.8 The effect of water on Ta<sub>2</sub>O<sub>5</sub> film thickness at growth temperature of 300°C.

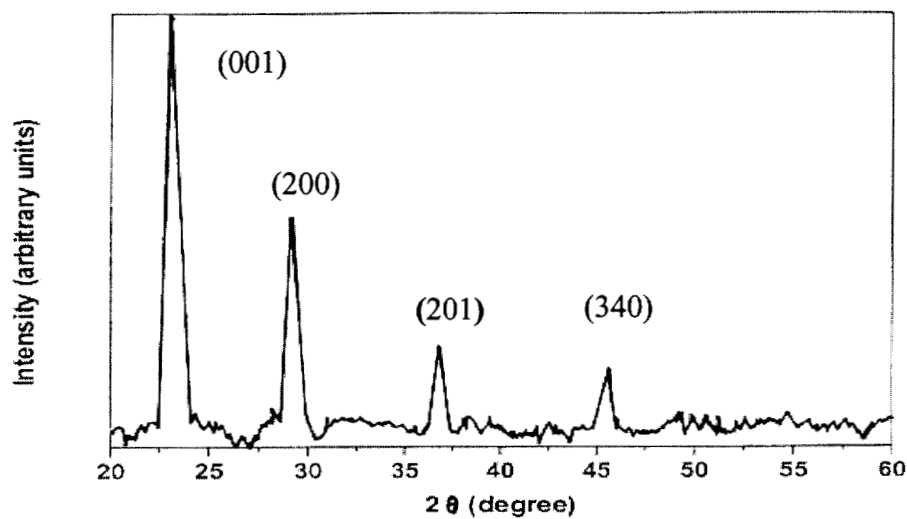


Fig. 4.9 X-ray diffraction pattern of rapid thermal annealed Ta<sub>2</sub>O<sub>5</sub> film at 800°C for 30 s in Ar.

### 4.3 Growth and initial characterization of HfO<sub>2</sub>

Hafnium oxide (HfO<sub>2</sub>) is another insulating material with a much higher permittivity than silicon dioxide (SiO<sub>2</sub>). The reported dielectric constants of bulk HfO<sub>2</sub> are 13-16 [8], which is lower than that of Ta<sub>2</sub>O<sub>5</sub>. However, the leakage current of HfO<sub>2</sub> is much lower than that of Ta<sub>2</sub>O<sub>5</sub> for films of the same thickness. Quite promising results have been reported for sputtered HfO<sub>2</sub> films used in MOS capacitors [9]. It has also been used as an effective etch-stop layer when etching SiO<sub>2</sub> overcoats [10].

The source materials for growing HfO<sub>2</sub> were HfCl<sub>4</sub> powder and water vapor. The optimized source temperature was 140°C for HfCl<sub>4</sub>, whereas H<sub>2</sub>O was again kept at 20°C. The deposition of HfO<sub>2</sub> by ALE was conducted between 250 – 500°C. The growth rate decreased from 1.9 Å/cycle at 250°C to 0.32 Å/cycle at 500°C. The growth rate of HfO<sub>2</sub> is 1.1 Å/cycle at 300°C. To keep the growth temperature same as that for Ta<sub>2</sub>O<sub>5</sub>, a film deposited at 300°C was analyzed using SIMS technique giving a result that the chlorine concentration is less than detection limit. When HfO<sub>2</sub> was grown on a Si substrate, the film uniformity was very poor. Similar to the growth of Ta<sub>2</sub>O<sub>5</sub> on bare Si substrates, an interfacial layer of SiO<sub>2</sub> was observed when growing HfO<sub>2</sub> directly on Si. However, the uniformity of HfO<sub>2</sub> film was significantly improved when HfO<sub>2</sub> was deposited on a nitrided Si substrate. This is due to the improved adhesion of HfO<sub>2</sub> to Si<sub>3</sub>N<sub>4</sub>. HfO<sub>2</sub> deposited on a Si substrate and Indium- Titanium- Oxide (ITO) coated glass by ALE at 300°C had a dielectric constant 16 for 28 nm thick film. Although there was a thin layer of SiO<sub>2</sub> appeared at the HfO<sub>2</sub>-Si interface, the reduction of capacitance due to the existence of SiO<sub>2</sub> is negligible when the thickness of HfO<sub>2</sub> is greater than 20 nm. It is obvious that capacitance of the HfO<sub>2</sub> will dominate when its thickness is large enough. The as-deposited HfO<sub>2</sub> by ALE was also amorphous. It is evident from XRD analysis that HfO<sub>2</sub> thin films crystallize after annealing in the RTA chamber at 800°C for 30 s in Ar or O<sub>2</sub> ambient, as shown in Fig. 4.10. The monoclinic structure is believed to be stable with lattice constants  $a = 5.285 \text{ \AA}$ ,  $b = 5.182 \text{ \AA}$ ,  $c = 5.116 \text{ \AA}$ , a preferred orientation in the (1, 1, 1) plane. A TEM cross-section photograph showed the oxidation of Si during the

growth of  $\text{HfO}_2$  on bare Si wafer in Fig. 4.11. This thin interfacial layer of  $\text{SiO}_2$  will reduce the effective  $k$  value of  $\text{HfO}_2/\text{SiO}_2$  stack because of the low dielectric constant of  $\text{SiO}_2$ . Therefore, a nitrided silicon substrate was used in the future  $\text{HfO}_2$  growth, as for the  $\text{Ta}_2\text{O}_5$  thin film.

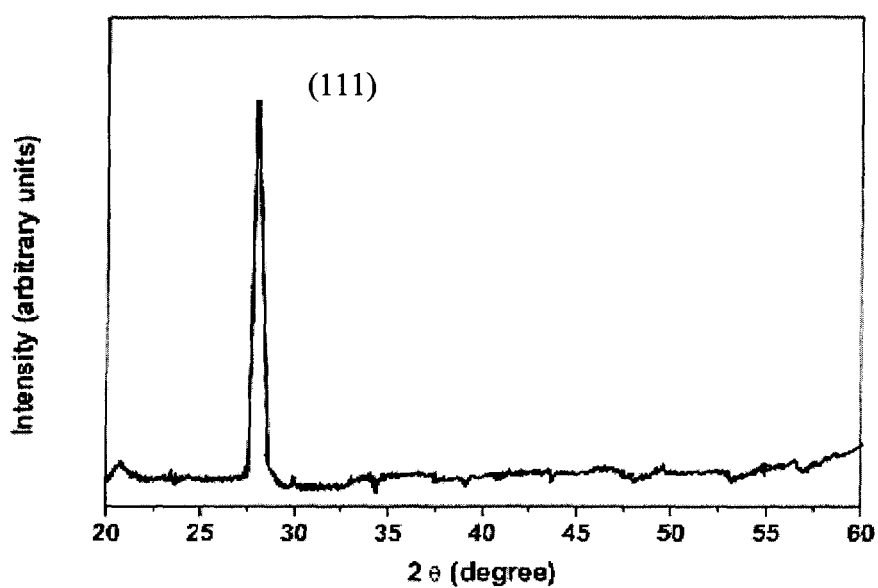


**Fig. 4.10** X-ray diffraction pattern of  $\text{HfO}_2$  annealed in RTA chamber at 800 °C for 30 s in Ar.

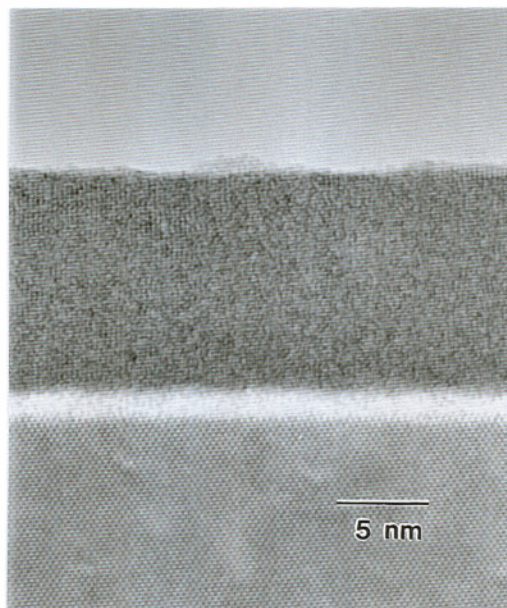


**Fig. 4.11 High resolution TEM lattice image of  $\text{HfO}_2$  film with an ellipsometry thickness of 15 nm grown on Si.  $\text{SiO}_2$  layer of 2 nm is formed at the interface.**

#### **4.4 Growth and initial characterization of $\text{ZrO}_2$**

Zirconium oxide ( $\text{ZrO}_2$ ) is characterized by extreme thermal, chemical and mechanical stability which together with its optical and electrical properties gives rise to a wide range of technical applications for its thin films and coatings, especially in optics, electronics, and as protective layers. The fairly high permittivity (20 for bulk material) and low leakage current with a wide band gap of 5.1~7.8 eV make  $\text{ZrO}_2$  an attractive material for future high capacitance MOS capacitor. Besides numerous physical vapor deposition techniques, like plasma spraying [11] and sputtering [12], chemical vapor deposition (CVD) has also been used to deposit  $\text{ZrO}_2$  thin films [13,14]. The use of  $\text{ZrCl}_4$ , the most readily available volatile zirconium precursor, is complicated due to its hygroscopic properties and the oxidation results in premature powder formation. The



characteristic feature of ALE can avoid the gas-phase reactions when exploiting  $\text{ZrCl}_4$  and  $\text{H}_2\text{O}$  as the source materials [15].

In a typical ALE process,  $\text{ZrCl}_4$  (99.5% purity; Strem) was evaporated from an open boat at  $150^\circ\text{C}$  onto the substrate. An external water reservoir held at  $20^\circ\text{C}$  was connected to the cold end of the reactor through a capillary and a needle valve. Water was introduced into the reactor by its own pressure without any bubbling systems. Total pressure of the reactor was in the order of 10 mbar.  $\text{ZrO}_2$  films were deposited at  $300^\circ\text{C}$ ,  $400^\circ\text{C}$  and  $500^\circ\text{C}$ , respectively. Lower growth rates were observed at  $400^\circ\text{C}$  and  $500^\circ\text{C}$ . In order to grow nanolaminates,  $\text{ZrO}_2$  grown at  $300^\circ\text{C}$  was studied in detail. Compared to deposition of  $\text{Ta}_2\text{O}_5$  and  $\text{HfO}_2$ , rather long pulse and purge times were needed to realize the self-controlled process for the  $\text{ZrO}_2$  growth. The growth of  $\text{ZrO}_2$  highly depended on  $\text{ZrCl}_4$  and the water pulse durations at substrate temperature of  $300^\circ\text{C}$ . Fig. 4.12 shows the dependence of film thickness on  $\text{ZrCl}_4$  pulse duration. The effect of the purge time was studied with a 2 s pulse durations as indicated in Fig. 4.13. The thicknesses shown were measured at the center of the substrates. When the  $\text{ZrCl}_4$  pulse time was longer than 1.5 s and water purge duration exceeded 2 s, saturation is reached and film conformity was independent of the above parameters. It was observed that the  $\text{ZrCl}_4$  pulse was critical with respect to the surface saturation, while short water pulse had no effect on film thickness. On the other hand, water purge time was essential to achieve good thickness uniformity. The optimized growth condition of  $\text{ZrO}_2$  produced a growth rate of 1.2 Å/cycle.

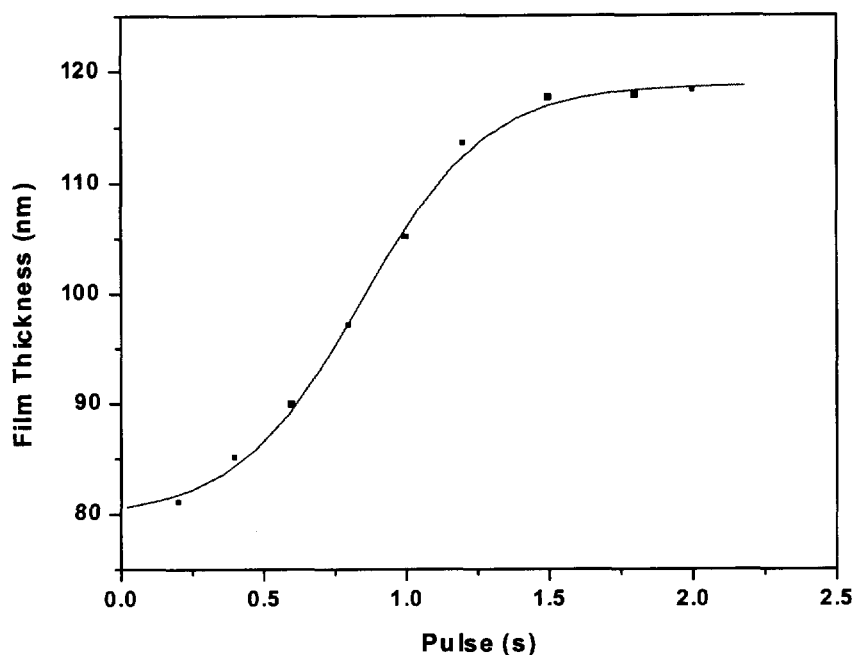


**Fig. 4.12 The dependence of film thickness on the  $\text{ZrCl}_4$  pulse duration for  $\text{ZrO}_2$  film deposited at  $300^\circ\text{C}$  for 1000 reaction cycles. The  $\text{ZrCl}_4$  purge time used was 2.0 s except for 2.0 s pulse time where 4.0 s purge duration was employed.**

The as-deposited  $\text{ZrO}_2$  was nearly amorphous and was partially crystallized after RTP at  $700^\circ\text{C}$  for 30 s, as shown in Fig. 4.14. The film showed strong (002) peak of tetragonal  $\text{ZrO}_2$  and relatively weak (111) peak of monoclinic  $\text{ZrO}_2$ . This means the polycrystalline  $\text{ZrO}_2$  film was composed of mainly tetragonal  $\text{ZrO}_2$  with a small amount of monoclinic  $\text{ZrO}_2$ . Again SIMS analysis did not detect any trace of chloride in the  $\text{ZrO}_2$  thin film. The ellipsometry measurement indicated a refractive index of 2.1 at wavelength 632.8 nm.

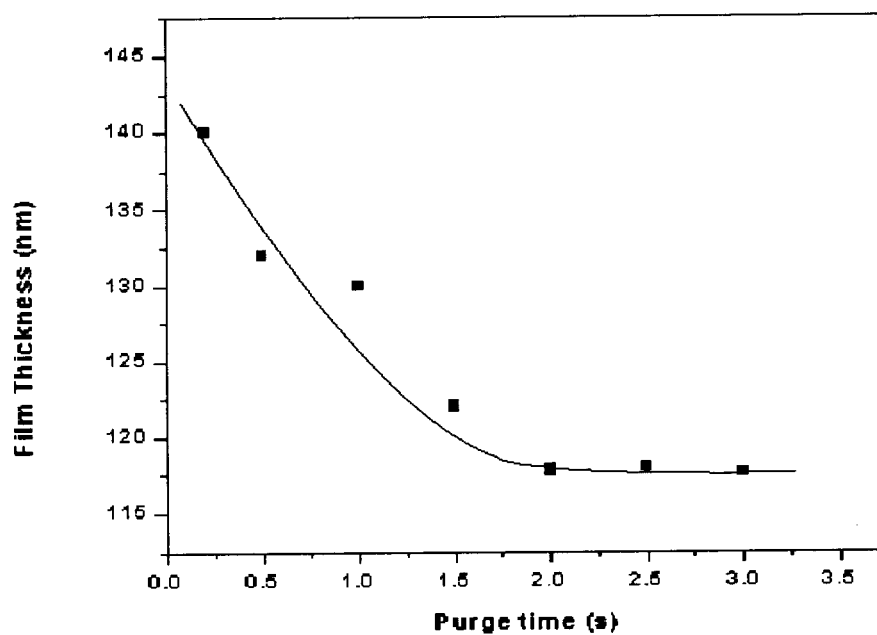


**Fig. 4.13** The film thickness as a function of the water purge durations. The data were measured at the center of the film grown by 1000 cycles at 300°C using 2.0 s  $\text{ZrCl}_4$  pulses.

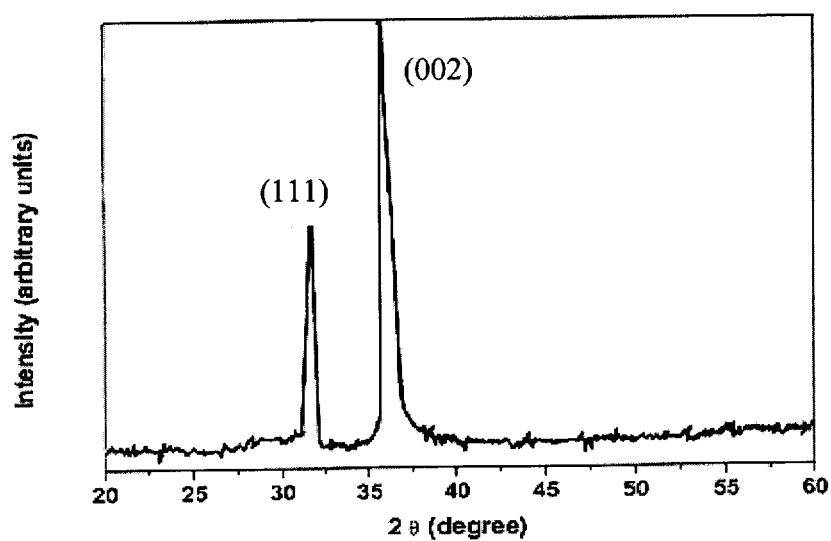


**Fig. 4.14** X-ray diffraction pattern of  $\text{ZrO}_2$  annealed at 700°C for 30 s in Ar.

## 4.5 Growth and initial characterization of nanolaminates

Nanolaminates consist of thin layers of alternating metal oxides. These oxides may be crystalline or amorphous by themselves. Since the amorphous layers interrupt the continuous growth of the polycrystalline material, the continuous grain boundaries were inherently eliminated [16]. To obtain the optimum dielectric properties, the constituent oxides should be of high permittivity and sufficiently thin.

As the layer thickness was reduced, the size of the crystallites after anneal was reduced, which in turn decreased the leakage current of the nanolaminates. An increased amount of electron trapping centers at the interlayer boundaries could also be the cause of leakage current reduction. The leakage current reduction in nanolaminates can also be due to electron trapping at the interfaces states at the end of leakage channels extending through single sublayers, thereby causing a decrease of the injecting electric field in the vicinity of these channels.

### 4.5.1 Growth of $\text{Ta}_2\text{O}_5$ – $\text{HfO}_2$ nanolaminates

Since both  $\text{Ta}_2\text{O}_5$  and  $\text{HfO}_2$  thin films on Si substrate were successfully fabricated by ALE, it is straightforward to grow  $\text{Ta}_2\text{O}_5$  –  $\text{HfO}_2$  nanolaminates by alternating the sequence of source materials. All the  $\text{Ta}_2\text{O}_5$  –  $\text{HfO}_2$  nanolaminates were deposited on nitrided silicon substrate at 300°C. A cross sectional view of the multilayer structure is shown in Fig. 4.15. By varying the number of cycles for each oxide constituent layer, one can determine the thickness of each intermediate layer and the total thickness of the stack.

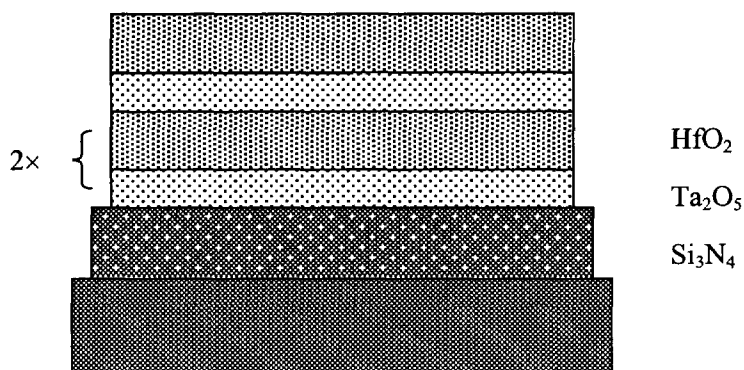


**Fig. 4.15 Schematic cross-section view of a  $\text{Ta}_2\text{O}_5$  –  $\text{HfO}_2$  nanolaminates structure of  $2 \times (\text{Ta}_2\text{O}_5 + \text{HfO}_2)$ . The thickness of each constituent layer can be varied by number of reaction cycles. The silicon nitride layer is 2.76 nm thick.**

For nanolaminates deposition, the pulses of source materials and  $\text{N}_2$  purge time were increased to ensure a smooth interface between the different oxide constituent layers. For ultra thin nanolaminates a  $\text{Ta}_2\text{O}_5$  seeding layer (5~10 cycles) was deposited before the sublayer was grown. The spectroscopic ellipsometer measured thickness was consistent with the thickness calculated from growth rate and number of reaction cycles. Our examination focused on very thin nanolaminates. The as-deposited  $\text{Ta}_2\text{O}_5$  –  $\text{HfO}_2$  nanolaminates were amorphous but crystallized after being annealed in a RTA furnace at  $800^\circ\text{C}$  for 30 s in either  $\text{O}_2$  or Ar ambient. The strongest diffraction peaks appeared in the XRD patterns corresponded to the monoclinic phase of  $\text{HfO}_2$ , while the  $\text{Ta}_2\text{O}_5$  showed only very weak crystallization. The determination of film composition was not possible even with Rutherford Backscattering Spectrometry (RBS) technique because the atomic weights of Ta and Hf are too close to each other, and the mass resolution of RBS is limited for heavy elements. The refractive index of the nanolaminate was 2.1 at a wavelength of 632.8 nm. The dielectric properties of  $\text{Ta}_2\text{O}_5$  –  $\text{HfO}_2$  nanolaminates with varied thickness were studied and the detailed discussion will be presented in Chapter 5.

### 4.5.2 Growth of $\text{Ta}_2\text{O}_5 - \text{ZrO}_2$ nanolaminates

Similar to the process of  $\text{Ta}_2\text{O}_5 - \text{HfO}_2$ ,  $\text{Ta}_2\text{O}_5 - \text{ZrO}_2$  nanolaminates were deposited on silicon or nitrided silicon substrates at  $300^\circ\text{C}$ . The schematic side-view of the multi-layer structure is the same as Fig. 4.15 except the  $\text{HfO}_2$  layer should be replaced by  $\text{ZrO}_2$  film. Since both  $\text{Ta}_2\text{O}_5$  and  $\text{ZrO}_2$  stick very well on bare Si substrate and nitrided Si substrate (a thin layer of  $\text{SiO}_2$  is formed at the interface again), it does not matter which oxide should be grown first. Only very thin  $\text{Ta}_2\text{O}_5 - \text{ZrO}_2$  nanolaminates (10 nm or less) were grown on nitrided silicon substrates. The as-deposited  $\text{Ta}_2\text{O}_5 - \text{ZrO}_2$  nanolaminates were also amorphous and was crystallized partially after  $700^\circ\text{C}$  annealing for 30 s in Ar or  $\text{O}_2$ . It is evident that a strong reflection peak of metastable t- $\text{ZrO}_2$  and two weak peaks of crystalline  $\text{Ta}_2\text{O}_5$  appeared, indicating the existence of nano-size crystallite phases. For nanolaminates with extremely thin constituent layer, for example, less than 5 nm, no obvious crystal sites would be detected by the X-ray diffractometer. This is due to the less chance for crystal growth for each oxide layer during the short exposure time of each precursor or X-ray could not detect the microcrystalline structure. The optical properties were characterized by spectroscopic ellipsometer. The refractive index was 2.0 and extinction coefficient was zero throughout the visible and near infrared region, which indicates that this film was optically transparent.

### 4.5.3 Growth of $\text{ZrO}_2 - \text{HfO}_2$ nanolaminates

The procedure for growing  $\text{ZrO}_2 - \text{HfO}_2$  nanolaminates is very much similar to that of the above two kinds of nanolaminates. More attention has been paid to sequence of binary oxide deposition on pure Si due to the unstable film formation when  $\text{HfO}_2$  was first deposited on Si. Therefore, during all the  $\text{ZrO}_2 - \text{HfO}_2$  nanolaminates deposition,  $\text{ZrO}_2$  was grown first in contact with the Si/ $\text{SiO}_2$  interface. Even this order does not have to be kept in the case of nitrided Si substrate, most nanolaminates of  $\text{ZrO}_2 - \text{HfO}_2$  on nitrided Si were grown in the same order since no difference in thickness from these two

orders was observed. The crystallization temperature of  $\text{ZrO}_2 - \text{HfO}_2$  nanolaminates is higher than that of  $\text{Ta}_2\text{O}_5\text{-ZrO}_2$ . It required  $800^\circ\text{C}$  to achieve partial crystallization for relatively thick  $\text{ZrO}_2 - \text{HfO}_2$  nanolaminates. It should be noted that only film with thickness less than 20 nm were investigated in details and the thickness of each constituent layer was less than 5 nm. There could be micro-crystallite structure with sub-nanometer scale, thus the XRD examination did not show any strong crystallization peaks.

So far in this chapter, the depositions of the binary oxides and nanolaminates have been described. Each film requires independent study related to the process parameters such as source temperatures, pulse times, purge duration and anneal temperature. The initial characterizations of these films were focused on crystalline structure and uniformity. The electrical and dielectric properties will be presented in Chapter 5.

## References

- [1] W. Kong, "Growth and characterization of thin film electroluminescent devices fabricated using atomic layer epitaxy," Ph.D. Dissertation, Oregon Graduate Institute, 1996, p. 31.
- [2] H. Shinriki and M. Nakata, "UV-O<sub>3</sub> and Dry-O<sub>2</sub>: Two-step annealed chemical vapor deposited Ta<sub>2</sub>O<sub>5</sub> films for storage dielectrics of 64-Mb DRAM's," IEEE Trans. Electron Devices **38**, 1991, pp. 455-462.
- [3] S. Kamiyama, P. Y. Lesaicherre, H. Suzuki, A. Sakai, I. Nishiyama, and A. Ishitani, "Ultrathin tantalum oxide capacitor dielectric layers fabricated using rapid thermal nitridation prior to low temperature chemical vapor deposition," J. Electrochem. Soc. **140**, 1993, pp. 1617-1624.
- [4] Y. Takaishi, M. Sakao, S. Kamiyama, H. Suzuki, and H. Watanabe, "Low temperature integrated process below 500°C for thin Ta<sub>2</sub>O<sub>5</sub> capacitor for giga-bit DRAMs," IEEE IEDM, San Francisco, CA, Dec. 11-14, 1994, p. 839-840.
- [5] K. F. Schuegraf, "Reliability of thin SiO<sub>2</sub> at direct-tunneling voltages," IEEE IEDM, San Francisco, CA, Dec. 11-14, 1994, p. 609-612.
- [6] G. S. Orhrlein, "Oxidation temperature dependence of the dc electrical conduction characteristics and dielectric strength of thin Ta<sub>2</sub>O<sub>5</sub> films on silicon," J. Appl. Phys. **59**, 1986, pp. 1587-1595.
- [7] S. O. Kim and H. J. Kim, "Fabrication of n-metal-oxide semiconductor field effect transistor with Ta<sub>2</sub>O<sub>5</sub> gate oxide prepared by plasma enhanced metal organic chemical vapor deposition," J. Vac. Sci. Technol. **B12**, 1994, pp. 3006-3009.
- [8] M. Ritala, M. Leskela, L. Niinisto, T. Prohaska, G. Friedbacher, and M. Grasserbauer, "Surface roughness reduction in atomic layer epitaxy growth of titanium dioxide thin films," Thin Solid Films **250**, 1994, pp. 155-162.
- [9] C. T. Kuo, R. Kwor, and K. M. Jones, "Study of sputtered HfO<sub>2</sub> thin films on silicon," Thin Solid Films **213**, 1991, pp. 257-264.
- [10] J. A. Britten, H. T. Nguyen, S. F. Falabella, B. W. Shore, M. D. Perry, and D. H. Raguin, "Etch-stop characteristics of Sc<sub>2</sub>O<sub>3</sub> and HfO<sub>2</sub> films for multiplayer dielectric grating applications," J. Vac. Sci. Technol. **A14**, 1996, pp. 2793-2795.



- [11] G. Johner and K. K. Schweitzer, "Thermal barrier coatings for jet engine improvement," *Thin Solid Films* **119**, 1984, pp. 301-315.
- [12] Y. Ma, Y. Ono, L. Stecker, D. R. Evans, and S. T. Hsu, "Zirconium oxide based gate dielectrics with equivalent oxide thickness of less than 1.0nm and performance of submicron MOSFET using a nitride gate replacement process," *Applied Surface Science*, **75**, 1994, pp. 333-340.
- [13] C. S. Hwang and H. J. Kim, "Deposition and characterization of  $\text{ZrO}_2$  thin film on silicon substrate by MOCVD," *J. Mater. Research* **8**, 1993, pp. 1361-1367.
- [14] J. Si, S. B. Desu, and C-Y Tsai, "Metal-organic chemical vapor deposition of  $\text{ZrO}_2$  films using  $\text{Zr}(\text{thd})_4$  as precursors," *J. Mater. Research* **9**, 1994, pp. 1721-1727.
- [15] M. Ritala and M. Leskela, "Zirconium dioxide thin films deposited by ALE using zirconium tetrachloride as precursor," *Applied Surface Science* **75**, 1994, pp. 333-340.
- [16] K. Kukli, M. Ritala, and M. Leskela, "Dielectric oxide nanolaminates deposited by atomic layer epitaxy," *Electrochem. Soc. Proc.* **25**, 1997, pp. 1137-1144.

## **Chapter 5**

### **Characterization of MOS Structures with High k Insulators**

Dielectric properties of binary oxides and nanolaminates are presented in this chapter. Material properties were characterized using variety of techniques. Film surface roughness was analyzed by an atomic force microscope (AFM). Chemical analysis was performed using FTIR. Composition profiles of different films were obtained from secondary ion mass spectroscope (SIMS). The electrical and optical properties were evaluated of thin films with different thicknesses. Dielectric constant was extracted from capacitance-voltage measurement. The dielectric constant decrease with film thickness is discussed. Gate leakage current mechanisms are presented for as-deposited and annealed thin films. The capacitance-voltage characteristics were measured with an HP4275 LCR meter. The current-voltage characteristics were analyzed using HP4145B parameter analyzer. The average thickness of binary oxides and nanolaminates were measured with an ellipsometer. Some thicknesses were verified by transmission electron microscope and SIMS profiles.

#### **5.1 Nitrided silicon substrate**

As we discussed in chap 4, silicon nitride was grown by RTP to act as a buffer layer to prevent the oxidation of silicon substrate during the high dielectric constant film growth. Our wafer came with the nitride layer. To reveal the doping concentration of the

Si substrate, the nitride layer was etched off by boiling in 75% phosphoric acid at 180°C. An aluminum dot was deposited on the exposed Si surface. C-V method was used to explore the doping level of the substrate according to the following equation [1]

$$N_A = \frac{2}{qk_s \epsilon_0 A^2 [d(1/C^2)/dV]} \quad (5.1)$$

where  $\epsilon_0$  is permittivity of free space,  $k_s$  is the dielectric constant of the substrate,  $A$  is the area of the aluminum dot. The calculated doping concentration was about  $1.0 \times 10^{15} \text{ cm}^{-3}$ . The FTIR spectrum of the nitrated substrate also indicated that the substrate was not heavily doped as shown in Fig. 5.1. The IR peak at  $1108 \text{ cm}^{-1}$  indicated interstitial oxygen atoms in Si lattice, and the peak at  $612 \text{ cm}^{-1}$  is due to substitutional carbon impurities in Si lattice. All other peaks are the phonon modes from the Si substrate. The nitride layer is fully transparent to the IR, so we were able to extract some information of the substrate underneath.

The surface roughness measurement of the silicon nitride layer was done using an atomic force microscope (AFM) as shown in Fig. 5.2. It was interesting to examine the roughness of the high dielectric film and compare it to the underlying nitride.

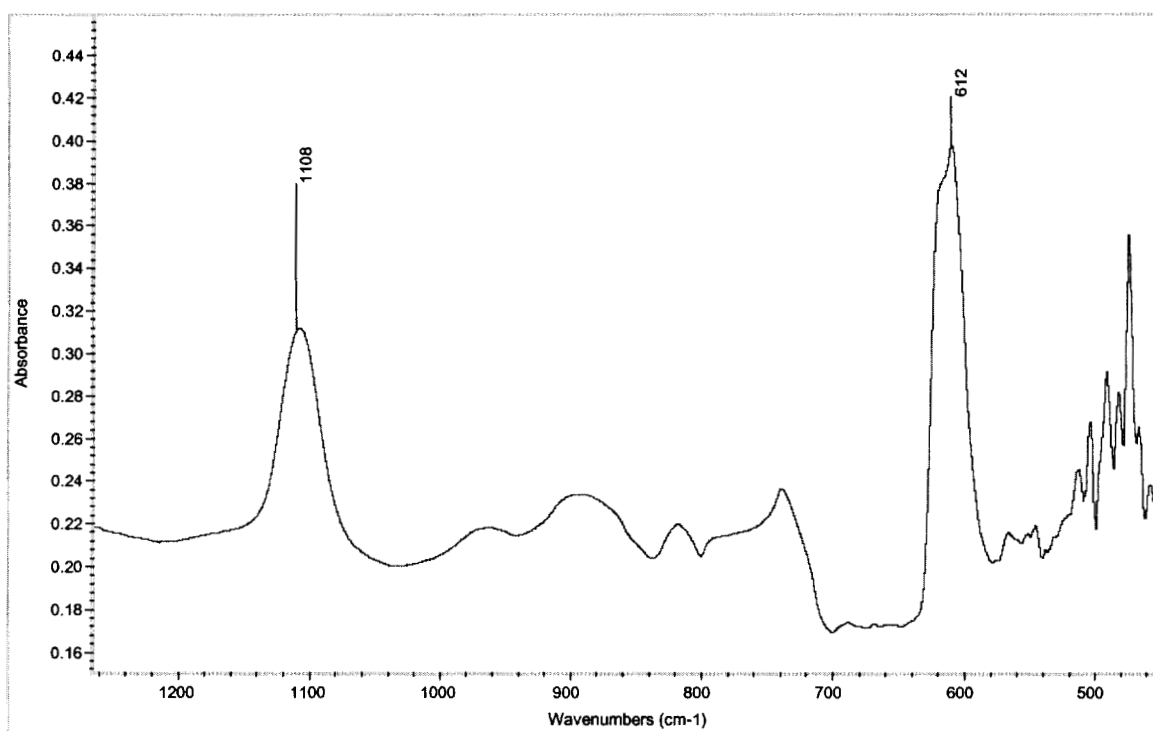


**Fig. 5.1 FTIR spectrum of the nitrided Si substrate.  
The thickness of the nitride layer is 2.76nm.**

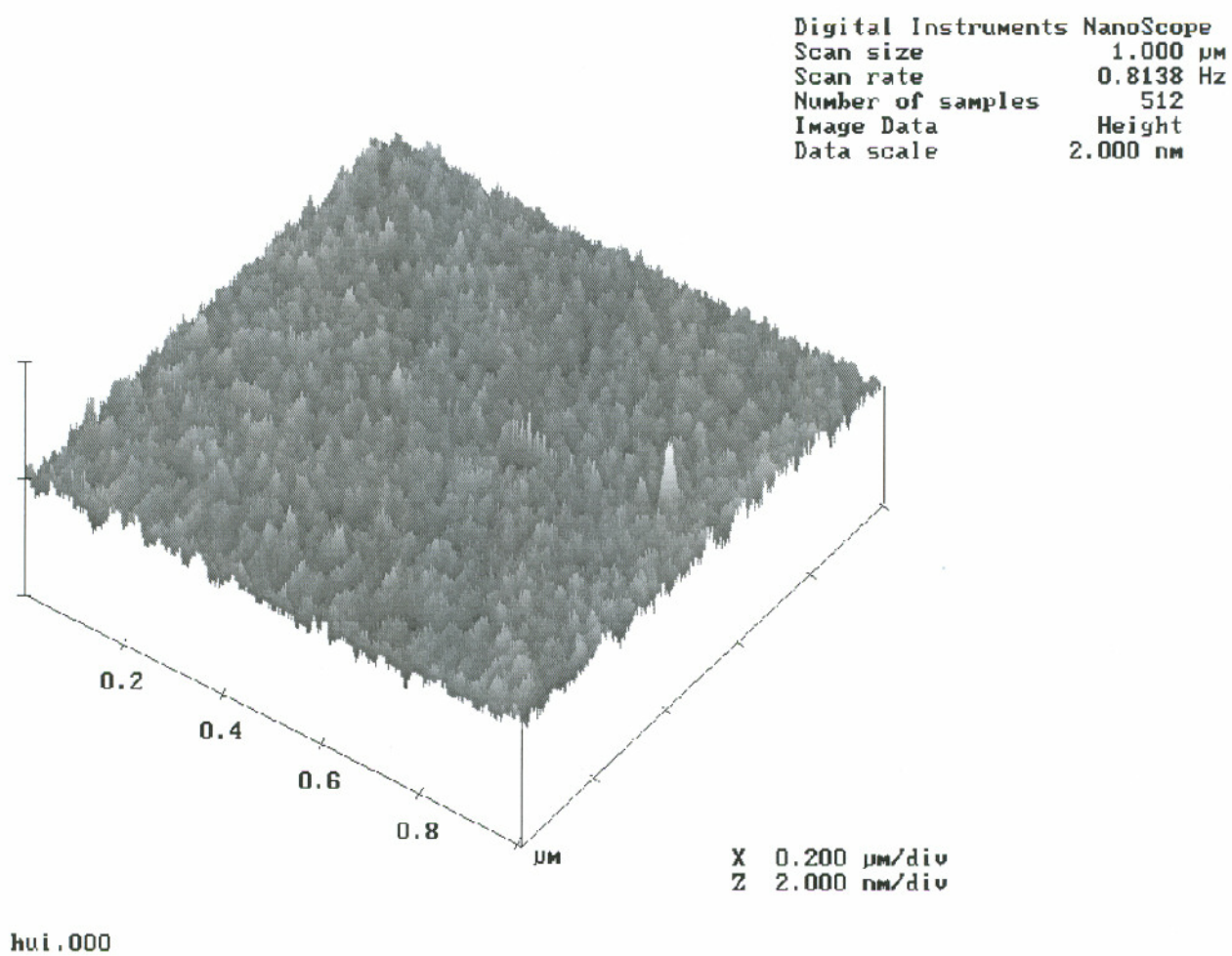


Fig. 5.2 AFM image of the silicon nitride layer of 2.76 nm, grown by rapid thermal annealing at 1000°C in ammonium for 30 s.

## 5.2. Material and electrical characterization of binary oxides

Al - Oxide - Si MOS structures were fabricated to determine the dielectric properties of binary oxide thin films. The Al dots of 0.4 ~ 0.6 mm diameter were evaporated on the top of the ALE grown oxides to define the MOS structures. The backsides of all these substrates were also aluminized to ensure a good back contact.

### 5.2.1. Ta<sub>2</sub>O<sub>5</sub> thin films

The dielectric constant of an insulator can be calculated by the capacitance-voltage measurement of a MOS capacitor in deep accumulation region. Bulk Ta<sub>2</sub>O<sub>5</sub> grown by ALE has a relatively high dielectric constant ( $k = 27$ ). In our investigation, Ta<sub>2</sub>O<sub>5</sub> was initially deposited on bare silicon substrates that were pre-cleaned and dipped in HF prior to loading into the reactor. The time between the HF dip and loading the sample into the ALE reactor was kept below 30 s to reduce any chances of oxidation. XRD analysis indicated these Ta<sub>2</sub>O<sub>5</sub> films to be amorphous as described in chapter 4. Secondary ion mass spectroscopy (SIMS) characterization showed the films to be stoichiometric, with no trace of chlorine. Two Ta<sub>2</sub>O<sub>5</sub> films were made for AFM study. Both samples were grown on nitrided Si at 300°C. In Fig. 5.3, Sample #322b1-2 was grown for 1000 cycles, which led to a thickness of about 55 nm; Sample 351b1-1 was grown for 80 cycles, which led to a thickness of about 4.4 nm. Both films were amorphous but the roughness of the thicker film is obviously more severe than that of the thinner film. This phenomenon has been reported by other authors [2,3]. It is interesting to see that the thinner Ta<sub>2</sub>O<sub>5</sub> film showed a smoother surface compared to the underlying Si<sub>3</sub>N<sub>4</sub>. Spectroscopic ellipsometry analysis showed that the as-deposited film of 75 nm had a refractive index of around 2.18 at 632.8 nm as shown in Fig. 5.4.

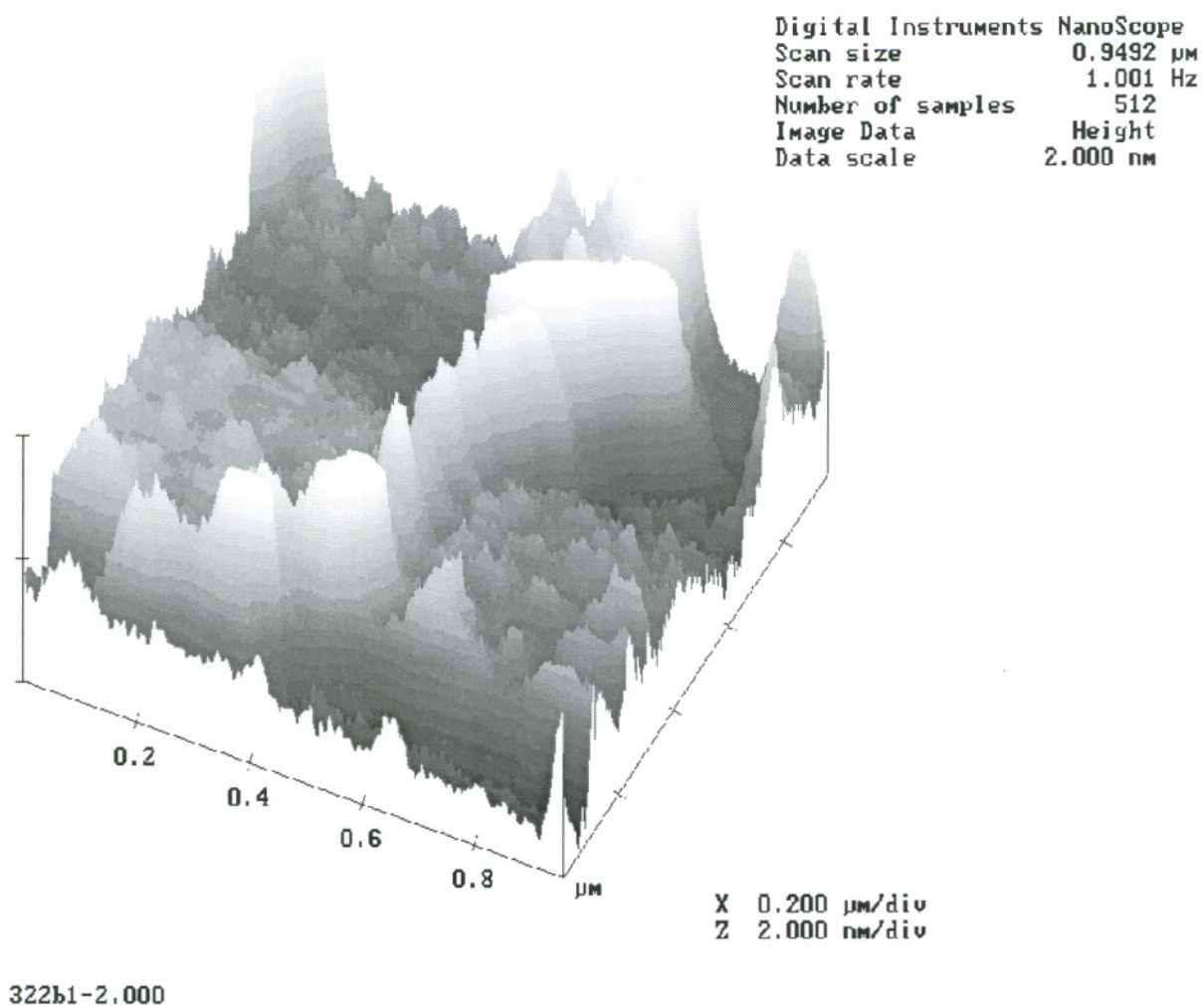


Fig. 5.3a AFM image of sample #322b1-2 on Si at 300°C for 1000 cycles  
(thickness  $\approx$  55nm)

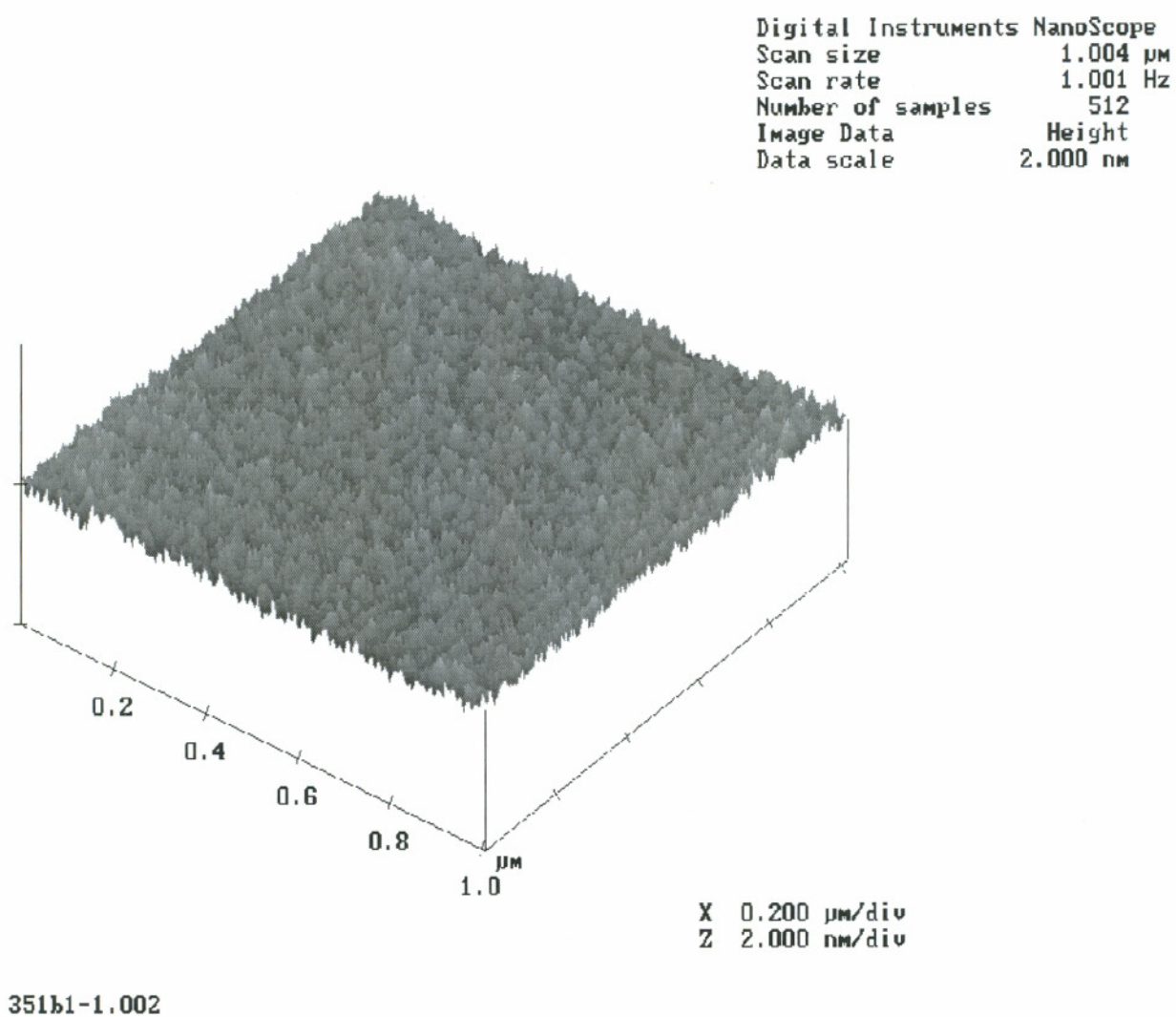


Fig. 5.3b AFM image of sample #351b1-1 on Si at 300°C for 80 cycles  
(thickness  $\approx 4.4$  nm)



We observed a significant difference in the dielectric properties for thick and thin films. For example, the  $k$  value of the 11.6 nm films was only 10 and a corresponding leakage current density was  $6 \times 10^{-6}$  A/cm<sup>2</sup> at 1 MV/cm. The values of  $k$  are significantly smaller than 27 which we had obtained from 75 nm thick Ta<sub>2</sub>O<sub>5</sub> grown on Si. These results are summarized in Table 5-1. As suspected, TEM cross-sectional profile of the thin Ta<sub>2</sub>O<sub>5</sub> film of 11.6 nm on bare Si showed a 1.5 nm thick layer of SiO<sub>2</sub> at the Si substrate/Ta<sub>2</sub>O<sub>5</sub> film interface, as showed in chapter 4. Apparently the silicon surface is getting oxidized during the initial growth phase of Ta<sub>2</sub>O<sub>5</sub> due to the presence of water vapor. Hence, the measured  $k$  value is that of the Ta<sub>2</sub>O<sub>5</sub> and SiO<sub>2</sub> capacitors in series. Dielectric constant of Ta<sub>2</sub>O<sub>5</sub> in this stack can be calculated according to Eqn. 5.2 and Eqn. 5.3. If we subtracted the effect of the 1.5 nm SiO<sub>2</sub> and assuming  $k$  of SiO<sub>2</sub> is 3.9, then the  $k$  value of the tantalum oxide film is 13.

$$\frac{1}{C_{meas(accum)}} = \frac{t_{SiO_2}}{\epsilon_{SiO_2}} + \frac{t_{Ta_2O_5}}{\epsilon_{Ta_2O_5}} \quad (5.2)$$

where  $C_{meas(accum)}$  is the capacitance per unit area of the MOS structure in the accumulation region.

The effective dielectric constant of the Ta<sub>2</sub>O<sub>5</sub> can then be derived from Eqn. 5.2,

$$\epsilon_{Ta_2O_5} = \frac{C_{meas(accum)} \epsilon_{SiO_2} t_{Ta_2O_5}}{\epsilon_{SiO_2} - C_{meas(accum)} t_{SiO_2}} \quad (5.3)$$

This equation can also be used for other interfacial layers instead of silicon oxide layer. For different stacks, it is hard to find the thickness of SiO<sub>2</sub> since its thickness varies with the thickness of the grown high  $k$  layer. Therefore, we will only consider the effective dielectric constant of the whole stack in most cases since we can not get a TEM picture for each film stack.

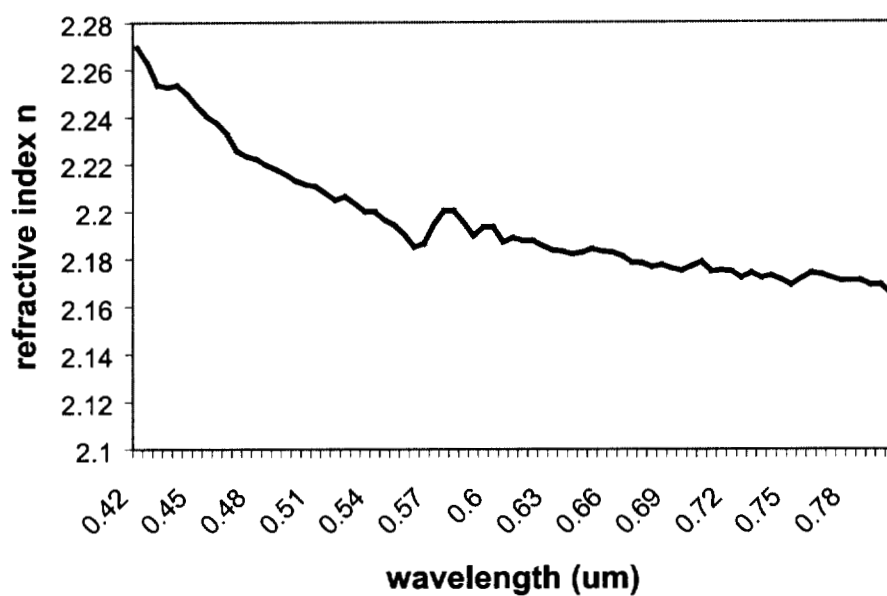


**Fig. 5.4** Refractive index of as-deposited  $\text{Ta}_2\text{O}_5$  film of 75 nm in the visible region.

**Table 5-1** Electrical properties of  $\text{Ta}_2\text{O}_5$  thin film grown on p-type Si substrate, where a thin layer of  $\text{SiO}_2$  exists at the interface due to the Si oxidation.

Total Thickness (nm)	Dielectric constant	Leakage current density ( $\text{A}/\text{cm}^2$ )(at $-1$ V)
75	27	$5.0 \times 10^{-11}$
36	15	$1.0 \times 10^{-11}$
12.1	10	$6.0 \times 10^{-6}$

In order to eliminate the native oxide growth, subsequent silicon substrates used were passivated with a 2 nm thick aluminum or a layer of silicon nitride of 2.76 nm or 2.12 nm thick. The idea of using Al as a passivation layer on Si was considered because Al has the heat of formation was reported to be higher than that of  $\text{SiO}_2$ , thus it would form aluminum oxide readily when exposed to water on the Si substrate.  $\text{Al}_2\text{O}_3$  films have a dielectric constant of 8.7 ~ 12.3 depending on the growth techniques. The  $\text{Al}_2\text{O}_3$  film grown by ALE has the k of 12.3. The  $\text{Al}_2\text{O}_3$  layer would also act as a barrier layer for further Si oxidation.

In this study, the Al was evaporated on Si at room temperature. Dielectric properties of  $\text{Ta}_2\text{O}_5$  films grown on Al passivated Si is summarized in Table 5-2. It is obvious that for thicker films, the dielectric properties are very close to bulk value for both as-deposited film and annealed film. Annealing caused the film to crystallize. Crystallization had more effect in increasing the dielectric constant for thinner film, and it also caused an increase in the leakage current due to the existence of grain boundaries that act as conductance channels. Using Al as a passivation layer is not an ideal method if we think about the low melting point of Al ( $\sim 660^\circ\text{C}$ ) and the diffusion between Al-Si at about  $400^\circ\text{C}$ . For any Al not fully oxidized during the deposition of  $\text{Ta}_2\text{O}_5$  film, chances of melting Al and diffusion between Al-Si will introduce a complicated interface. In addition, TEM cross-sectional view indicated that the Al is not a good barrier layer for water vapor diffusion, a layer of  $\text{SiO}_2$  was found at the interface of Si and  $\text{Al}_2\text{O}_3$  layer. Furthermore, the interface of the high k layer and the  $\text{Al}_2\text{O}_3$  layer was fairly rough and the thickness of  $\text{Al}_2\text{O}_3$  layer was hard to control. Therefore, we decided to replace  $\text{Al}_2\text{O}_3$  with silicon nitride as the passivation layer despite its relatively low dielectric constant compared to that of  $\text{Al}_2\text{O}_3$ .

**Table 5-2 Ta<sub>2</sub>O<sub>5</sub> films grown on Al passivated Si. The thickness of Al layer is 2 nm.**

Thickness (nm)	RTP	Refractive index	Dielectric constant	Leakage current (A/cm <sup>2</sup> ) at -1 V
75	-	2.194	26	$3.3 \times 10^{-12}$
75	1000°C in Ar for 10 s	2.195	27	$5.0 \times 10^{-11}$
38	-	2.123	16	$1.0 \times 10^{-11}$
38	1000°C in Ar for 10 s	2.228	19	$6.2 \times 10^{-11}$

Silicon nitride has been used as a passivation layer for a long time. It behaves as a nearly impervious barrier to diffusion especially for moisture and sodium. It also has a relatively high dielectric constant ( $\sim 7.8$ ), which makes it attractive as a gate dielectric material. The nitride layer in this research was deposited by rapid thermal nitridation in ammonia ambient at 1000°C for 30 s or less. Ta<sub>2</sub>O<sub>5</sub> films grown on nitrated silicon substrates showed no indication of an oxide layer at the interface. XRD analysis again showed amorphous films and ellipsometer measurements yielded refractive index (n) of 2.1 for films of 10 nm thick on silicon nitride.

The leakage current of as deposited Ta<sub>2</sub>O<sub>5</sub> is generally quite large and is attributed to oxygen vacancies and impurities in the film. Several post deposition treatments in oxidizing environments have been proposed to alleviate these defects [4-6]. We have examined the effect of post deposition thermal treatment using rapid thermal anneal (RTA) of our samples in both argon and oxygen ambients. The purpose of using both gases was to investigate if the leakage of the ALE grown films was due to oxygen vacancies. Results of two of these samples annealed (for 60 s) in these environments at 700°C and 800°C are compared in Table 5-3. After the 700°C anneal for 60 s, the k values in both cases increase and the leakage currents increased, most likely due to partial

crystallization of the films. However, following the 800°C anneal, leakage current increased even more in the case of Ar ambient and decreased in the O<sub>2</sub> ambient. XRD scans showed presence of the polycrystalline phase in both cases.

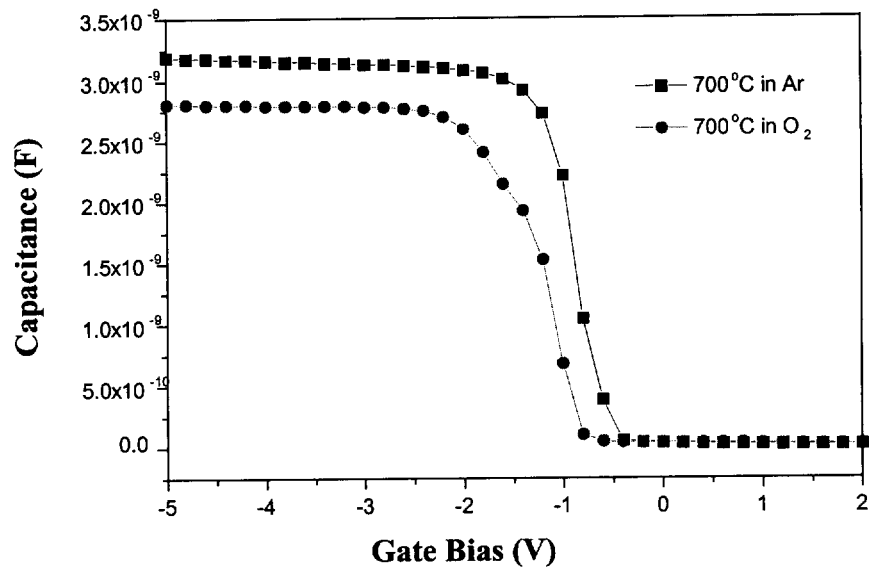
**Table 5-3 Electrical properties of Ta<sub>2</sub>O<sub>5</sub> / Si<sub>3</sub>N<sub>4</sub> after RTA in argon and oxygen ambients.**

Thickness(nm)	RTA for 60 s	Refractive index	Dielectric Constant	J (A/cm <sup>2</sup> ) at 1 MV/cm
17	None	2.2	15	2.5×10 <sup>-9</sup>
16	700°C in Ar	2.24	21	5.6×10 <sup>-8</sup>
16	700°C in O <sub>2</sub>	2.25	19	3.3×10 <sup>-7</sup>
17	800°C in Ar	2.25	21	2.0×10 <sup>-6</sup>
17	800°C in O <sub>2</sub>	2.24	21	1.9×10 <sup>-8</sup>

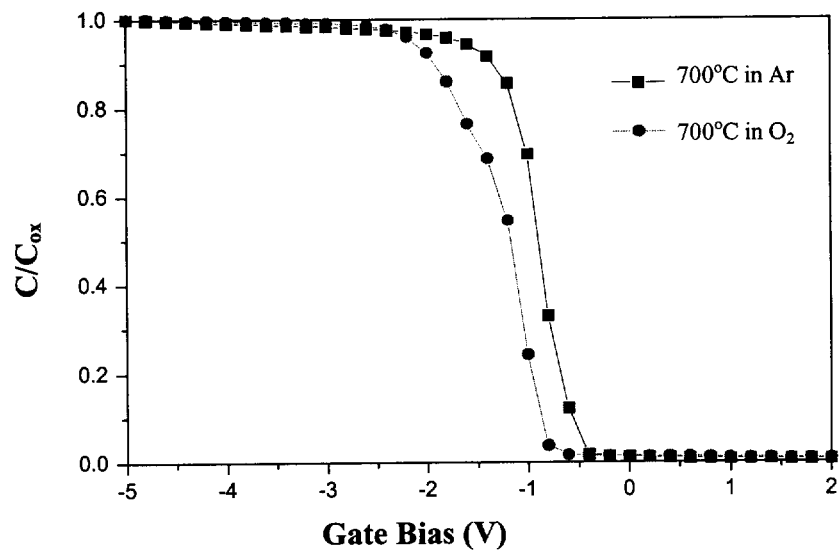
Fig. 5.5 shows the C-V curves of a 16 nm thick Ta<sub>2</sub>O<sub>5</sub> film annealed at 700°C in Ar and O<sub>2</sub> for 60 s. The capacitance in accumulation region showed a slight difference. The dielectric constant varied from 21 for Ar annealing to 19 for oxygen annealing. A lateral shift of about 0.4 V was also seen between the two curves in (b), the normalized C-V curves. Assuming that this lateral shift is due to difference of fixed charge located near the interface, its charge density can be calculated from

$$N = \frac{C_{ox} \Delta V}{q} \quad (5.4)$$

which is approximately 10<sup>10</sup> cm<sup>-2</sup>.



(a)



(b)

**Fig. 5.5** High frequency C-V curves for 16 nm thick of  $\text{Ta}_2\text{O}_5$  annealed at  $700^\circ\text{C}$  for 60 s in Ar and  $\text{O}_2$ . (a) C-V curve, (b) Normalized C-V curve.

The C-V characteristics of  $\text{Ta}_2\text{O}_5$  films annealed at  $800^\circ\text{C}$  is shown in Fig. 5.6. It is apparent from the C-V traces that annealing in oxygen reduces the interface state charge although no attempt was made to measure the  $D_{it}$  quantitatively at this point. The stretch-out in the C-V curve was due to the interface state charges [7]. The stretch-out for the  $\text{O}_2$  annealed thin film is much less severe than that observed in the Ar annealed sample, this also indicated a thermal silicon oxide layer could be formed at the Si surface that reduced the interface charge density significantly. As the Si surface oxidized, the thin layer of  $\text{SiO}_2$  will adversely affect the dielectric constant due to the low dielectric constant of  $\text{SiO}_2$ .

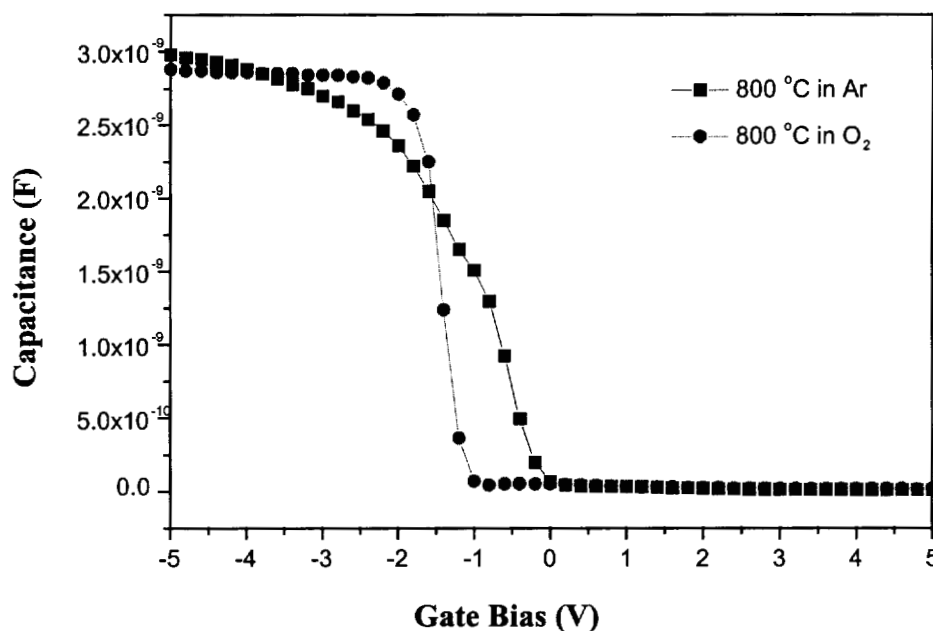


**Fig. 5.6 High frequency C-V curves for 17 nm thick of  $\text{Ta}_2\text{O}_5$  annealed at  $800^\circ\text{C}$  for 60 s in Ar and  $\text{O}_2$ .**

The leakage current also indicated a small discrepancy at 700°C for the two annealing ambients as shown in Fig. 5.7. It is surprising that the film annealed in O<sub>2</sub> is slightly more leaky than that annealed in Ar. However the difference is within an order of magnitude and we think it is within allowed margin of error. This indicated that the leakage current in ALE grown dielectric thin films is not due to the oxygen vacancies. There is a significant difference in the leakage current density for the films annealed at 800°C in Ar and O<sub>2</sub>. In the case of O<sub>2</sub> anneal, very low current was obtained at gate voltage lower than 2 V, then the leakage current increased as the gate voltage increased. We believe the onset of the increase in current is due to the tunneling current through the extremely thin silicon oxide layer (~ 1-2 nm) formed at the surface at high electric field. Here the crystallization of thin film and the existence of the thin silicon oxide layer play competitive roles in determination of the leakage current. The partial crystallization contributed to higher leakage current while silicon oxide layer reduced the leakage current dramatically. It is not surprising to note that the leakage current of 800°C-annealed film in Ar is two orders higher than the same thick film annealed in oxygen. We believe it is the presence of grain boundaries that facilitates the leakage current flow. There was no significant difference in dielectric constants of the films annealed in Ar and O<sub>2</sub>, therefore the dielectric films grown by ALE do not seem to have high density of oxygen vacancies.



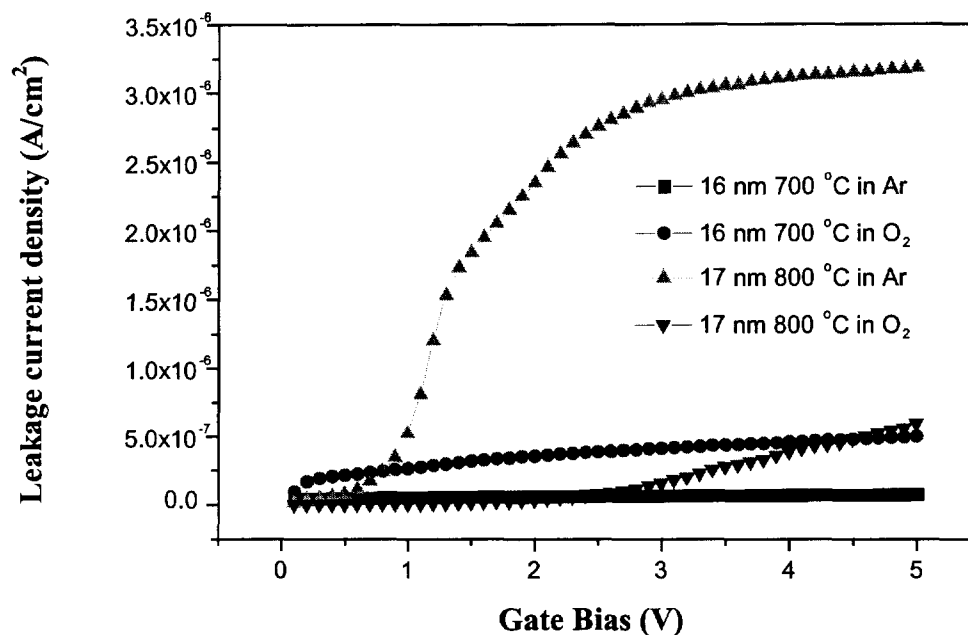


**Fig. 5.7** The leakage current density of MOS capacitors with 16 nm and 17 nm thick Ta<sub>2</sub>O<sub>5</sub> gate dielectric layers and under different annealing conditions.

The temperature dependence of leakage current was studied by measuring the I-V characteristics of thin films on a heated chuck. Fig. 5.8 shows the representative DC current-temperature plots at a bias of +2.0 volts for the as-deposited Ta<sub>2</sub>O<sub>5</sub> film and Ar annealed film, as a function of substrate temperature. Anneal in Ar ambient will introduce crystallization thereby increase the leakage current.  $J/T^2$  is found to follow standard Arrhenius behavior.

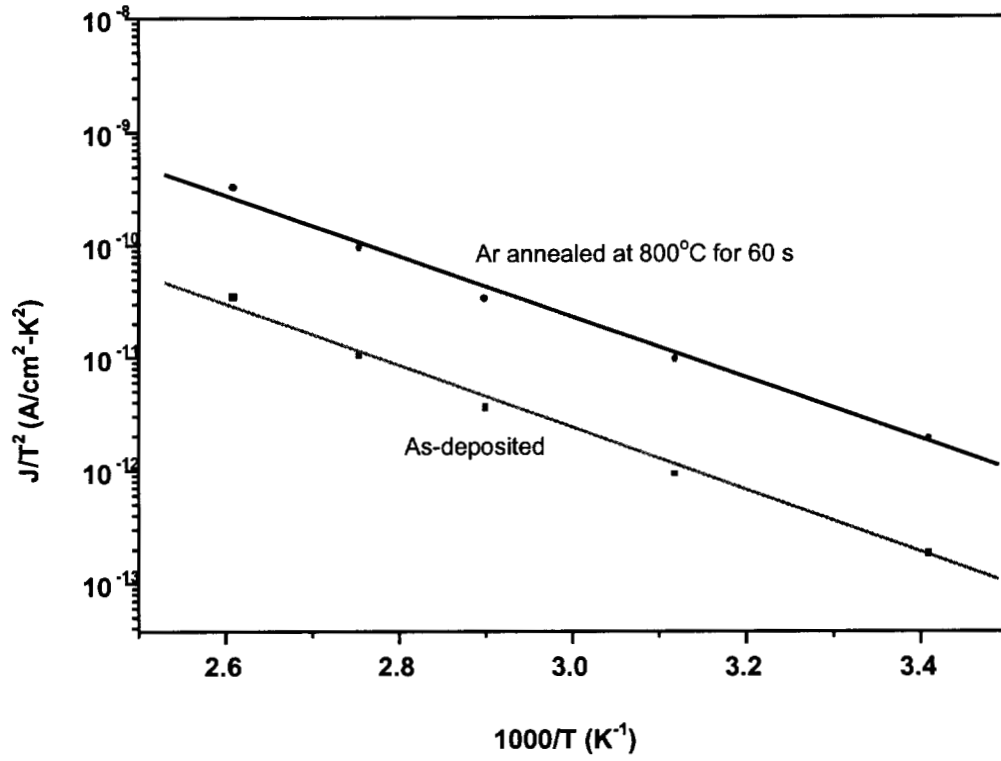


**Fig. 5.8  $J/T^2$  plots of gate leakage current under positive gate bias +2.0 volts for as-deposited and Ar annealed  $\text{Ta}_2\text{O}_5$  film of 17 nm.**

From Eqn. 5.5 of thermionic emission current,

$$J_{th} = \frac{4\pi m^* q}{h^3} k^2 T^2 \exp\left(-\frac{q[\Phi_B - \sqrt{qE/4\pi\epsilon_{ox}}]}{kT}\right) \quad (5.5)$$

we have

$$\ln \frac{J_{th}}{T^2} = -\frac{q[\Phi_B - \sqrt{qE/4\pi\epsilon_{ox}}]}{kT} + \ln \frac{4\pi m^* q k^2}{h^3} \quad (5.6)$$

the barrier height can then be extracted from the slope of the above equation

$$\Phi_B = -k \cdot \text{slope} + \sqrt{\frac{qE}{4\pi\epsilon_{ox}}} \quad (5.7)$$

The calculated barrier height was approximately 0.68 eV for the as-deposited Ta<sub>2</sub>O<sub>5</sub> film, whereas the Ar annealed film had a barrier height of 0.64 eV. It should be noticed that the permittivities of the two films were different. After anneal, the permittivity increased from 15 to 21. This slight decrease in barrier height with Ar anneal may be due to the crystallization of the film or it may represent a change in the band structure or a change in the charge state or strain at the Ta<sub>2</sub>O<sub>5</sub>/Si<sub>3</sub>N<sub>4</sub> interface.

When the films were made thinner, although the value of refractive index kept increasing slightly, the k value kept dropping as shown in Table 5-2. We do not believe that the drop in k value with the film thickness was due to the inferior property of the film. The little change in the refractive indices of the thinner films indicated that the quality of the thinner films was as good as that of thicker film or even better. Actually for the thinner film, the film density did not decrease, and the surface roughness was less severe compared to thicker films. It is more likely that reduction in k of thinner films (< 10 nm) was due to fewer bulk dipole moments between the two surfaces. In other words, the two surfaces of the ultra-thin film experience more of the outside world than the bulk between them, as discussed in ref. [8]. In our investigation, we found a significant drop in k values for films below 10 nm thick. Dielectric films with high k values are expected to be more affected by reduction of their thickness than low k materials.

### 5.2.2. HfO<sub>2</sub> and ZrO<sub>2</sub>

Zirconium and hafnium oxides grown by ALE have bulk  $k$  values of 21 and 16, respectively. Hf forms the most stable oxide with the highest heat of formation ( $\Delta H_f = 271$  Kcal/mol) among the elements in group IVA of the periodic table (Ti, Zr, Hf). HfO<sub>2</sub> film is very resistive to impurity diffusion and intermixing at the interface because of its high density (9.68 g/cm<sup>3</sup>). In addition, HfO<sub>2</sub> is compatible with n<sup>+</sup> polysilicon gate without any barrier materials. ZrO<sub>2</sub> is also one of the most promising candidates for high  $k$  material. It has a large energy bandgap from 5.16 to 7.8 eV [9,10], low leakage current, and can be etched in HF solution. In this study, both of these oxides were initially deposited on bare Si substrates, and subsequently on silicon nitride passivated Si as for the tantalum oxide. SIMS analysis showed both these films to be stoichiometric with no detectable chlorine. Refractive indices of HfO<sub>2</sub> and ZrO<sub>2</sub> were 2.1 and 2.15, respectively. The trends described above in the  $k$  values and leakage currents as the film thickness was reduced were again seen with these oxides.

For HfO<sub>2</sub> films grown on Si, the  $k$  value dropped from 16 for 27.6 nm thick films to 10 for 15 nm thick film on silicon. For the oxide films deposited on nitrated wafer, the dielectric constant of films with different thicknesses are tabulated in Table 5-4. The C-V characteristics are presented in Fig. 5.9.

**Table 5-4 Electrical properties of HfO<sub>2</sub>/ Si<sub>3</sub>N<sub>4</sub> with the thickness of Si<sub>3</sub>N<sub>4</sub> about 2.76nm or 2.12nm.**

Thickness (nm) HfO <sub>2</sub> / Si <sub>3</sub> N <sub>4</sub>	Dielectric constant	Leakage current (A/cm <sup>2</sup> )
24.8/2.76	16	$1.4 \times 10^{-8}$
9.84/2.76	11	$5.2 \times 10^{-8}$
11/2.12	10	$4.7 \times 10^{-8}$
5.7/2.12	8	$9.0 \times 10^{-8}$

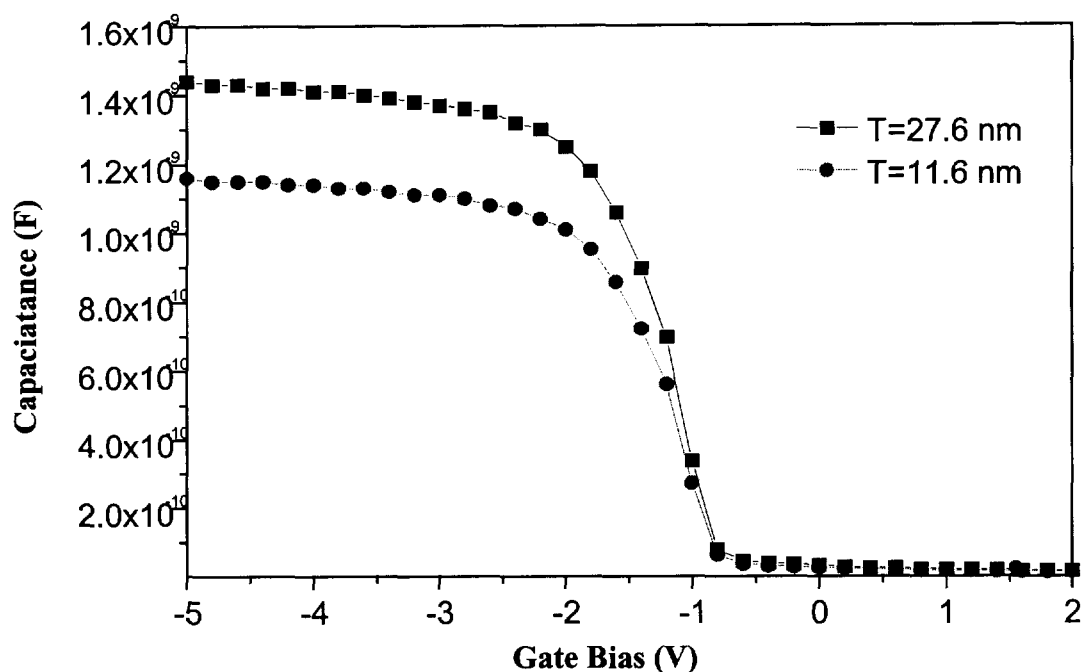


**Fig. 5.9 C-V characteristics of the HfO<sub>2</sub> thin films with thicknesses 27.6 nm and 11.6 nm respectively. The thicknesses include 2.76 nm of nitride. The area of the capacitor is 0.0028 cm<sup>2</sup>.**

In the case of ZrO<sub>2</sub> deposited on bare Si substrates, k value was 21 for 23 nm thick film and dropped to 16 for 17.8 nm thick film. A series of thinner films were grown on nitrated substrates as presented in Table 5-5.

**Table 5-5 Electrical properties of ZrO<sub>2</sub>/ Si<sub>3</sub>N<sub>4</sub> with the thickness of Si<sub>3</sub>N<sub>4</sub> about 2.76nm/2.12nm.**

Thickness (nm) ZrO <sub>2</sub> / Si <sub>3</sub> N <sub>4</sub>	Dielectric constant	Leakage current (A/cm <sup>2</sup> )
6.5/2.76	10	9.4×10 <sup>-8</sup>
18.4/2.12	21	1.7×10 <sup>-8</sup>
8.7/2.12	10	9.0×10 <sup>-8</sup>

It was interesting to note that HfO<sub>2</sub> films had the lowest leakage current of the three oxides examined. Also, the adhesion of HfO<sub>2</sub> films was significantly better on

nitrided Si than on bare Si surfaces. The surface chemistry of the  $\text{HfO}_2$  films growth on Si by ALE is not well understood, but it does not affect the use of  $\text{HfO}_2$  films to improve the dielectric properties of  $\text{Ta}_2\text{O}_5$  when a nitride layer is used as a passivation layer.

### **5.3 Material and electrical characterization of nanolaminates**

It has been shown that thin alternating layers (or nanolaminates) of insulators can be grown to produce a composite film whose insulating properties can be adjusted. The materials used for improving the dielectric properties of  $\text{Ta}_2\text{O}_5$  have been  $\text{HfO}_2$ ,  $\text{ZrO}_2$  and  $\text{Al}_2\text{O}_3$ . We have examined  $\text{Ta}_2\text{O}_5$  -  $\text{HfO}_2$ ,  $\text{ZrO}_2$  -  $\text{HfO}_2$ , and  $\text{Ta}_2\text{O}_5$  -  $\text{ZrO}_2$  nanolaminates that were grown on aluminum or nitride passivated silicon substrates.

#### **5.3.1 $\text{Ta}_2\text{O}_5$ - $\text{HfO}_2$ nanolaminates**

As we did for the  $\text{Ta}_2\text{O}_5$  film, our initial work on  $\text{Ta}_2\text{O}_5$  -  $\text{HfO}_2$  nanolaminates was performed on Al coated Si substrates. Two sets of nanolaminates were grown by ALE. Sample #1, #2, #3 and #4 were deposited at the same condition. Sample #1 and #2 were from the same run and so were #3 and #4. Small variations in thickness were observed from run to run. For as-deposited films, the ellipsometry measured thickness of as-deposited film matched well (deviation less than 5%) with the calculated thickness based on the growth rate of each constituent film. However, the thickness of annealed film measured by an ellipsometer showed obvious difference from what the TEM picture indicated. For example, samples #1 showed a thickness of 17 nm from ellipsometry but TEM presented a total thickness of 21 nm, including the high k layer (14.2 nm) and  $\text{Al}_2\text{O}_3/\text{SiO}_2$  (6.8 nm). Several issues need to be considered here. First, Al was proved not to be an ideal barrier for the water vapor as we pointed out earlier in this chapter. It was clear that a layer of  $\text{SiO}_2$  was formed at the Si surface. Annealing process helped in increasing the thickness of  $\text{SiO}_2$  by extracting oxygen from  $\text{Ta}_2\text{O}_5$  and  $\text{Al}_2\text{O}_3$ . Therefore we obtained a lower dielectric constant and lower leakage current for the annealed

samples due to the existence of the  $\text{Al}_2\text{O}_3/\text{SiO}_2$  stack. The dielectric characteristic dependence on annealing is summarized in Table 5-6.

Secondly, it is interesting to note that there was no appreciable difference in dielectric constant for the two different stacks of nanolaminates with the same total thickness if the thickness ratio of each binary oxide is kept the same in both stacks. We chose the number of  $\text{Ta}_2\text{O}_5$  growth cycles to be twice as that of  $\text{HfO}_2$  layer because the growth rate of  $\text{Ta}_2\text{O}_5$  is about half of that of  $\text{HfO}_2$ . To get the nanolaminates containing the same thickness of  $\text{Ta}_2\text{O}_5$  and  $\text{HfO}_2$ , the growth cycles of each constituent layer must be optimized accordingly. In fact, we would like to introduce less  $\text{HfO}_2$  to keep the dielectric constant high and also achieve lower leakage current. However, we used the same number of growth cycles for the subsequent very thin multilayer films because it was hard to get uniform deposition as the number of growth cycle decreases.

A dramatic increase of dielectric constant was achieved after the high temperature rapid thermal annealing treatment. RTA caused the crystallization of nanolaminates and therefore increased the leakage current as well.

**Table 5-6 The Ta<sub>2</sub>O<sub>5</sub>- HfO<sub>2</sub> nanolaminates grown on Al coated Si substrates with and without rapid thermal annealing.**

Sample	Film stack	Thickness (nm)	RTP (950°C, in Ar,10 s)	Thickness after RTP (nm)	Dielectric constant	Leakage current (A/cm <sup>2</sup> ) at 1 MV/cm
#1	2(50 Ta <sub>2</sub> O <sub>5</sub> +25 HfO <sub>2</sub> )	15.2	Yes	21.0	11	5.1×10 <sup>-8</sup>
#2	2(50 Ta <sub>2</sub> O <sub>5</sub> +25 HfO <sub>2</sub> )	15.4	No	-	19	3.5×10 <sup>-7</sup>
#3	4(25 Ta <sub>2</sub> O <sub>5</sub> +12 HfO <sub>2</sub> )	14.1	Yes	-	11	4.7×10 <sup>-8</sup>
#4	2(25 Ta <sub>2</sub> O <sub>5</sub> +12 HfO <sub>2</sub> )	14.2	No	-	18	5.8×10 <sup>-7</sup>



Due to the unpredictable surface reaction of aluminum with water vapor on silicon substrate before and after annealing, a better diffusion barrier layer such as silicon nitride was used to replace the aluminum passivation layer for the subsequent nanolaminates deposition. A series of  $\text{Ta}_2\text{O}_5$  -  $\text{HfO}_2$  nanolaminates were grown on the 2.76 nm or 2.12 nm silicon nitride and characterized by C-V and I-V measurements. Results from these films were summarized in Table 5-7. We have analyzed  $\text{Ta}_2\text{O}_5$  -  $\text{HfO}_2$  nanolaminates of thickness less than 10 nm. When these ultra-thin nanolaminates were deposited on silicon nitride coated Si substrates, the first few cycles were used for growing a thin  $\text{Ta}_2\text{O}_5$  film that acted as a seed layer. For this step, extended pulse time for  $\text{TaCl}_5$  and  $\text{N}_2$  purge were used. This was an effort to resolve the problem that the first few cycles of an ALE growth were not very uniform due to island growth. This problem would be more obvious for nanolaminates growth since alternate precursors were switched frequently. It was reported that the ALE film roughening has its origin in agglomeration, which was most intense during the very first few deposition cycles. Substrate surface cleanliness may also be an issue for the island growth for the first few cycles. For our nitrided substrates, no special cleaning was performed besides blowing with dry  $\text{N}_2$ . However, once the grown film fully covered the substrate, the surface of subsequent film becomes smoother. An AFM image showed very uniform and flat surface as presented in Fig. 5.10.

**Table 5-7 The Ta<sub>2</sub>O<sub>5</sub>- HfO<sub>2</sub> nanolaminates growth on nitrided Si substrates. The thickness of Si<sub>3</sub>N<sub>4</sub> is 2.76 nm.**

Sample	Film stack	Total Thickness (nm)	Dielectric constant	SiO <sub>2</sub> equivalent thickness (nm)	Leakage current density (A/cm <sup>2</sup> ) at 1 MV/cm
#1	10 Ta <sub>2</sub> O <sub>5</sub> + 2(25 Ta <sub>2</sub> O <sub>5</sub> +25 HfO <sub>2</sub> )	10	12	3.25	2.0×10 <sup>-7</sup>
#2	10 Ta <sub>2</sub> O <sub>5</sub> + 2(20 Ta <sub>2</sub> O <sub>5</sub> +20 HfO <sub>2</sub> )	9.6	10	3.74	1.7×10 <sup>-7</sup>
#3	10 Ta <sub>2</sub> O <sub>5</sub> + 2( 10 Ta <sub>2</sub> O <sub>5</sub> +10 HfO <sub>2</sub> )	8.0	10	3.12	3.8×10 <sup>-8</sup>
#4	5 Ta <sub>2</sub> O <sub>5</sub> + 2(5 Ta <sub>2</sub> O <sub>5</sub> +5 HfO <sub>2</sub> )	6.8	10	2.65	1.2×10 <sup>-8</sup>

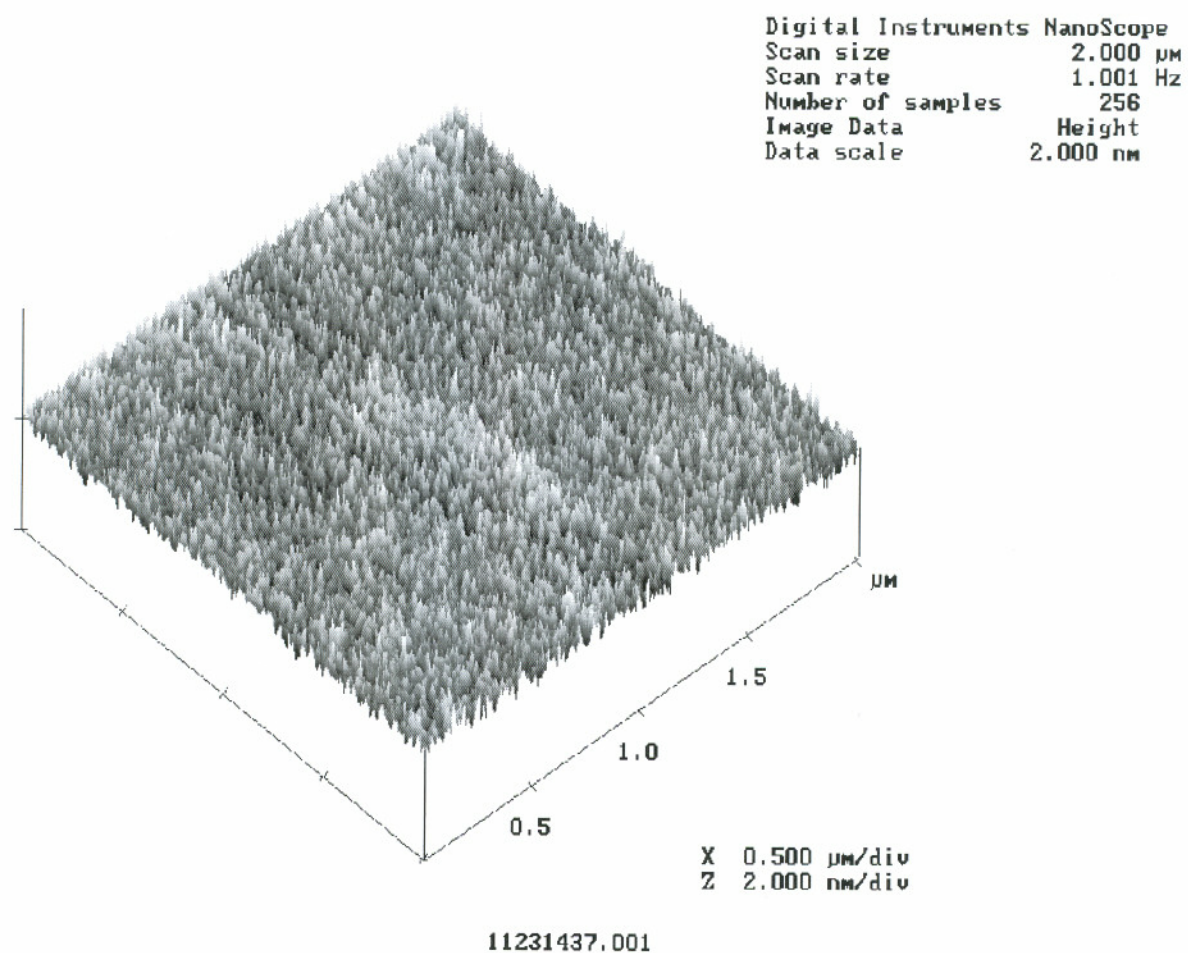
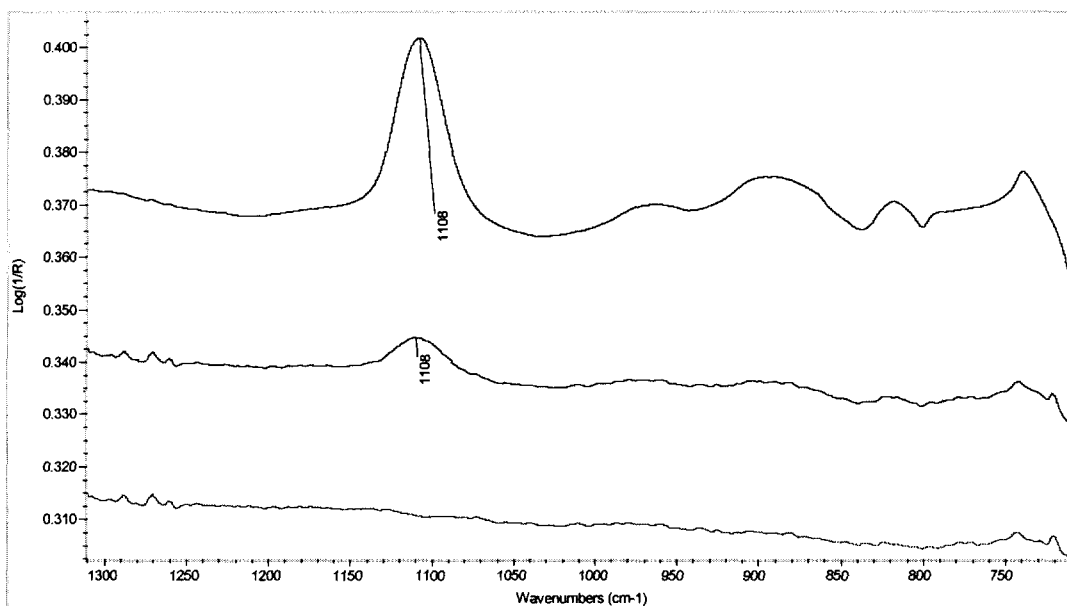


Fig. 5.10 An AFM image of the Ta<sub>2</sub>O<sub>5</sub> - HfO<sub>2</sub> nanolaminates. The stack is 5 Ta<sub>2</sub>O<sub>5</sub> + 2 × (10 Ta<sub>2</sub>O<sub>5</sub> + 10 HfO<sub>2</sub>).

Ultra thin  $\text{Ta}_2\text{O}_5$ -  $\text{HfO}_2$  nanolaminates ( $5 \text{ Ta}_2\text{O}_5 + 2 \times (10 \text{ Ta}_2\text{O}_5 + 10 \text{ HfO}_2)$ ) were also studied by FTIR to determine if there was any oxidation occurring at the silicon surface during the ALE process. If silicon oxide is formed at the interface, this IR spectrum will show peaks for Si-O bonding. To check for the presence of the Si-O bond due to the interstitial oxygen in Si matrix, which exists before the nanolaminates process, the FTIR spectrum of nitrided substrate was also examined. A subtraction of these two IR spectra indicated that there was no Si-O bond forming due to the process, as shown in Fig. 5.11.



**Fig. 5.11 FTIR spectra of  $\text{Ta}_2\text{O}_5/\text{HfO}_2$  nanolaminates/ $\text{Si}_3\text{N}_4/\text{Si}$  and  $\text{Si}_3\text{N}_4/\text{Si}$ . The top curve is the spectrum of the nanolaminates, the middle one is nitrided silicon substrate, the bottom one is the subtraction of two curves showing that there is no  $\text{SiO}_2$  forming at the interface.**

X-ray reflectivity (XRR) was used to verify the total thickness and film density for nanolaminates on Si and on  $\text{Si}_3\text{N}_4/\text{Si}$ . Glancing angle  $\theta$ - $2\theta$  measurements were done using the Siemens D5000 XRD. It is evident that the thickness measured by spectroscopic ellipsometer was consistent with the XRR thickness (variation less than 3%). But the thickness from the single wavelength ellipsometer was 10-15% larger than that measured by the other two methods. XRR also measured the film density of 0.87-0.88 relative to bulk  $\text{HfO}_2$ . No interfacial silicon dioxide was detected for the film grown on nitride. It proved that silicon nitride is an effective barrier layer against water vapor in this process.

Again the dielectric constants of nanolaminates were extracted from the C-V measurements. Fig. 5.12 is a typical high frequency C-V curve of as-deposited  $\text{Ta}_2\text{O}_5$ - $\text{HfO}_2$  nanolaminates of 7.3 nm grown on 2.76 nm silicon nitride coated substrate, from which a dielectric constant of 12 was determined with the gate area of  $0.0028 \text{ cm}^2$ . Hence this stack is electrically equivalent to 3.25 nm of  $\text{SiO}_2$ . The leakage current at 1MV/cm was  $2.0 \times 10^{-7} \text{ A/cm}^2$ .

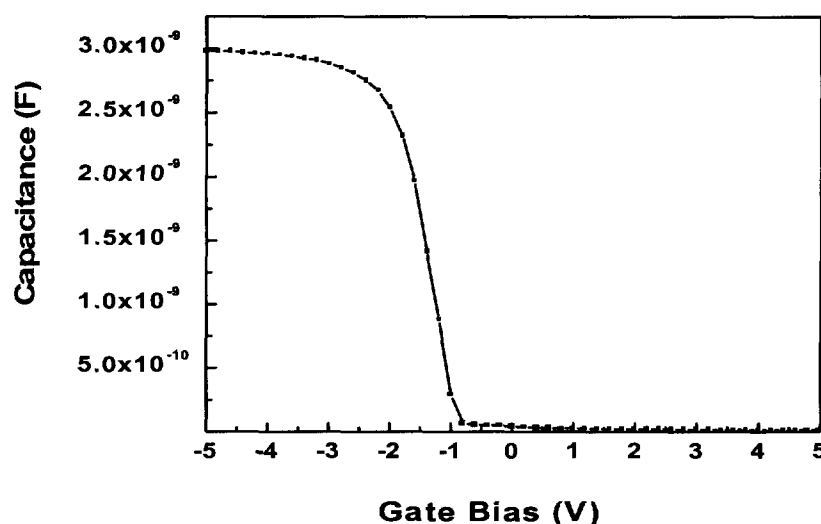


**Fig. 5.12 C-V curve of the as-deposited Al-  $\text{Ta}_2\text{O}_5/\text{HfO}_2$ - $\text{Si}_3\text{N}_4$ -Si (MIS) capacitor. The  $\text{Ta}_2\text{O}_5/\text{HfO}_2$  nanolaminates contains  $10\text{Ta}_2\text{O}_5+2(25 \text{Ta}_2\text{O}_5+25 \text{HfO}_2)$ . The area of the capacitor is  $2.8 \times 10^{-3} \text{ cm}^2$ .**

The flatband voltage is defined as the gate bias at which the transition from an accumulation to depletion in the surface of a MOS system occurs. It can be experimentally determined from C-V curve by plotting the  $1/(C_{HF}/C_{OX})^2$  versus  $V_g$ . The lower knee of this curve occurs at  $V_g = V_{FB}$ . Such a transition is sometimes difficult to determine unambiguously. Differentiating this curve and finding the maximum slope of the left flank of this differentiated curve again results in a sharply peaked curve where the VFB is the gate bias corresponding to the peak position [11]. Fig. 5.13 indicated that for this Ta<sub>2</sub>O<sub>5</sub>-HfO<sub>2</sub> nanolaminates the flatband voltage ( $V_{FB}$ ) is about -1.1 V.

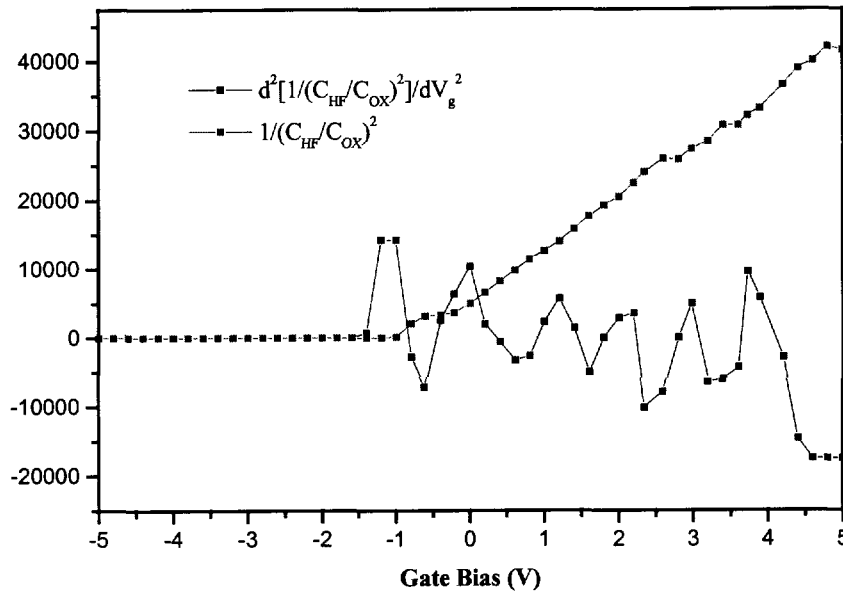


**Fig. 5.13 Calculation of the flatband voltage from a C-V measurement. The gate voltage corresponds to the peak of  $\frac{d^2}{dV_g^2} \left[ \frac{1}{(C_{HF}/C_{ox})^2} \right]$  was the flatband voltage.**

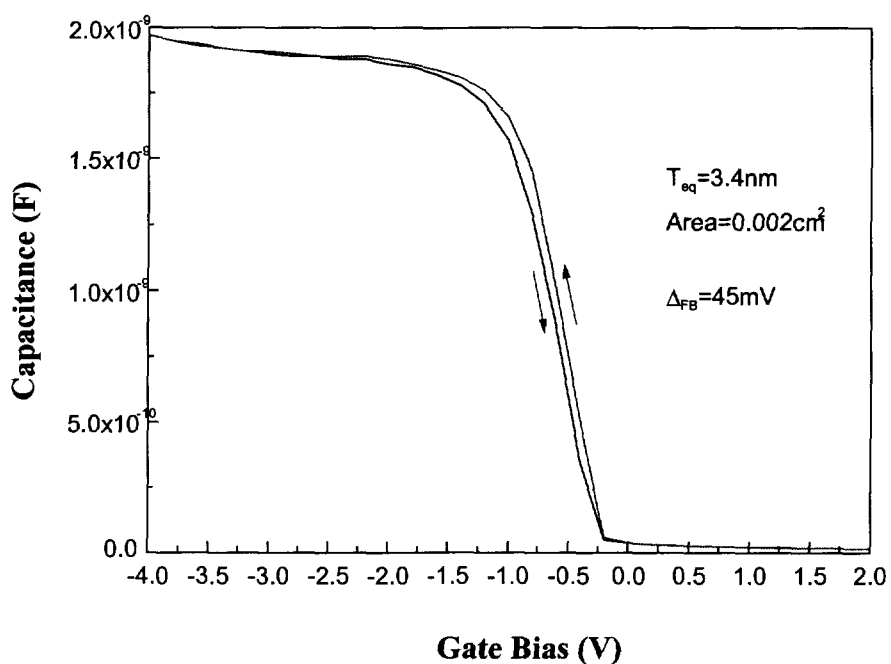
The fixed charge  $Q_f$  is related to the flatband voltage and gate-semiconductor work function difference by equation

$$Q_f = (\phi_{MS} - V_{FB})C_{ox} \quad (5.8)$$

$$N_f = \frac{Q_f}{qA} \quad (5.9)$$

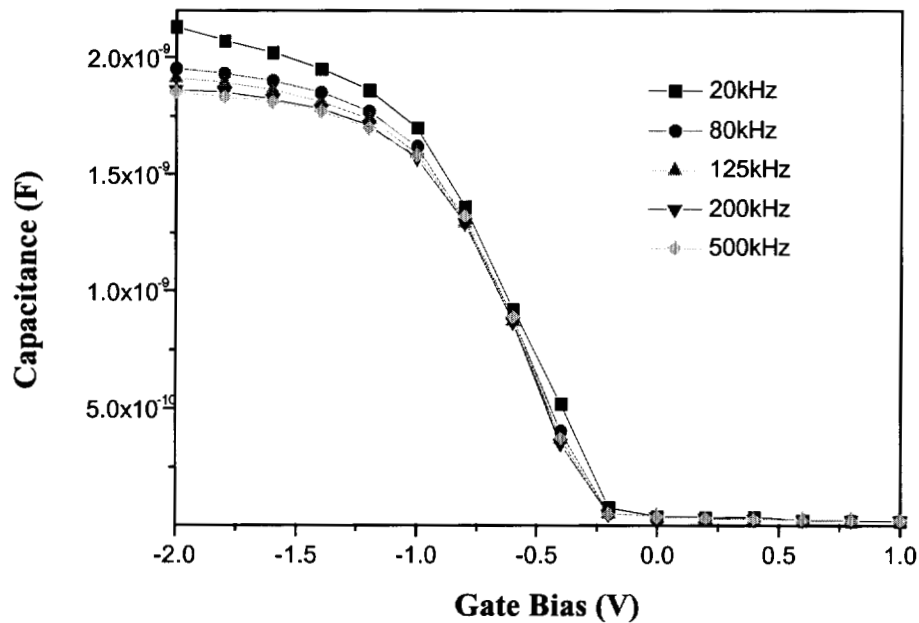
where  $A$  is the capacitor area in  $\text{cm}^2$ ,  $\phi_{\text{MS}}$  was calculated based on the doping concentration of the substrate assuming it was uniformly doped. The calculated fixed charge density was  $8.3 \times 10^{10} \text{ cm}^{-2}$ .

Fig. 5.14 showed that the amount of hysteresis is about 45mV for a voltage sweep from  $-4.0\text{V}$  to  $2.0\text{V}$ , which is believed to be due to charge trapping and detrapping. The small hysteresis indicated the  $\text{Ta}_2\text{O}_5$  -  $\text{HfO}_2$  nanolaminates with the  $\text{Si}_3\text{N}_4$  as the barrier layer has good film quality.



**Fig. 5.14 Hysteresis characteristic of  $\text{Ta}_2\text{O}_5$ - $\text{HfO}_2/\text{Si}_3\text{N}_4$  nanolaminates, the  $\text{Ta}_2\text{O}_5$ - $\text{HfO}_2$  is  $5 \text{ Ta}_2\text{O}_5 + 10(8 \times \text{Ta}_2\text{O}_5 + 8 \times \text{HfO}_2)$  and  $\text{Si}_3\text{N}_4$  is  $2.12 \text{ nm}$ .**

There was no significant frequency dependence of capacitance ( $<1\%$ /decade) for most process conditions as shown in Fig. 5.15. However, the capacitance measured at 20kHz was significantly higher than other higher frequencies. This frequency dependence was possibly due to the presence of fast interface state charges. All C-V measurements used to determine the dielectric constant were performed at 200 kHz, therefore the effect of interface charges could be eliminated.



**Fig. 5.15** Frequency dependency of C-V curve of  $\text{Ta}_2\text{O}_5\text{-HfO}_2/\text{Si}_3\text{N}_4$  nanolaminates, the  $\text{Ta}_2\text{O}_5\text{-HfO}_2$  is  $5 \text{ Ta}_2\text{O}_5 + 10(8 \times \text{Ta}_2\text{O}_5 + 8 \times \text{HfO}_2)$  and  $\text{Si}_3\text{N}_4$  is 2.12 nm.

Leakage current is an issue of critical concern in gate dielectrics. Many investigations have used elaborate processes such as  $\text{N}_2\text{O}$  annealing [12], plasma  $\text{O}_2$  annealing [13,14], and two-step annealing [15,16] to improve the leakage current levels of  $\text{Ta}_2\text{O}_5$  capacitors. Results in this study demonstrate the leakage current of amorphous nanolaminate structure is lower than that of pure binary oxides.



In dielectric films, there are several possible mechanisms responsible for the leakage current. These mechanisms include Schottky emission, Poole-Frenkel emission, Fowler-Nordheim tunneling, direct tunneling and a space charge limited current. A detailed discussion was presented in Chapter 2. Considering our bias conditions and film thickness, Schottky and Poole-Frenkel emissions would be the dominant leakage mechanisms for these samples. The Schottky emission can be expressed as follows,

$$J \propto T^2 \exp \left[ \frac{q(-\phi_B) + \sqrt{qE/4\pi k \epsilon_0}}{k_B T} \right] \quad (5.10)$$

and the Poole-Frenkel emission can be described as:

$$J \propto E \exp \left[ \frac{q(-\phi_B) + \sqrt{qE/\pi k \epsilon_0}}{k_B T} \right] \quad (5.11)$$

where  $J$  represents leakage current density,  $T$  is absolute temperature,  $k_B$  is Boltzmann constant,  $q$  represents electronic charge,  $E$  is electric field,  $\phi_B$  represents barrier height and  $k$  denotes the dielectric constant of the investigated insulator material.

The I-V characteristic of  $\text{Ta}_2\text{O}_5 - \text{HfO}_2$  nanolaminate annealed at  $1000^\circ\text{C}$  in Ar for 10 s was displayed in Fig. 5.16. In order to determine the leakage mechanisms in the ultra-thin nanolaminates, the logarithm of the current density was plotted against the electric field. For example, in Fig. 5.17 the logarithmic current density is plotted as a function of the square root of electric field  $[\ln(J) \text{ vs. } E^{1/2}]$  for  $\text{Ta}_2\text{O}_5 - \text{HfO}_2$  nanolaminate stack. A straight line was obtained at low electric fields ( $<0.4 \text{ MV/cm}$ ) implying Schottky emission [17]. At higher electric field conduction is governed by a different mechanism. In Fig. 5.18 the logarithmic current density divided by the electric field was plotted as a function of the square root of the electric field  $[\ln(J/E) \text{ vs. } E^{1/2}]$ . A

straight line was obtained at a high electric field ( $> 0.4$  MV/cm), suggesting that the leakage current at high electric field is due to the Poole-Frenkel conduction mechanism [18,19].

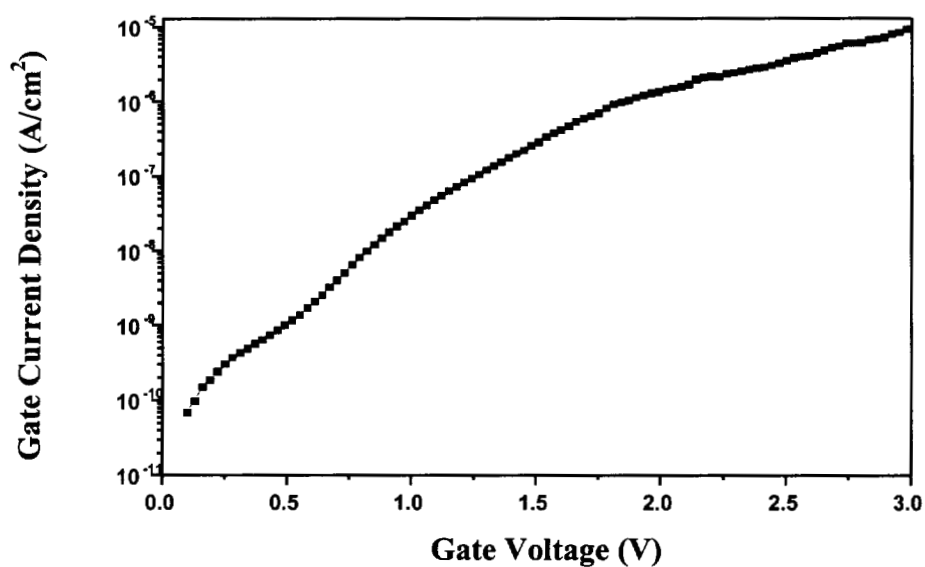


**Fig. 5.16** The leakage current density vs applied voltage for the Al-Ta<sub>2</sub>O<sub>5</sub>/HfO<sub>2</sub>-Si<sub>3</sub>N<sub>4</sub>-Si capacitor. The thickness of the nanolaminates was 7.4 nm. The area of the capacitor is 0.0028 cm<sup>2</sup>.

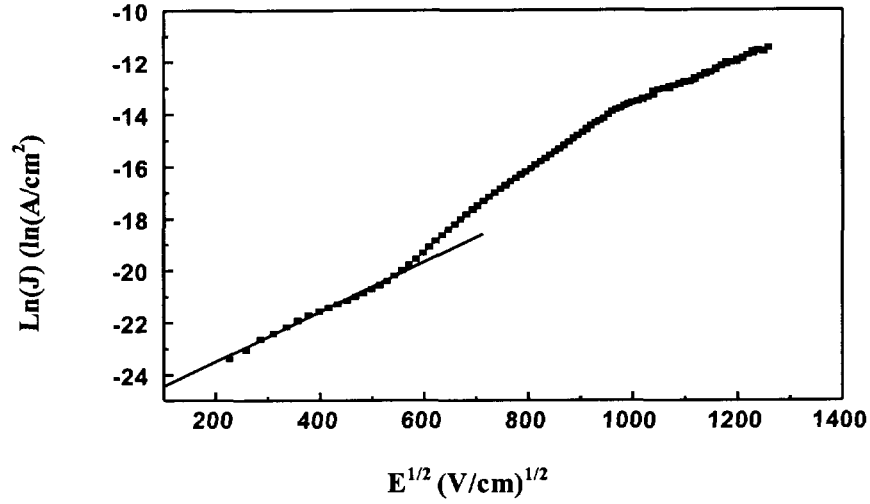


**Fig. 5.17** The  $\ln(J)$  vs  $E^{1/2}$  is plotted for the Al-Ta<sub>2</sub>O<sub>5</sub>/HfO<sub>2</sub>-Si<sub>3</sub>N<sub>4</sub>-Si (MIS) capacitor. The straight line characteristic at low electric field ( $< 0.4$  MV/cm) indicates Schottky emission.

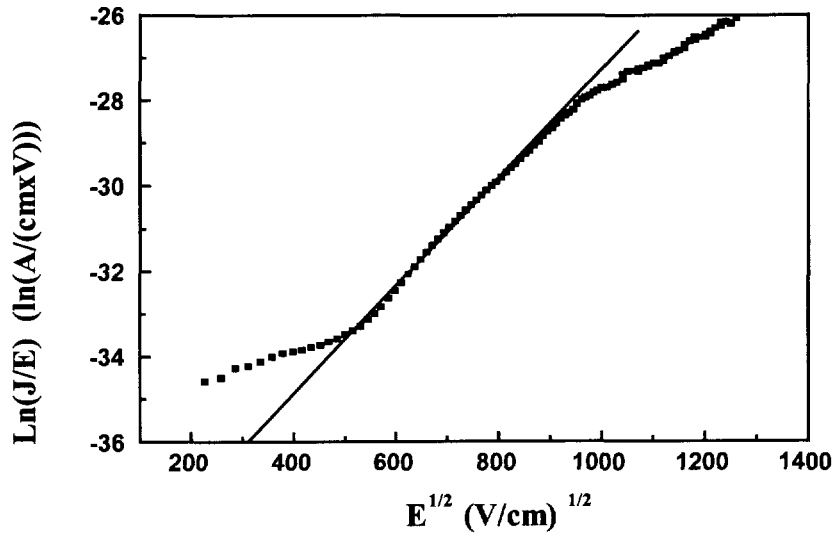


**Fig. 5.18** The  $\ln(J/E)$  vs  $E^{1/2}$  is plotted for the Al-Ta<sub>2</sub>O<sub>5</sub>/HfO<sub>2</sub>-Si<sub>3</sub>N<sub>4</sub>-Si (MIS) capacitor. The straight-line characteristic at relative high electric field ( $> 0.4$  MV/cm) indicates Poole-Frenkel conduction.

### 5.3.2 Ta<sub>2</sub>O<sub>5</sub>-ZrO<sub>2</sub> nanolaminates

Pure ZrO<sub>2</sub> films have showed high permittivity (21) and lower leakage current compared to pure Ta<sub>2</sub>O<sub>5</sub> thin film. Therefore, ZrO<sub>2</sub> is a good candidate to be incorporated with Ta<sub>2</sub>O<sub>5</sub> thin films. Because the refractive index of bulk ZrO<sub>2</sub> is comparable with that of Ta<sub>2</sub>O<sub>5</sub> film, the nanolaminates have shown a fairly high refractive index of 2.1.

A series of Ta<sub>2</sub>O<sub>5</sub>-ZrO<sub>2</sub> nanolaminates were grown on bare Si and Si<sub>3</sub>N<sub>4</sub> coated substrate. For nanolaminates grown on bare Si wafer, a layer of SiO<sub>2</sub> was expected at the Si/nanolaminates interface due to the silicon oxidation and it was confirmed by a TEM image. Ta<sub>2</sub>O<sub>5</sub>-ZrO<sub>2</sub> nanolaminates deposited on Si substrates were also analyzed by C-V and I-V measurements, as summarized in Table 5-8. For these samples, the thickness ratio of Ta<sub>2</sub>O<sub>5</sub> to ZrO<sub>2</sub> equals to 12%: 88%. Highest permittivity was reported for Ta<sub>2</sub>O<sub>5</sub>-ZrO<sub>2</sub> nanolaminates at this ratio [20]. As seen from some TEM images, the thickness of the interfacial SiO<sub>2</sub> layer varies with the grown nanolaminates, which made it difficult to calculate the effective dielectric constant of the nanolaminates. Therefore the k values listed in Table 5-8 are the effective dielectric constant of the Ta<sub>2</sub>O<sub>5</sub>-ZrO<sub>2</sub> nanolaminates/SiO<sub>2</sub> stack. Leakage current was measured at (V<sub>t</sub> +1) volt. T<sub>eq,ox</sub> is the electrical equivalent thickness of SiO<sub>2</sub>.

**Table 5-8 Ta<sub>2</sub>O<sub>5</sub>-ZrO<sub>2</sub> nanolaminates deposited on Si substrates.  
The thickness ratio of Ta<sub>2</sub>O<sub>5</sub>: ZrO<sub>2</sub> is 12% : 88%.**

Thickness (nm)	k	T <sub>eq,ox</sub> (nm)	Leakage current (A/cm <sup>2</sup> )
82	21	15.2	8.4×10 <sup>-9</sup>
48	16	11.7	8.4×10 <sup>-9</sup>
37	16	9.0	4.2×10 <sup>-9</sup>
15	11	5.3	3.4×10 <sup>-7</sup>
10.2	10	3.9	3.7×10 <sup>-6</sup>

To avoid the reduction of permittivity due to the Si oxidation during exposure to water vapor, another set of samples were deposited on the nitrided silicon wafer. This time our investigation was focused on thinner Ta<sub>2</sub>O<sub>5</sub>-ZrO<sub>2</sub> nanolaminates. As in the case of Ta<sub>2</sub>O<sub>5</sub>-HfO<sub>2</sub> nanolaminates, we used the same number of cycles for both Ta<sub>2</sub>O<sub>5</sub> and ZrO<sub>2</sub> constituent layers. Rapid thermal anneal was performed on these thinner films and the dielectric properties were tabulated in Table 5-9. For the as-deposited film of 9.86 nm (including the 2.76 nm silicon nitride layer), we obtained a dielectric constant of 13 and the SiO<sub>2</sub> equivalent thickness is 3 nm. Once the thickness dropped below 10 nm, the decrease of the dielectric constant slowed down. The dielectric constant of 8.46 nm nanolaminates still showed a k value of 11.5. This was partially due to the existence of Si<sub>3</sub>N<sub>4</sub> layer, which has a k value of 7.8. For the annealed samples, we observed the k values to vary with the annealing temperature and annealing ambient. When annealed at 700°C, k increased to 12. We believe this was due to the partial crystallization of the nanolaminates. At 800°C, k value dropped. This drop could be caused by the silicon oxidation at the Si/Si<sub>3</sub>N<sub>4</sub> interface. This SiO<sub>2</sub> layer contributes to the reduction in dielectric constant. At higher annealing temperature such as 900°C, the crystallization and Si oxidation have competitive role in determining the dielectric constant. Fig. 5.19 showed the leakage current property of Ta<sub>2</sub>O<sub>5</sub>-ZrO<sub>2</sub> thin film nanolaminates annealed at 600 – 900°C in O<sub>2</sub> for 60 s. The leakage current property of nanolaminates could be improved at the expenses of the dielectric constant decrease due to the interfacial layer growth. At the same time, crystallized structure in the thin film nanolaminates would introduce higher leakage current. The sample annealed at 1000°C in Ar showed the highest dielectric constant due to the crystallization but relatively high leakage current due to the oxide-free interface.

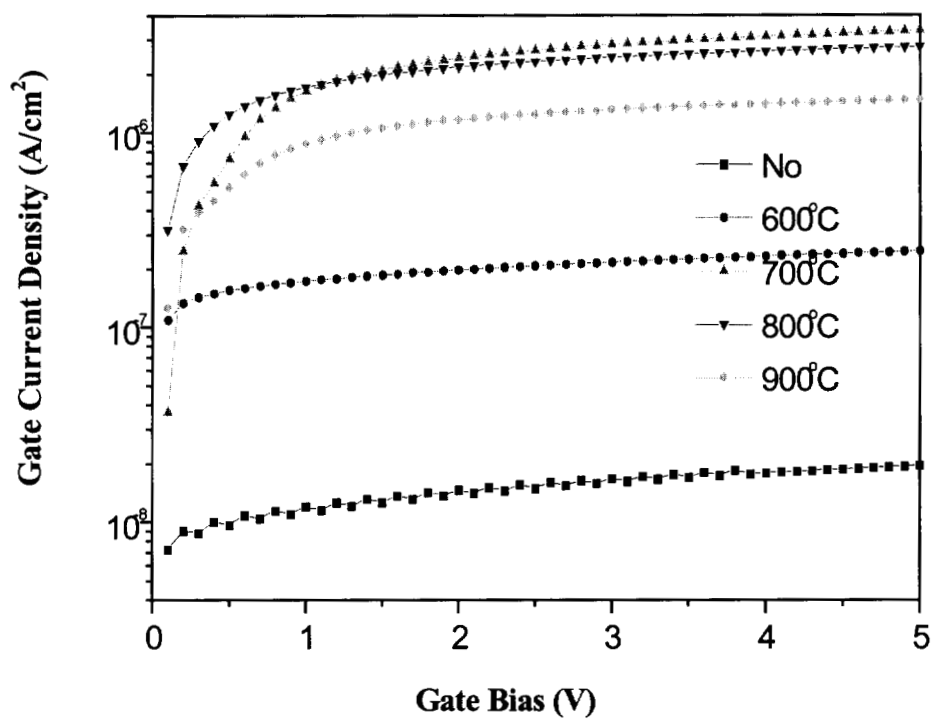


**Fig. 5.19** Gate current density of as-deposited and RTA treated Ta<sub>2</sub>O<sub>5</sub>- ZrO<sub>2</sub> nanolaminates grown on nitrated Si substrates. The thickness of the nanolaminates is about 3.7 nm and the nitride thickness is 2.76 nm.

**Table 5-9 Ta<sub>2</sub>O<sub>5</sub>- ZrO<sub>2</sub> nanolaminates grown on nitrided Si substrates. The thickness of Si<sub>3</sub>N<sub>4</sub> is 2.76 nm.**

Film stack	RTA	Total Thickness (nm)	Dielectric constant	SiO <sub>2</sub> equivalent thickness (nm)	Leakage current density (A/cm <sup>2</sup> ) at +1V.
10 Ta <sub>2</sub> O <sub>5</sub> + 2(20 Ta <sub>2</sub> O <sub>5</sub> +20 ZrO <sub>2</sub> )	No	9.86	13	3	3.5×10 <sup>-8</sup>
5 Ta <sub>2</sub> O <sub>5</sub> + 2(8 Ta <sub>2</sub> O <sub>5</sub> +8 ZrO <sub>2</sub> )	No	5.96	8	2.9	1.2×10 <sup>-8</sup>
5 Ta <sub>2</sub> O <sub>5</sub> + 2(8Ta <sub>2</sub> O <sub>5</sub> +8 ZrO <sub>2</sub> )	600°C in O <sub>2</sub> for 60 s	5.96	9	2.6	1.7×10 <sup>-7</sup>
5 Ta <sub>2</sub> O <sub>5</sub> + 2(8 Ta <sub>2</sub> O <sub>5</sub> +8 ZrO <sub>2</sub> )	700°C in O <sub>2</sub> for 60 s	6.36	12	2.1	1.6×10 <sup>-6</sup>
5 Ta <sub>2</sub> O <sub>5</sub> + 2(8 Ta <sub>2</sub> O <sub>5</sub> +8 ZrO <sub>2</sub> )	800°C in O <sub>2</sub> for 60 s	6.36	9	2.8	1.7×10 <sup>-6</sup>
5 Ta <sub>2</sub> O <sub>5</sub> + 2(8 Ta <sub>2</sub> O <sub>5</sub> +8 ZrO <sub>2</sub> )	900°C in O <sub>2</sub> for 60 s	6.46	11	2.3	8.8×10 <sup>-7</sup>
5 Ta <sub>2</sub> O <sub>5</sub> + 2(8 Ta <sub>2</sub> O <sub>5</sub> +8 ZrO <sub>2</sub> )	1000°C in Ar for 10 s	6.46	15	1.7	1.4×10 <sup>-6</sup>

### 5.3.3 ZrO<sub>2</sub>-HfO<sub>2</sub> nanolaminates

Besides the Ta<sub>2</sub>O<sub>5</sub> based thin film nanolaminates, work has been done to combine ZrO<sub>2</sub> and HfO<sub>2</sub> thin films. We expected even lower leakage current compared to previous two thin film nanolaminates because the individual binary oxides are both less leaky than pure Ta<sub>2</sub>O<sub>5</sub>. Although the dielectric constant of bulk ZrO<sub>2</sub> is slightly lower than that of bulk Ta<sub>2</sub>O<sub>5</sub>, with the decrease of the film thickness, the dielectric constant was expected to drop dramatically from its bulk value. For thin film of thickness about 10 nm, the dielectric constants of both ZrO<sub>2</sub> and HfO<sub>2</sub> binary oxides are close to 10. In this study, all thin film nanolaminates were grown directly on nitrided Si substrates. X-ray diffraction pattern indicated that the ZrO<sub>2</sub> - HfO<sub>2</sub> nanolaminates crystallized at 800°C.

Again crystallization contributed to the increase of dielectric constant and the leakage current. The electrical properties of as-deposited and RTA annealed ZrO<sub>2</sub> - HfO<sub>2</sub> nanolaminates are summarized in Table 5-10. It is noticed that the leakage current variation trend with film thickness of ZrO<sub>2</sub> - HfO<sub>2</sub> nanolaminates was very similar to that of the Ta<sub>2</sub>O<sub>5</sub> - ZrO<sub>2</sub> nanolaminates, except the leakage current of ZrO<sub>2</sub> - HfO<sub>2</sub> nanolaminates was lower than that of Ta<sub>2</sub>O<sub>5</sub> - ZrO<sub>2</sub> nanolaminates. Again the Si oxidation at the Si/Si<sub>3</sub>N<sub>4</sub> interface during annealing in oxygen would reduce the leakage current by forming a thin layer of SiO<sub>2</sub>. Rapid thermal annealing at temperature above 800°C caused the amorphous thin film to crystallize and thus increased the dielectric constant. The I-V characteristic of these nanolaminates was shown in Fig. 5.20.



**Table 5-10 ZrO<sub>2</sub>-HfO<sub>2</sub> nanolaminates growth on nitrated Si substrates. The thickness of Si<sub>3</sub>N<sub>4</sub> is 2.76 nm.**

Film stack	RTA	Total Thickness (nm)	Dielectric constant	SiO <sub>2</sub> equivalent thickness (nm)	Leakage current density (A/cm <sup>2</sup> ) at +1V
10 ZrO <sub>2</sub> + 2(20 ZrO <sub>2</sub> +20 HfO <sub>2</sub> )	No	11.6	14	3.2	$2.3 \times 10^{-8}$
5 ZrO <sub>2</sub> + 2(10 ZrO <sub>2</sub> +10 HfO <sub>2</sub> )	No	8.0	12	2.5	$3.6 \times 10^{-8}$
5 ZrO <sub>2</sub> + 2(5 ZrO <sub>2</sub> +5 HfO <sub>2</sub> )	No	7.6	11	2.3	$7.3 \times 10^{-8}$
5 ZrO <sub>2</sub> + 2(5 ZrO <sub>2</sub> +5 HfO <sub>2</sub> )	700°C in O <sub>2</sub> for 60 s	5.96	9	2.6	$3.7 \times 10^{-7}$
5 ZrO <sub>2</sub> + 2(5 ZrO <sub>2</sub> +5 HfO <sub>2</sub> )	800°C in O <sub>2</sub> for 60 s	5.96	12	1.8	$2.8 \times 10^{-7}$
5 ZrO <sub>2</sub> + 2(5 ZrO <sub>2</sub> +5 HfO <sub>2</sub> )	900°C in O <sub>2</sub> for 60 s	6.16	10	2.2	$2.9 \times 10^{-7}$
5 ZrO <sub>2</sub> + 2(5 ZrO <sub>2</sub> +5 HfO <sub>2</sub> )	1000°C in Ar for 10 s	6.16	9	1.7	$2.4 \times 10^{-7}$

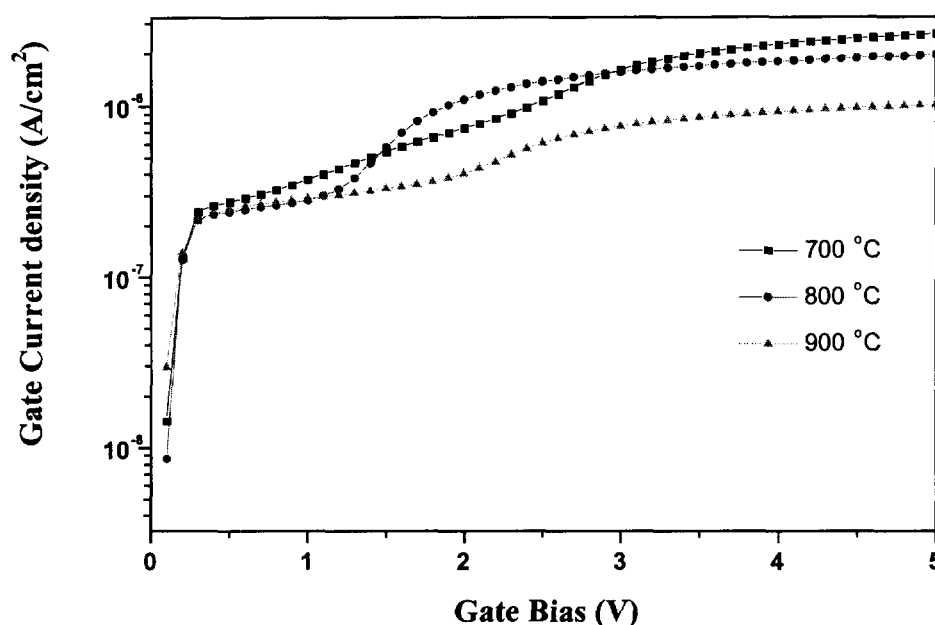


**Fig. 5.20** Gate current density of as-deposited and O<sub>2</sub> RTA treated ZrO<sub>2</sub>- HfO<sub>2</sub> nanolaminates grown on nitrided Si substrates. The thickness of the nanolaminates is about 3.4 nm and the nitride thickness is 2.76 nm.

#### 5.4. Electrical properties of SiON and High k films

It is well known that as the thickness approaches 2~3 nm, SiO<sub>2</sub> would suffer from very large leakage current. Silicon oxynitride (SiON) films are more resistant to current leakage compared to SiO<sub>2</sub>. We obtained a SiON thin film of 3.2 nm deposited on Si and measured the current-voltage characteristic. Fig. 5.21 indicated that the leakage current of SiON thin film was three orders higher than that of the high k nanolaminates with lower equivalent SiO<sub>2</sub> thickness when the gate bias is larger than +1 V. Among the three kinds of nanolaminates we investigated, ZrO<sub>2</sub> - HfO<sub>2</sub> nanolaminates showed the lowest leakage current, which was not surprising because each constituent binary oxide is less leaky than Ta<sub>2</sub>O<sub>5</sub>. For the same thickness Ta<sub>2</sub>O<sub>5</sub> - HfO<sub>2</sub> and Ta<sub>2</sub>O<sub>5</sub> - ZrO<sub>2</sub> nanolaminates,

the former was more leakage resistant. This was consistent with  $\text{HfO}_2$  being less leaky than  $\text{ZrO}_2$ .

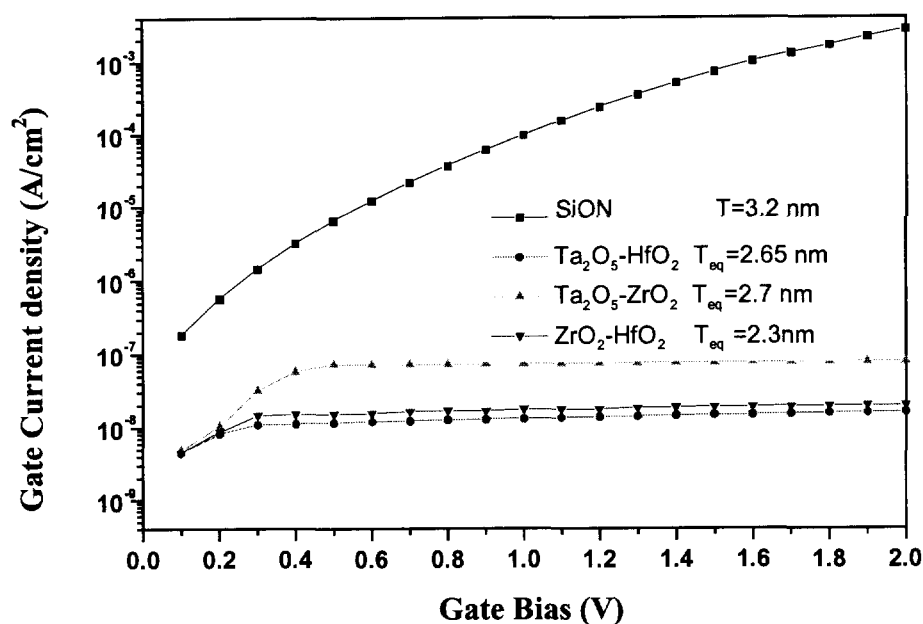


**Fig. 5.21** Gate leakage current of SiON,  $\text{Ta}_2\text{O}_5$  -  $\text{HfO}_2$  nanolaminates/ $\text{Si}_3\text{N}_4$ ,  $\text{Ta}_2\text{O}_5$  -  $\text{ZrO}_2$  nanolaminates/ $\text{Si}_3\text{N}_4$ , and  $\text{ZrO}_2$  -  $\text{HfO}_2$  nanolaminates/ $\text{Si}_3\text{N}_4$ . The thickness of  $\text{Si}_3\text{N}_4$  is 2.76 nm for all three nanolaminates.

Fig. 5.22 shows the breakdown characteristics of as-deposited thin films of  $\text{Ta}_2\text{O}_5$ ,  $\text{HfO}_2$  and  $\text{ZrO}_2$  on Si substrate pre-coated with 2.1 nm  $\text{Si}_3\text{N}_4$  at room temperature. The thickness of all three films is about 8 nm. Negative biases were used in order to keep the capacitors in accumulation region and therefore minimize the voltage drop in the substrate. The current is seen to increase slowly with bias until an abrupt irreversible breakdown occurs at applied field of about 11.5 MV/cm. This may be due to the existence of the  $\text{Si}_3\text{N}_4$  layer that has been reported to have high dielectric strength.

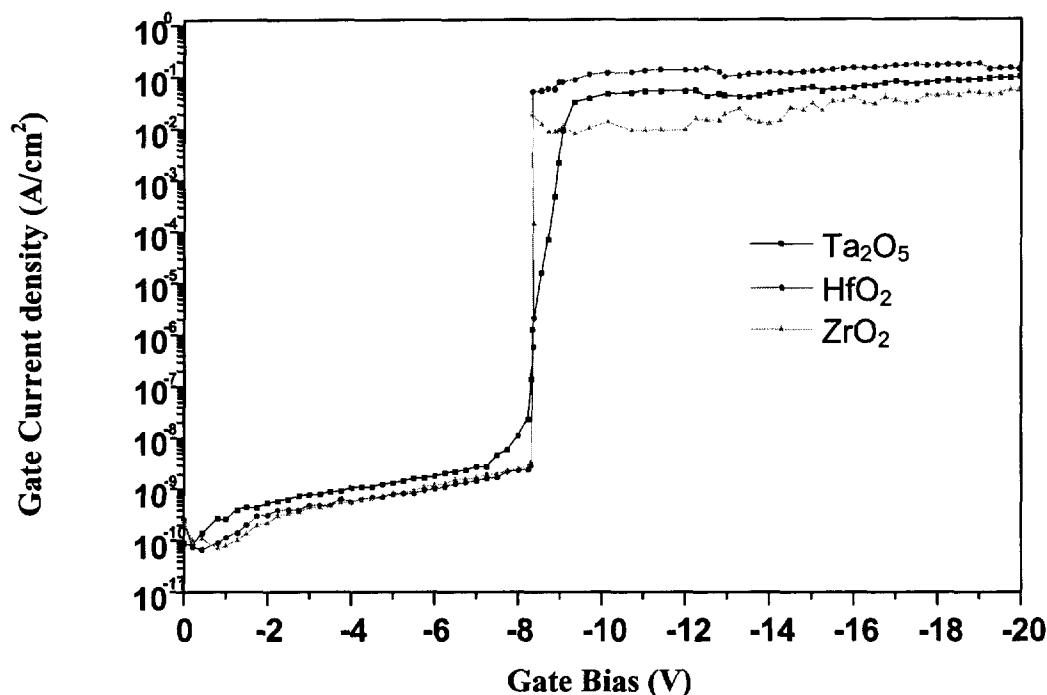


**Fig. 5.22 Ramped I-V characteristic of MIS capacitors with binary high k films driven to breakdown in the accumulation mode. All films are of 8 nm thick.**

A similar study on the I-V properties was performed on nanolaminates of Ta<sub>2</sub>O<sub>5</sub> - HfO<sub>2</sub>, Ta<sub>2</sub>O<sub>5</sub> - ZrO<sub>2</sub> and ZrO<sub>2</sub> - HfO<sub>2</sub> on 2.1 nm Si<sub>3</sub>N<sub>4</sub>. It is surprising to see that the ZrO<sub>2</sub> - HfO<sub>2</sub> has extremely high dielectric strength compared to the other two nanolaminates and constituent binary oxides, as illustrated in Fig. 5.23. Before irreversible breakdown occurs, the leakage current for all three nanolaminates was less than  $5 \times 10^{-7}$  A/cm<sup>2</sup>. The dielectric strengths of Ta<sub>2</sub>O<sub>5</sub> - HfO<sub>2</sub> nanolaminates and Ta<sub>2</sub>O<sub>5</sub> - ZrO<sub>2</sub> were 9.6 MV/cm and 9 MV/cm, respectively. However, the breakdown field for the ZrO<sub>2</sub> - HfO<sub>2</sub> was as high as 25 MV/cm.

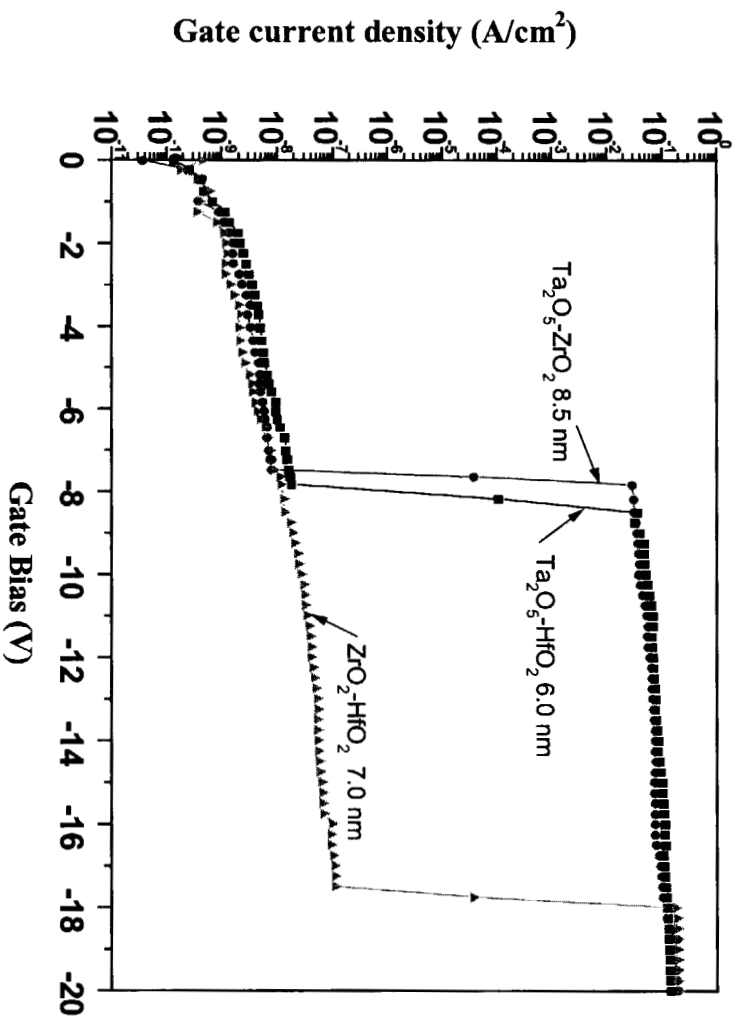


Fig. 5.23 I-V characteristics of MIS capacitors of  $\text{Ta}_2\text{O}_5$  -  $\text{HfO}_2$ ,  $\text{Ta}_2\text{O}_5$  -  $\text{ZrO}_2$  and  $\text{ZrO}_2$  -  $\text{HfO}_2$  nanolaminates in the accumulation region.

In this chapter, material and electrical properties of binary oxides  $\text{Ta}_2\text{O}_5$ ,  $\text{HfO}_2$ ,  $\text{ZrO}_2$  and their nanolaminates were investigated. Surface roughness of silicon nitride coated substrate and as-grown films with different thickness was studied using AFM. TEM indicated that a thin layer of  $\text{SiO}_2$  formed when high  $k$  films were deposited directly on Si substrate, and C-V measurement showed that this layer would reduce the effective dielectric constant of the high  $k$  film/ $\text{SiO}_2$  stack. Al and  $\text{Si}_3\text{N}_4$  were deposited as barrier layer of the Si oxidation separately. It was shown that the nitride was a better passivation film as to prevent Si surface oxidation by water vapor. C-V method had been used to calculate the dielectric constant, extract flatband voltage and characterize the interface charges. The leakage mechanisms of  $\text{Ta}_2\text{O}_5$ - $\text{HfO}_2$  nanolaminates were examined based on I-V measurement. Dielectric breakdown of these high  $k$  films and their nanolaminates were studied as well. As we shrink the thickness of these high  $k$  materials, the extracted dielectric constant would reduce which set a limitation on application of these materials. However, they are still promising candidates for replacing  $\text{SiO}_2$  as the future gate dielectric materials.

## References

- [1] D. K. Schroder, *Semiconductor Material and Device Characterization*, John Wiley & Sons, 1990, p. 46.
- [2] C. Goodman and M. Pessa, "Atomic Layer epitaxy," *J. Appl. Phys.* **60**, 1986, R65-R81.
- [3] M. Oikkonen, M. Blomberg, T. Tuomi, and M. Tammenmaa, "X-ray diffraction study of microstructure in ZnS thin films grown from zinc acetate by atomic layer epitaxy," *Thin Solid Films* **124**, 1985, pp. 317-321.
- [4] H. Kimura, J. Mizuki, S. Kamiyama, and H. Suzuki, "Extended absorption fine line structure analysis of the difference in local structure of tantalum oxide capacitor films produced by various annealing method," *Appl. Phys. Lett.* **66**, 1995, pp. 2209-2211.
- [5] L. K. Han, G. W. Yoon, D. L. Kwong, V. K. Mathews, and P.C. Fazan, "Effects of post-deposition annealing on the electrical properties and reliability of ultrathin chemical vapor deposited Ta<sub>2</sub>O<sub>5</sub> films," *IEEE Electron Device Letters*, **15**, 1994, pp. 280-282.
- [6] G. B. Alers, R.M. Fleming, Y.H. Wong, B. Dennis, A. Pinczuk, G. Redinbo, R. Urdahl, E. Ong, and Z. Hasan, "Nitrogen plasma annealing for low temperature Ta<sub>2</sub>O<sub>5</sub> films," *Appl. Phys. Lett.* **72**, 1998, pp. 1308-1310.
- [7] T. Hori, *Gate Dielectrics and MOS ULSIs*, Springer, 1997, p. 42.
- [8] K. Natori, D. Otami, and N. Sano, "Thickness dependence of the effective dielectric constant in a thin film capacitor," *Appl. Phys. Lett.* **73**, 1998, pp. 632-634.
- [9] M. Balog, M. Schieber, M. Michman, and S. Patai, "The chemical vapor deposition and characterization of ZrO<sub>2</sub> films from organometallic compounds," *Thin Solid Films* **41**, 1977, pp. 247-250.
- [10] B. Kralik, E. K. Chang, and S. G. Louie, "Structural properties and quasiparticle band structure of ziconia," *Physical Review B* **57**, 1998, pp. 7027-7032.
- [11] R. J. Hillard, J. M. Heddleson, D. A. Zier, P. Rai-Choudhury, and D. K. Schroder "Direct and rapid method for determining flatband voltage from non-equilibrium capacitance voltage data" in *Diagnostic Techniques for Semiconductor Materials and Devices* (J. L. Benton, G. N. Maracas, and P. Rai-Choudhury, eds). Electrochem. Soc., Pennington, NJ, 1992, pp. 261-274.

- [12] S. C. Sun and T. F. Chen, "A novel approach for leakage current reduction of LPCVD Ta<sub>2</sub>O<sub>5</sub> and TiO<sub>2</sub> films by rapid thermal N<sub>2</sub>O annealing," IEEE IEDM, San Francisco, CA, Dec. 11-14, 1994, pp. 333-336.
- [13] S. Kamiyama, H. Suzuki, H. Watanabe, A. Sakai, M. Oshida, T. Tatsumi, T. Tanigawa, N. Kasai, and A. Ishitani, "A comparative study of hot-carrier induced light emission and degradation in bulk and SOI MOSFETs," IEEE IEDM, Washington, DC, Dec. 10-13, 1995, pp. 49-52.
- [14] S. Kamiyama, H. Suzuki, H. Watanabe, A. Sakai, H. Kimura, and J. Mizuki, "Ultrathin tantalum oxide capacitor process using oxygen-plasma annealing," J. Electrochem. Soc. **141**, 1994, pp. 1246-1251.
- [15] H. Shinriki and M. Nakata, "UV-O<sub>3</sub> and Dry-O<sub>2</sub>: Two-step annealed chemical-vapor-deposited Ta<sub>2</sub>O<sub>5</sub> films for storage dielectrics of 64-Mb DRAM's," IEEE Trans. Electron Devices **38**, 1991, pp. 445-464.
- [16] H. Shinriki, M. Nakata, Y. Nishioka, and K. Mukai, "Two-step annealing technique for leakage current reduction in chemical-vapor-deposited Ta<sub>2</sub>O<sub>5</sub> film," IEEE Electron Devices Letters **10**, 1989, pp. 514-516.
- [17] H. Matsushashi and S. Nishikawa, "Optimum electrode materials for Ta<sub>2</sub>O<sub>5</sub> capacitors for high- and low- temperature processes," Jpn. J. Appl. Phys. **133**, 1994, pp. 1293-1297.
- [18] C. Isobe and M. Saitoh, "Effect of ozone annealing on the dielectric properties of tantalum oxide thin films grown by chemical vapor deposition," Appl. Phys. Lett. **56**, 1990, pp. 907-909.
- [19] F. Chiu, J. Wang, J. Lee, and S. Wu, "Leakage currents in amorphous Ta<sub>2</sub>O<sub>5</sub> thin films," J. Appl. Phys. **81**, 1997, pp. 6911-6915.
- [20] K. Kukli, J. Ihanus, M. Ritala, and M. Leskela, "Properties of Ta<sub>2</sub>O<sub>5</sub>-based dielectric nanolaminates deposited by atomic layer epitaxy," J. Electrochem. Soc. **144**, 1997, pp. 300-306.



## Chapter 6

### Summary and Conclusions

Thin films of binary oxides  $\text{Ta}_2\text{O}_5$ ,  $\text{HfO}_2$  and  $\text{ZrO}_2$  and their nanolaminates  $\text{Ta}_2\text{O}_5\text{-HfO}_2$ ,  $\text{Ta}_2\text{O}_5\text{-ZrO}_2$  and  $\text{ZrO}_2\text{-HfO}_2$  were grown on Si substrates by atomic layer epitaxy. The F-120 ALE reactor used in this study is a research level reactor that can handle 2"  $\times$  2" substrates. Process parameters, such as source material temperatures, substrate temperature, reactant gas flow rate, reactants pulse time and purging duration have to be optimized to get uniform deposition.

During the growth of  $\text{Ta}_2\text{O}_5$ , it was found that the best film uniformity was achieved at 300 °C and the film was identified as amorphous by X-ray diffraction pattern. Rapid thermal anneal (RTA) above 800°C introduced crystallization. However, film thickness did not change before and after RTA, which indicated the as-deposited film was already fairly dense when the growth temperature is higher than 200 °C. Spectroscopic ellipsometry confirmed the densities of as deposited and annealed films were the same. Secondary ion mass spectroscopy characterization indicated the  $\text{Ta}_2\text{O}_5$  film to be stoichiometric, with the concentration of chloride below the detection limit. Atomic force microscopy revealed that thicker film had a rougher surface. For  $\text{Ta}_2\text{O}_5$  film deposited directly on bare Si (with the native oxide being removed), a thin layer of  $\text{SiO}_2$  was

identified by Transmission Electron Microscope (TEM). This layer was formed during the  $\text{Ta}_2\text{O}_5$  film growth as the water vapor was used as oxygen source.

For  $\text{HfO}_2$  film, a more complicated surface reaction was observed. The uniformity of  $\text{HfO}_2$  was very poor and island growth existed in most cases. This film showed better adhesion to  $\text{Si}_3\text{N}_4$  coated substrate.  $\text{Si}_3\text{N}_4$  was also served as a barrier layer against Si oxidation. The as-deposited film was either amorphous or partially crystallized with very weak peak intensity. A preferred orientation in the (1,1,1) plane with very high intensity was detected by XRD after annealing at  $800^\circ\text{C}$ .

$\text{ZrO}_2$  growth requires longer pulse and purge time to realize the self-controlled process compared to the previous two oxides. It is found that  $\text{ZrCl}_4$  pulse was critical with respect to the thickness saturation, while short water pulse had no effect on the film thickness. Water purge time was essential to improve the film uniformity. ALE growth at  $300^\circ\text{C}$  produced nearly amorphous film and it crystallized upon  $700^\circ\text{C}$  RTA.

No process parameters needed to be optimized in the growth of nanolaminates due to the characteristics of ALE technique. We incorporated two binary oxides into a nanolaminate structure and the thickness was determined by the number of cycles of each constituent oxide layers. Since we focused on very thin nanolaminates (less than 10 nm), the dependence of dielectric properties on thickness ratio of two constituent oxides were not studied when we were already approaching the lower limit of allowable number of cycles.

For  $\text{Ta}_2\text{O}_5$ - $\text{HfO}_2$ , aluminum evaporated on Si as the water barrier layer was studied. A more complicated interface layer consisting of  $\text{Al}_2\text{O}_3/\text{SiO}_2$  after deposition of high k films was showed by TEM image, which indicated Al was not an effective coating for preventing Si surface oxidation. When  $\text{Si}_3\text{N}_4$  coated substrates were used, several techniques, such as SIMS, FT-IR spectrum and X-ray reflectivity analysis were used to determine that no  $\text{SiO}_2$  formed underneath the nitride layer after the high k films were deposited.

Dielectric properties of binary oxides and nanolaminates were characterized by various techniques, including C-V measurement, I-V measurement and ellipsometry. The relative dielectric constant ( $k$ ) was calculated from C-V curve. The C-V measurements on the films from same process but with different thicknesses showed a decreased dielectric constant versus the  $k$  value of bulk material as the film thickness was reduced. A significant drop of  $k$  value was observed for films less than 10 nm thick. This reduction in  $k$  has been shown to depend on the number of atomic monolayers and the atomic polarizability of the film. In other words, there were fewer dipole moments between two surfaces, the polarizability of the ultra thin film can be dramatically affected by its interfaces as opposed to the diminishing bulk properties.

Rapid thermal annealing (RTA) was performed in different ambients, including argon (Ar) and oxygen ( $O_2$ ). It showed a positive effect on the dielectric constant due to the crystallization of the film. However, annealing in Ar increased the leakage current because the crystallization facilitated the leakage path through the grain boundaries. The reduction of gate current in  $O_2$  RTA could be due to the formation of thin  $SiO_2$  layer. This very thin  $SiO_2$  layer had little effect on  $k$  for high  $k$  film of 16 nm thick. However, a negative effect on  $k$  was expected for thinner film with this very thin  $SiO_2$  layer although no experiments were performed. We have to compensate between the increased  $k$  value and increased leakage current after RTA process.

Among the three binary oxides,  $HfO_2$  showed the lowest leakage current while  $Ta_2O_5$  was the most leaky film due to the small bandgap. Therefore  $ZrO_2$ - $HfO_2$  demonstrated the best leakage resistant characteristic among the three nanolaminates while all three nanolaminates showed lower leakage compared to  $SiO_2$  of same thickness. The leakage mechanism was studied on  $Ta_2O_5$ - $HfO_2$  nanolaminates. It revealed that Schottky emission was responsible for the leakage at low electric field and Poole-Frenkel conduction dominated at high field. The dielectric strength of  $Ta_2O_5$ ,  $HfO_2$  and  $ZrO_2$  was very close with the breakdown occurred at applied field of about 11.5 MV/cm. It was surprising that the dielectric strength of  $ZrO_2$ - $HfO_2$  was much higher than that of the

Ta<sub>2</sub>O<sub>5</sub>-HfO<sub>2</sub> and Ta<sub>2</sub>O<sub>5</sub>-ZrO<sub>2</sub>, showing 25MV/cm versus 9.6 MV/cm and 9 MV/cm respectively.

The charges at the Si interface were studied based on C-V measurements. The flatband voltage of Ta<sub>2</sub>O<sub>5</sub> - HfO<sub>2</sub> nanolaminates grown on Si<sub>3</sub>N<sub>4</sub> was determined to be -1.1V and the calculated fixed charge density was about  $8.3 \times 10^{10} \text{ cm}^{-2}$ . There were methods discussed in chapter 2 that can be used to measure interface charge density, it either requires a MOSFET device or some theoretical data that involves very complicated calculation. Therefore, no interface charge density results were reported.

Several issues remain to be solved in the future for this study. Using water as the oxygen source will cause the Si surface oxidation if no barrier layer was used. There are possible alternatives to resolve this problem such as using N<sub>2</sub>O or NO to replace current DI water. At least the oxidation rate should be much lower than using water and the thickness of silicon oxide layer (if it exists) can be dramatically reduced, therefore relieve the negative effect on dielectric constant.

It is always desired to fabricate MOSFET devices using the high k films investigated. Transistors using Ta<sub>2</sub>O<sub>5</sub> and ZrO<sub>2</sub> have been recently reported, however transistors made with the nanolaminates have not been studied yet. Special attention should go to the HfO<sub>2</sub> since it had been reported as etch-stop material. To make the studied films applicable in manufacturing, reactive ions etching with proper etch rate and selectivity to silicon would be critical. For MOSFET applications the dielectric films must be etched down to source and drain which have shallow junctions. It is essential to control the etch process in order to protect the junction area.

Gate-electrode material is closely related to the dielectric reliability and gate leakage. There are many other choices, such as polysilicon, TiN, Pt or other metal stacks, that may improve the dielectric properties. The deposition of gate material is very important in respect of the ultra thin dielectric film. The interface between gate and dielectric needs to be studied as well.

A theoretical study on the dependence of dielectric constant on film thickness is critical for high  $k$  materials. There are many contrary results in literature. It is puzzling that dielectric constant of bulk material has been reported for ultra thin film by some researchers. An in-depth investigation including experiments and simulations would be necessary to resolve the issue.

The charges inside the nanolaminates would be of interest since there are many interfaces within the dielectric material. The effect of these charges on the leakage and reliability should be examined.

Finally, with the shrinkage of feature size, deposition and characterization of high dielectric constant material will continue to be one of the most interesting research topics in the future.

### Vita

The author, Hui Zhang, was born in Ying Kou, Liao Ning, China, in January, 1972. She enrolled in Central South University of Technology in 1990 and received a B.E. in Material Science and Engineering in 1994. After working for Hunan Research Institute of Material and Metallurgy in Changsha, Hunan for one year, she enrolled in the Department of Material Science and Engineering at Oregon Graduate Institute of Science and Technology in 1995 and received her M.S. in Material Science in 1997. At the same year, she entered the Department of Electrical Engineering at Oregon Graduate Institute and obtained her M.S. and Ph.D. in Electrical Engineering in 1998 and 2000, respectively. She has authored several scientific publications during the years at OGI. She married Jianxiong Zhao in 1995.